High frequency VLBI observations of galactic and extragalactic sources

INAUGURAL-DISSERTATION

zur
Erlangung des Doktorgrades
der Mathematisch-Naturwissenschaftlichen Fakultät
der Universität zu Köln

vorgelegt von

Christoph Rauch

aus
Bergisch Gladbach, Deutschland

Köln 2016

Angefertigt mit Genehmigung der Mathematisch-Naturwissenschaftlichen Fakultät
der Universität zu Köln

1. Referent: Prof. Dr. Andreas Eckart
2. Referent: Prof. Dr. Anton Zensus
Tag der Promotion: 21.04.16
Erscheinungsjahr: 2016

Diese Dissertation ist auf dem Universitäts Publikations Server der Universität
Köln unter http://kups.ub.uni-koeln.de/ elektronisch publiziert.

Universität zu Köln

Abstract

by Christoph Rauch

for the degree of

Doctor rerum naturalium

The radio source Sagittarius A* (Sgr A*), which is commonly associated with the super-massive black hole in the Galactic Center, offers the largest angular dimension of an active galactic nucleus and, therefore, the best opportunity to study the underlying physics of these objects. While orbital parameters of nearby stellar sources have proven its existence beyond reasonable doubt, its energy production mechanism is still uncertain.

Sgr A* shows intensity outbursts, referred to as flares, which occur on time scales ranging from 7-10 minutes (sub-flares) to 1-2 hours (main-flares). Several models are currently under investigation, that can explain the observable properties of the quiescent and flaring state of Sgr A*. The observed amplitudes and time scales of near-Infrared (NIR) and X-ray flares are consistent with expected values of an expansion with an adiabatic cooling mechanism. Alternatively, a hot spot model, is also capable of reproducing the observed parameters. Such a feature is, in analogy to the solar coronal mass ejection, formed by flux ropes, which are capable of rapidly expelling material, if their equilibrium stability is lost. Other models explain these flux excesses by a temporary accretion disc with a short time jet or a mixed Jet-advection-dominated accretion flow.

A set of observable parameters, that can be used to discriminate between the currently proposed models, are the full-width at half max (FWHM) Gaussian size of the emission region, the absolute position of Sgr A*, its symmetry, as well as time delays and time scales of its flares. Relativistic magnetohydrodynamic simulations predict an almost constant size and shape of the emission region. Therefore, a change of its FWHM size, position or symmetry would point towards a jet or hot spot model. The expected changing source size and/or asymmetry are caused by an adiabatically expanding, orbiting or spatially constant, off-center component. In addition to this, the flares of Sgr A* show correlated flux excesses at different wavelengths ranging from NIR/X-ray to radio frequencies. The time delay found between these frequencies offers the opportunity to analyze physical properties that arise at different radii, because individual observing bands measure distinct radial regions.

The subject of this thesis is to discriminate between the described flaring models of Sgr A*. Three six-hour Very Long Baseline Interferometry (VLBI) observations at 43 GHz have been performed on May 16 - 18 2012 in parallel

to NIR observations carried out at the Very Large Telescope (VLT). A NIR flare observed on May 17 triggered the VLBI observation of this date, which shows a flare peaking at 1.41 Jy, delayed by (4.5 ± 0.5) h. This increasing flux density is apparently accompanied by a changing source structure, that can best be modeled by a central emission region with a weak secondary component of 0.02 Jy at about 1.5 mas under 140° (east of north).

Different cleaning methods have been tested, which lead to consistent maps of Sgr A* showing an off-center component in both polarizations. Symmetry-tests, based on analysis of closure phases, residual noise maps and simulated artificial data sets, improved the robustness of this two component model. Furthermore, positions acquired from phase referencing analysis offer large error limits and have to be considered as constant.

The observed position of the secondary component, which is still affected by interstellar scattering, offers speeds of (0.4 ± 0.3) c for the presented time delay of (4.5 ± 0.5) h between the NIR and 7 mm flare. This time lag represents the velocity between different radial regions around the black hole mapped by the individual frequencies. Relating this and several other delays, provided by the current literature, to theoretical intrinsic source sizes and interpolating them to a common NIR/X-ray center, results in a radial velocity profile of Sgr A* that appears to be accelerating towards the outermost regions.

The complexity of required calibration and technical observing inaccuracies does not allow to completely exclude weather or other random observational effects to be the cause of the extended source structure, but we have shown, that with most careful cleaning efforts, this two component structure stays robust and is most probable a real data feature. The complete quantity of indications of a secondary component during the flaring states of Sgr A* are within one to two sigma. The consistent set of hints towards a two component structure excludes the hot spot model, because of its spatial dimension, and points towards the existence of a temporary jet anchored at Sgr A*.

UNIVERSITÄT zu Köln

Zusammenfassung

von Christoph Rauch

zur Erlangung des Doktorgrades

Doctor rerum naturalium

Das im Allgemeinen mit der Radioquelle Sagittarius A* (Sgr A*) assoziierte super-massereiche Schwarze Loch im galaktischen Zentrum bietet die größte räumliche Dimension eines aktiven Galaxiekerns und daher die beste Möglichkeit die zugrunde liegenden physikalischen Prozesse dieser Objekte zu untersuchen. Während Orbitalparameter benachbarter Sterne dessen Existenz jenseits begründeter Zweifel bewiesen haben, ist der vorhandene Energieproduktionsmechanismus noch nicht vollständig geklärt.

Sgr A* zeigt Intensitätsausbrüche, die auch als Flares bezeichnet werden, auf Zeitskalen von 7-10 Minuten (Sub-Flares) bis zu 1-2 Stunden (Main-Flares). Verschiedene Modelle werden derzeit diskutiert, welche fähig sind, die beobachtbaren Eigenschaften der inaktiven und aktiven Phasen von Sgr A* zu erklären. Die Amplituden und Zeitskalen der Nahinfrarot- (NIR) und Röntgen-Flares sind konsistent mit einer adiabatisch gekühlten Expansion. Alternativ kann auch ein Hot-Spot Modell diese Parameter reproduzieren. Solch eine Struktur wird, in Analogie zum solaren koronalen Massenauswurf, durch Flussröhren geformt, welche fähig sind Material rapide auszuwerfen, sobald sie ihre Gleichgewichtsstabilität verlieren. Andere Modelle erklären die beobachteten Intensitätsausbrüche durch eine temporäre Akkretionsscheibe und einen kurzzeitigen Jet sowie durch ein Konglomerat aus Jet und advektions-dominierter Akkretion.

Die Halbwertsbreite (FWHM) der Emissionsregion, die absolute Position von Sgr A*, dessen Symmetrie sowie die Zeitunterschiede und Zeitskalen der Flares bieten eine Reihe beobachtbarer Parameter, die herangezogen werden können, um zwischen den derzeitigen Modellen zu unterscheiden. Relativistische Magnetohydrodynamik Simulationen sagen eine beinahe konstante Größe und Form der Emissionsregion voraus. Daher würde eine Veränderung der FWHM, Position oder Symmetrie auf ein Jet oder Hot-Spot Modell hindeuten. Die erwartete Veränderung der Quellgröße und/oder Asymmetrie werden durch eine adiabatisch expandierende, außerhalb des Zentrums gelegene, statische oder es umkreisende, Komponente hervorgerufen. Außerdem zeigen die Intensitätsausbrüche korrelierte Flussexzesse zwischen verschiedenen Wellenlängen, die sich über den NIR-/Röntgenstrahlungs- bis zum Radiobereich erstrecken. Die Zeitverzögerung zwischen verschiedenen Frequenzen bietet die Möglichkeit physikalische Eigenschaften auf unterschiedlichen Radien zu analysieren, da einzelne

Aufnahmebänder verschieden Tiefen detektieren.

Diese Dissertation beschäftigt sich mit dem Thema, zwischen den beschriebenen Modellen der aktiven Phasen von Sgr A* zu unterscheiden. Drei sechsstündige Langbasisinterferometrieaufnahmen (VLBI) bei 43 GHz wurden zwischen dem 16. und 18. Mai 2012, parallel zu NIR-Aufnahmen des Very Large Telescopes (VLT), durchgeführt. Ein NIR-Flare am 17. Mai triggerte die VLBI-Aufnahmen dieses Datums, die eine um (4.5 ± 0.5) h verzögerte ansteigende Flussdichte bis auf einen Wert von 1.41 Jy detektierten. Dieser Flare geht anscheinend mit einer Veränderung der Quellstruktur einher, welche am besten durch eine zentrale Emissionsregion und eine schwache sekundäre Komponente von 0.02 Jy, die sich unter einem Winkel von 140° (östlich) in einer Entfernung von 1.5 mas befindet, modelliert werden kann.

Verschiedene Bildgenerierungsmethoden wurden geprüft und weisen konsistente Karten von Sgr A* mit einer sekundären Quelle abseits des Zentrums in beiden Polarisationen auf. Die Belastbarkeit dieses Zweikomponentenmodells wurde getestet, indem die Quellsymmetrie anhand von Closure Phasen, Rauschresiduen und simulierten Datensätzen untersucht wurde. Des Weiteren zeigen die Positionen, die durch Phasenreferenzierungsanalysen erhalten wurden, hohe Fehlergrenzen und müssen daher als konstant angesehen werden.

Die beobachtete Position der sekundären Komponente, welche durch interstellare Streuung beeinträchtigt ist, zeigt Geschwindigkeiten von (0.4 ± 0.3) c für eine Zeitverzögerung von (4.5 ± 0.5) h zwischen NIR- und 7 mm-Flares. Diese Verzögerung repräsentiert die Geschwindigkeit zwischen den verschiedenen Radien um das Schwarze Loch, welche durch die unterschiedlichen Frequenzen detektiert werden. Bringt man diese und andere, in der derzeitigen Literatur erwähnten, Zeitverzögerungen in Relation zu der theoretischen intrinsischen Quellengröße und interpoliert sie in Bezug auf ein gemeinsames NIR-/Röntgenstrahlungs-Zentrum, so ergibt sich ein radiales Geschwindigkeitsprofil von Sgr A*, welches eine Beschleunigung hin zu den äußersten Regionen aufzeigt.

Die Komplexität der Kalibrations- und technischen Aufnahmeungenauigkeiten erlaubt es nicht, Wetter oder andere zufällige Aufnahmeeffekte auszuschließen. Es kann aber behauptet werden, dass selbst bei einer mit höchstmöglicher Achtsamkeit durchgeführten Bildgenerierung die Zweikomponentenstruktur belastbar bleibt und daher höchstwahrscheinlich ein reales Datenmerkmal ist. Die Gesamtheit der Hinweise auf eine sekundäre Komponente während der aktiven Phasen von Sgr A* liegt innerhalb von ein bis zwei Sigma. Diese konsistente Reihe von Anzeichen für eine Zweikomponentenstruktur schließt ein Hot-Spot-Modell, aufgrund seiner räumlichen Ausdehnung, aus und deutet auf die Existenz eines kurzzeitigen Jets mit Ursprung in Sgr A* hin.

A scientist is happy, not in resting on his attainments but in the steady acquisition of fresh knowledge.

Max Planck, 1858 - 1947

Acknowledgements

I thank Prof. Dr. A. Zensus to open the possibility for me to work in the VLBI group and granting the funding. I am grateful for his effective and positive supervision during the thesis advisory committee and several personal meetings, which were not only scientifically fruitful, but also provided organizational help.

I would like to express my gratitude to Prof. Dr. A. Eckart for supervising me during my Diploma thesis and Dissertation over the last years. Thank you for giving me the impression of always being welcome and solving my many questions with impressive facility.

I would like to thank Prof. Dr. E. Ros for introducing me into the astonishing world of radio astronomy and for always having an open door. Not only for his very constructive scientific advices, but also for his permanent good mood while answering my many questions, which created a pleasant and productive working atmosphere.

Furthermore, I thank Dr. T. P. Krichbaum for his time spent and scientific input which kept me on track towards generating real and reliable results. Even during periods of peaking work loads he found the time to help me with his knowledge in the data reduction and imaging processes as well as technical aspects, that were mandatory for this work.

And of course I want to thank Dr. K. Mužić for her participation in the thesis advisory committee meetings and her scientific input for the publication of this thesis.

I want to thank Banafsheh Shahzamanian for providing us with the NIR light curve on which the VLBI observations have been triggered, that lead to interesting results.

Dr. Ru-Sen Lu has earned my thanks for sharing his knowledge with us and providing additional ideas.

And of course my office mates Dr. Biagina Boccardi, Dr. Sebastian Kiehlmann and Dr. Vassilis Karamanavis, who managed to be a reliable source of information and joy, that was just one look over the shoulder away.

I also want to thank Dr. Jeff Hodgson for correcting our publication and further improving its scientific results.

The whole VLBI group also deserves to be thanked for their advices and interesting topics during our meetings.

Further acknowledgements go to the participants of conferences at the physics departments of the Christian-Albrechts-university in Kiel and the Nicolaus Copernicus

University in Toruń, who raised new ideas during my visits.

Special thanks go to my family for their support and love during this time.

This work was supported through a stipend from the International Max Planck Research School (IMPRS) for Astronomy and Astrophysics at the Universities of Bonn and Cologne.

Contents

List of Figures

List of Tables

Nomenclature

Abbreviations

ADAF	Advection-dominated accretion flow
ADIOS	Advection-dominated inflow-outflow solutions
AGN	Active galactic nuclei
AO	Adaptive optics
BR	Brewster
CARMA	Combined Array for Research in Millimeter Astronomy
CDAF	Convection-dominated accretion flows
CONICA	Coudée Near Infrared Camera
CXC	Chandra X-ray Observatory
DC	Direct current
Dec.	Declination
DFT	Direct Fourier transform
EDAF	Ejection-dominated accretion flow
ESA	European Space Agency
EVN	European VLBI Network
FD	Fort Davis
FFT	Fast Fourier transform
FWHM	Full-width-at-half-maximum
HN	Hancock
IC	Inverse Compton
ICRF	International Celestial Reference Frame
IF	Intermediate frequency
IRAC	Infrared Array Camera
ITRF	International Terrestrial Reference Frame
JCMT	James Clerk Maxwell Telescope
JPL-Caltech	Jet Propulsion Laboratory at California Institute of Technology
KP	Kitt Peak
LA	Los Alamos
LCP	Left-handed circular polarization (counter-clockwise)
LO	Local oscillator
MK	Mauna Kea
MOJAVE	Monitoring of Jets in Active Galactic Nuclei with VLBA Experiments
NACO	NAOS and CONICA
NAOS	Nasmyth Adaptive Optics
NASA	National Aeronautics and Space Administration
NIR	Near-Infrared
NL	North Liberty
NRAO	National Radio Astronomy Observatory

NSC	Nuclear stellar cluster
OV	Owens Valley
PSF	Point-spread-function
PT	Pie Town
Quasar	Quasi-stellar radio source
QSO	Quasi-stellar object
R.A.	Right ascension
RCP	Right-handed circular polarization (clockwise)
RFI	Radio frequency interference
RIAF	Radiatively inefficient accretion flow
SC	St. Croix
SED	Spectral energy distribution
SEFD	System equivalent flux density
Sgr A*	Sagittarius A*
SMBH	Super-massive black hole
SMT	Submillimeter Telescope
SNR	Signal to noise ratio
SSC	Synchrotron + synchrotron self-Compton
SSC-Caltech	Spitzer Space Center at California Institute of Technology
STScI	Space Telescope Science Institute
TANAMI	Tracking Active Galactic Nuclei with Austral Milliarcsecond Interferometry
TEC	Total electron content
VIPS	VLBA Imaging and Polarimetry Survey
VLBA	Very Long Baseline Array
VLBI	Very Long Baseline Interferometry
VLT	Very Large Telescope

Used Symbols

a	Angular momentum per unit mass
A_{ij}	Visibility Amplitude
$\vec{A_{ij}}$	Additive baseline errors
A_{V}	Extinction magnitude
b	Digitization loss or normalization coefficient
$\vec{B}$	Baseline
$B_{\perp\!\!\!\mid\mid}$	Parallel magnetic field strength
$\bar{B_{ij}}$	Bandpass response matrix
β	power spectrum exponent
β_{app}	Apparent speed
c	Speed of light or constant
C_n^2	Refractive index structure constant
Γ	Lorentz factor
D	diameter
$\bar{D_{ij}}$	Polarization leakage matrix
δ	Declination
δi	phase error of the equipment at i.
δ_{var}	Variability Doppler factor
$\bar{J_{ij}}$	Antenna voltage pattern matrix
E_ν	Sum of all monochromatic waves emitted by sources at a frequency ν
E_ν^*	Complex conjugate of $E_\nu(\vec{r})$
$F[f(x)]$	Fourier transform of a function $f(x)$
$\bar{F_{ij}}$	Ionospheric effect matrix
G	Gravitational constant
g_i	Voltage gain
G_i	Conversion gain factor
$\bar{G_{ij}}$	Electronic gain matrix
γ	power law exponent or loop gain value
η	fringe moduli function
η_s	Electronic losses
I_ν	Intensity a frequency ν
J	Angular momentum
J_i	Corrupting factor
$\bar{J_{ij}}$	Observational effects operator
k	Wave number
K	Normalization function
K_i	Antenna sensitivity
θ	Angle
θ_0	Isoplanatic angle
θ_{int}	Intrinsic angular size
θ_{obs}	Observed angular size

θ_{sca}	Scattering angle
l	Direction cosines pointing at source
λ	Wavelength
m	Mass or direction cosines pointing at source or polarization level
M	Unit mass
$\bar{M_{ij}}$	Multiplicative baseline errors
N	Number of positions or stations
n_e	Number of electrons
n_i	Noise term
ν	Frequency
$\Delta\nu$	Observing bandwidth
ξ_{ij}	phase of the Fourier transform at baseline ij
p	Pressure
$\bar{P_{ij}}$	Parallactic angle matrix
R	Radius
Q, U	Stokes Parameter of liner polarization
$\vec{r_i}$	Observer location
R_s	Schwarzschild radius
S	Flux density
$\vec{s}$	Unit vector towards source
s_i	Signal of a source
t	Time
T	Temperature
$\bar{T_{ij}}$	Tropospheric effects matrix
T_{b}	Brightness temperature
T_{s}	System temperature
τ	Geometric time delay
τ_{acc}	Accumulation time
u, v	Coordinates of the plane orthogonal towards the line of sight ((u, v)-plane)
v	Speed
V	Stokes parameter of circular polarization
V_ν	Visibility function at frequency ν
Φ	Phase
$\Delta\phi$	Misalignment angle of phase shift
x_i	Signal of antenna i
χ	Polarization angle
Ψ	Opening angle or phase angel
$d\Omega$	Surface element of the celestial sphere
ω_i	time variable phase rotation of scans at telescope i.
z	Distance

Numerical Constants

π	$= 3.14159$
$1\,\mathrm{rad}$	$= 57.296\,\mathrm{degrees}$

Physical Constants

Speed of light	$c = 2.9979 \times 10^{8}\,\mathrm{m\,s^{-1}}$
Gravitational constant	$G = 6.670 \times 10^{-11}\,\mathrm{N\,m^{2}\,Kg^{-2}}$

Astronomical Constants

Astronomical unit ($1\,\mathrm{AU}$)	$= 1.496 \times 10^{11}\,\mathrm{m}$
Parcec ($1\,\mathrm{pc}$)	$= 3.086 \times 10^{16}\,\mathrm{m}$
Julian light year ($1\,\mathrm{ly}$)	$= 9.460730472 \times 10^{15}\,\mathrm{m}$
Julian year ($1\,\mathrm{yr}$)	$= 3.15576 \times 10^{7}\,\mathrm{s}$
Solar mass ($1\,\mathrm{M}_{\odot}$)	$= 1.989 \times 10^{30}\,\mathrm{Kg}$

Chapter 1

The Galactic Center

The universe has formed between (13.796 ± 0.029) and (13.813 ± 0.038) Gyr ago, based on current cosmic microwave background measurements (Planck Collaboration XIII, 2015). After the fundamental particles formed during the very first seconds, these condensed into protons, neutrons and electrons, the first simple components of atoms. At this early stage 10 s to 20 min after creation, the thermal energy was still very high and thus, the high velocity of electrons prevented them from being caught in the sphere of influence of other particles, that already had synthesized the least complex nuclei of Hydrogen (1p, 0n), Helium (2p,2n) and Lithium (3p, 3-4n) through fusion processes. After the incident thermal energy has been mitigated (around 3×10^6 years), the electrons could be captured by the nuclei and form the first electrically neutral atoms.

A large volume of interacting particles shows the tendency to condense into filamentary structures consisting of small scale clumps at the positions of density irregularities. These gravity seeds will then start to gather more material by collision and gravitational attraction, forming, due to an initial rotation, spinning compact objects, that extract excessive matter in form of jets along the axis of least resistance (rotation axis). After the system has reached equilibrium state this process usually forms rotating spheroids with a central massive core like planets, stars or elliptical galaxies (E0-6 type). This process can to some extend be found on many astronomical scales, ranging from the large scale Galaxy clusters, over Galaxies, down to solar systems. This evolution shows that all Galaxies contain a very massive core and while stellar black holes can be formed, depending on their initial size, for masses above $1.5-3\,M_\odot$ Bombaci (1996), it is logical to assume that most, if not all galactic nuclei contain a black hole, like Sgr A*, which is the main topic of this thesis (e.g., Richstone et al. 1998; Gebhardt et al. 2000; Ferrarese & Merritt 2000; Gültekin et al. 2009; Seth et al. 2014). Figure 1.1 shows a logarithmic illustration of the current picture of the universe up to the Big Bang. The current observable universe, defined by the maximum traveling range of light since the cosmological expansion, spreads over 28.5 Gpc.

The high density during the early stages of the universe, emphasizes creation of very massive objects. Therefore, after first clumping of matter into large filaments, the earliest created objects are assumed to be massive galaxies, quasars and population III stars. The strong radiation originating from these objects was capable of ionizing the surrounding material around 350×10^6 years ago. Within these high mass objects, many stars starting to fuse matter into more complex elements. Iron atoms are the end of this fusion chain, because it offers the highest bounding energy per nucleon (see Fig.1.2, left part) and thus, is found in the core of stellar or planetary objects

Figure 1.1: Observable universe in logarithmic scale. The image is centered on the sun with the Big Bang at its edge. Source: Pablo Carlos Budassi/Wikimedia Commons.

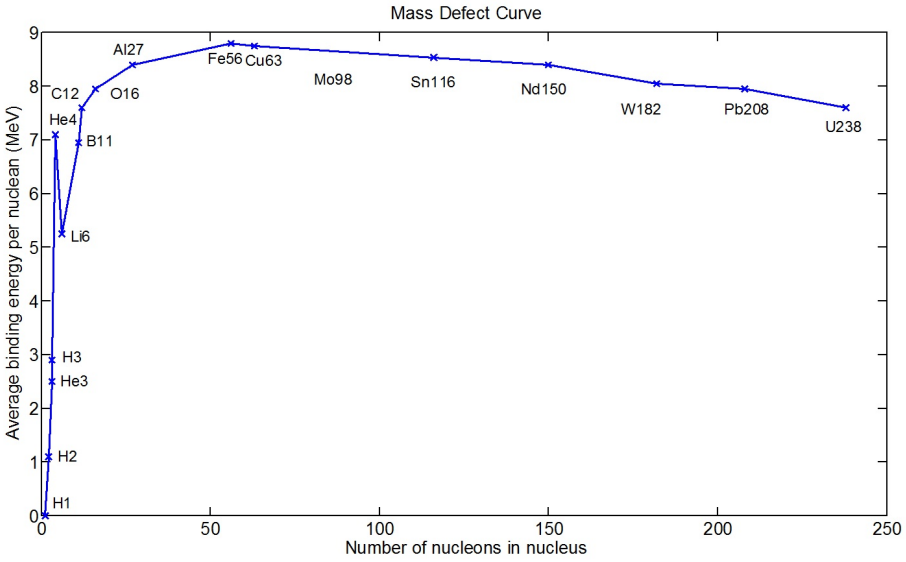

Figure 1.2: Binding energy per nucleon as a function of their total number contained in the nucleus. Source: Lewis (2008)

and their primordial stages. The evolution of some of these stars into a super nova created additional elements such as Uranium, which is capable of creating the remaining presently existing elements by nuclear fission processes (right part of Fig. 1.2).

Our host galaxy, the Milky Way, is located in the, so called, Local Group of galaxies and offers a decentralized picture of our extended definition of home. At larger scales, this group is part of the Laniakea cluster (see Fig. 1.3), which is centered around a gravitational anomaly, called the Great Attractor (R.A.: 10h32m, Dec.: $-46°00'$) at a distance of (45-50) Mpc (Mieske et al., 2005). While our solar system is located about 10-20 pc above the Galactic plane in the Orion-Cygnus arm, a relatively low density region of a normal barred spiral galaxy (see Fig. 1.4), the distance of ∼8 kpc towards its center yields a ∼26000 ly long path of possible electromagnetic aberration for the optical radiation originating in this region (see also Chap. 3). Observations of the Galactic Center are limited by obscuring dust and gas that affects electromagnetic radiation passing through it. It's a challenging task to overcome this hurdle at optical/NIR frequencies and it was not possible to gain high angular resolution images of this region until observational methods advanced to a state, that made it possible to detect fine structures and objects (see Fig. 1.5).

This extinction has its strongest effect close to the Galactic Center. Radio, infrared and X-ray wavelengths can pass this veil less affected and are, therefore, the best wavelengths to study the Galactic Center. This is also true for all sources located behind the Galactic Center, which casts an observational shadow (see Fig. 1.4). The Galactic disk rotates clockwise as viewed from the galactic north at about 220 to 244 $\mathrm{km\,s^{-1}}$ (Bovy et al., 2009; Gillessen et al., 2009), with a rotation curve ratio of 29 to 32 $\mathrm{km\,s^{-1}\,kpc^{-1}}$ (Reid & Brunthaler, 2004; Reid et al., 2009; McMillan et al.,

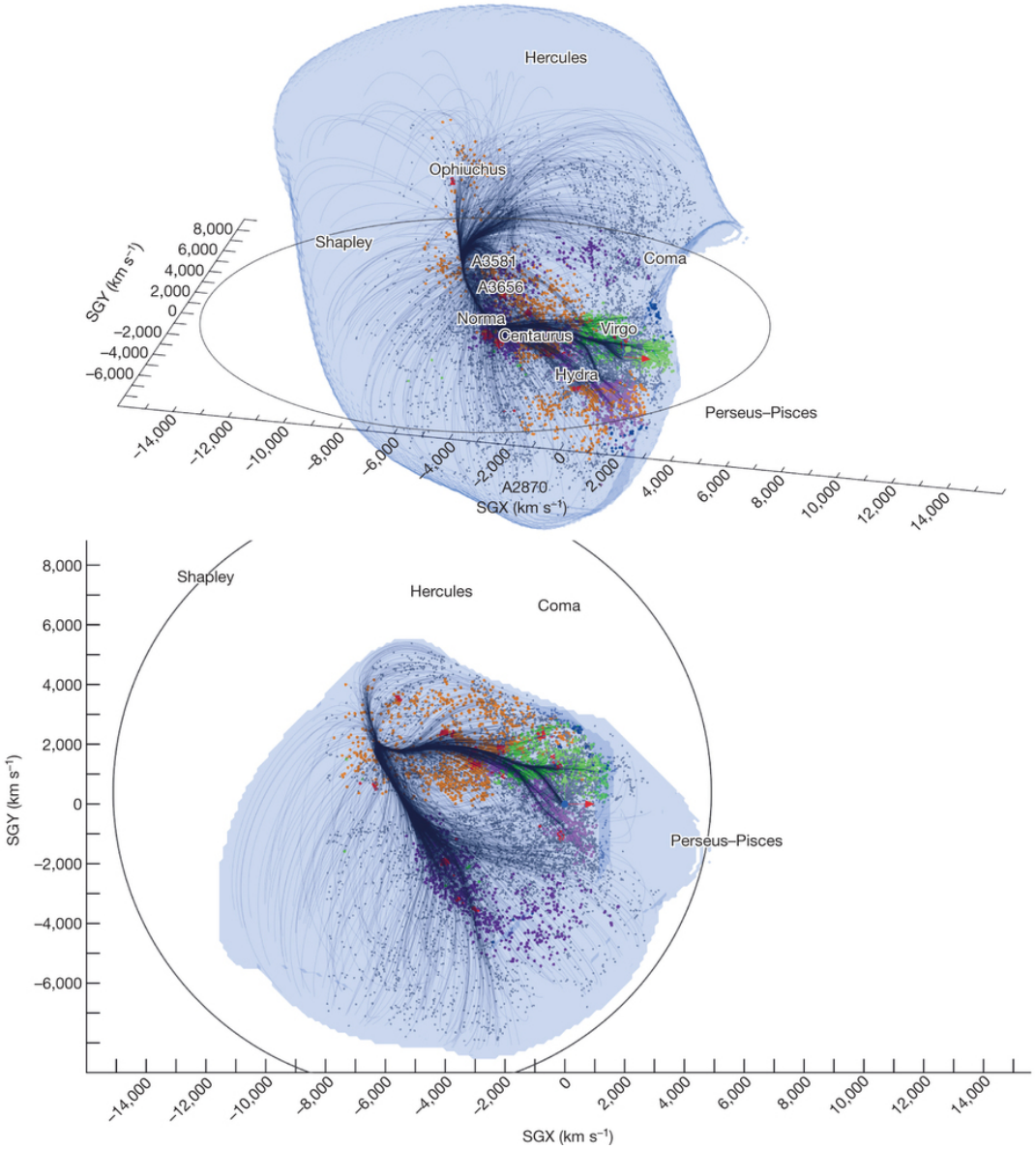

Figure 1.3: Overview of the Laniakea supercluster. Source: Tully et al. (2014)

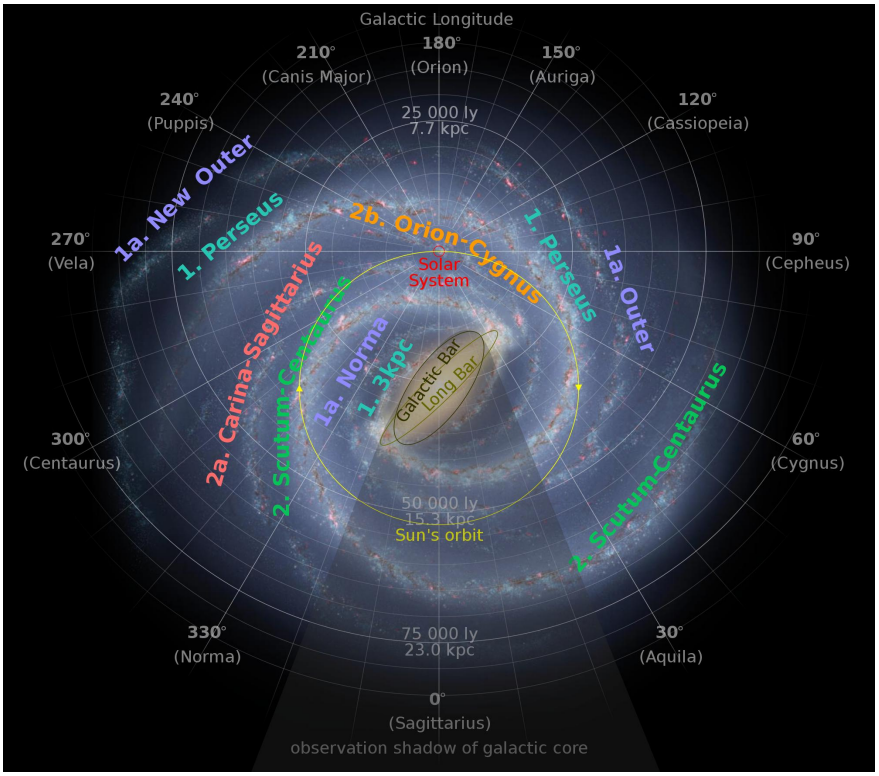

Figure 1.4: Milky Way map with position of the solar system. The obscuring dust in the Galactic Bar casts an observational shadow on all sources behind it at optical/NIR wavelengths. Source: NASA / JPL-Caltech / R. Hurt (SSC-Caltech).

2010). This translates into a period of about 240 million years, making it necessary to deal with these observational obstacles in order to gain insights on the Galactic Center region and obscured sources at optical/NIR-wavelengths. The ability to observe the nucleus of the Galactic Center behind this dusty veil made it one of the most prominent subjects in astrophysics and the detection of a central super-massive black hole (SMBH) even further raised interest in this target. This thesis aims at gaining further insights on the physical processes of this very interesting source, which is a current concern of astronomical science.

1.1 Nuclear Stellar Cluster

The Galactic Center is a very complex area, containing a huge amount of distinct objects and gaseous streams. Figure 1.5 provides a nice overview of its complexity and the amount of features. Molecular clouds absorb a large part of its radiation and are, therefore, associated with the dark areas in this image. Within this region of high object density reside massive star clusters, supernova remnants and at a few parsecs the circum nuclear disk (see Fig. 1.6). The central objects within the Galactic Center can be decomposed into a nuclear bulge of $1.4 \times 10^9\,\mathrm{M}_\odot$, covering the central hundreds

Figure 1.5: Composite image of the Galactic Center taken at Infrared (red, Mission: Spitzer Space Telescope), Optical (yellow, Mission: Hubble Space Telescope) and X-ray (blue, Mission: Chandra X-ray Observatory). Instrument: IRAC. Source: NASA, ESA, CXC, SSC, STScI, JPL-Caltech

of parsecs, an enclosed stellar disc (radius: $\sim 230\,\mathrm{pc}$, scale height: $\leq 45\,\mathrm{pc}$) and a compact nuclear stellar cluster (NSC) (Launhardt et al., 2002). This NSC is assumed to inherit a high amount of star formation derived from its strong UV-radiation and stellar luminosity function. The flattened NSC spreads over (4.2±0.4) pc (half-light or effective radius, enclosing half of the total emitted flux) with a mass of $(2.5 \pm 0.4) \times 10^7\,M_\odot$ and is rotating in the same direction as the Galactic Center (Schödel et al., 2014). Its misalignment of ∼10° is currently assumed to be caused by individual accretion events during the time of cluster formation (Schödel et al., 2015).

Schödel et al. (2007) report, that the dense and clumpy molecular ring, called the circum nuclear disk, orbits the gravitational center an radius of ∼1.6 pc with a velocity of $\sim 110\,\mathrm{km\,s^{-1}}$ (Guesten et al., 1987; Jackson et al., 1993; Christopher et al., 2005). Within this ring ionized gas forms three major streams, called the mini-spiral, which connects the disk with the central star cluster. NIR observations provide a clear view of the stars inside the mini spiral and currently provide, due to its proximity and angular size, the only observations of a cluster that can be resolved into individual stellar sources at milli-pc scales. The achievable detection limit only allows high magnitude stars at NIR wavelengths to be detected, that only account for about 1% of its total stellar population. These stars are mostly red/blue super-giants and all main sequence stars down to $\sim 2\,\mathrm{M}_\odot$.

According to Meyer (2008a), one of the first radio observations, offering the required observational precision and techniques to overcome the limiting obstacles, revealed the radio complex Sagittarius A which can be resolved into a supernova remnant (Sagittarius A East), an extended source (Sagittarius A West), which was identified with

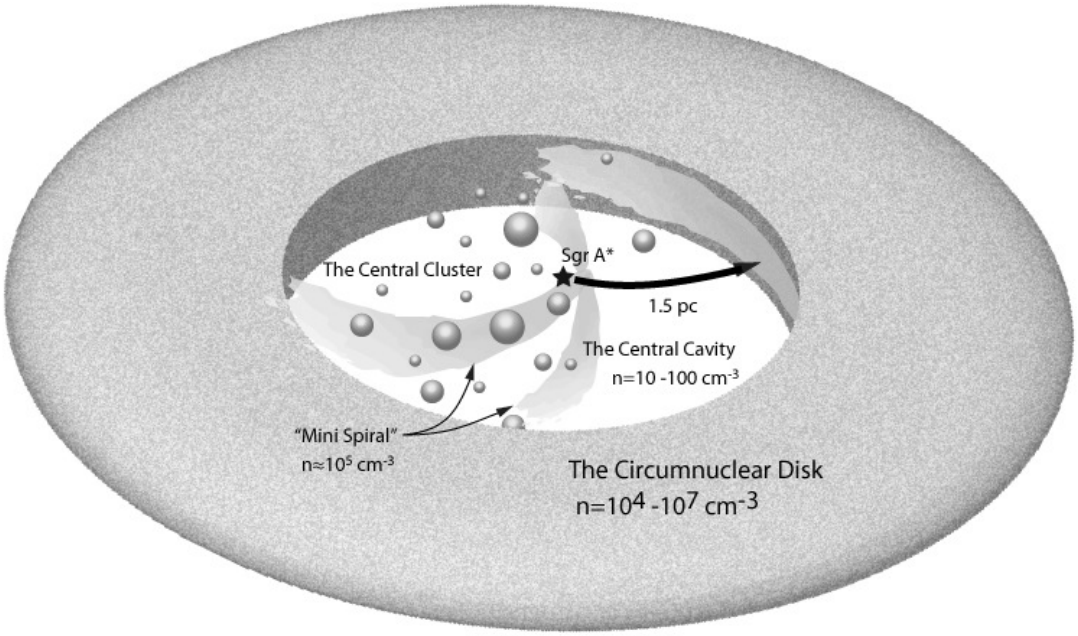

Figure 1.6: Schematic view of the Galactic Center. Relative positions of Sgr A* and the central cluster within the central cavity are shown within the circum nuclear disk. Source: (Goto et al., 2013).

the mini spiral and a very compact ($<1''$), bright radio source Sagittarius A* (Sgr A*) with unique properties (see Fig. 1.7) (Balick & Brown, 1974). The latter source was discovered to be the counterpart of electromagnetic radiation released by hot plasma close to a SMBH of $\sim 4.0 \times 10^6 M_\odot$ (see Sect. 2.1). This source is the main science target of this thesis and Sgr A* will in the following refer to the black hole together with its narrow neighborhood up to the radii of detected electromagnetic radiation originating from the matter within the black holes immediate gravitational influence. The focus of this work lies on the physical properties of this object and the theories that try to explain its energy production mechanism. This source has shown intensity outbursts that are discussed in detail in section 3.2. Special emphasis is put on the models trying to explain this flaring behavior.

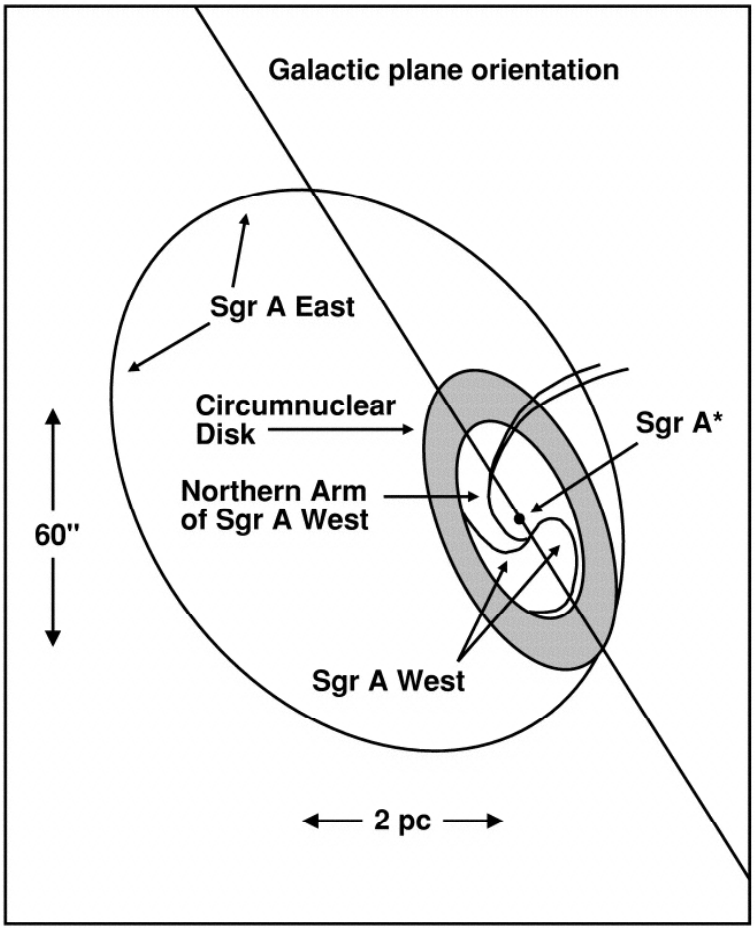

Figure 1.7: Schematic overview of the Sgr A complex. Source: Baganoff et al. (2003)

Chapter 2

Black Holes

The theory of black holes is an unconventional approach that needed great courage to propose and pursue such a groundbreaking idea. These must have been characteristics that John Michell (Michell, 1784) and Pierre Simon Laplace (Laplace, 1796) possessed when they introduced the idea of objects that provide such strong gravitational fields that are capable of confining objects and even electromagnetic radiation in their gravitational influence. As with most discoveries, the idea of black holes needed the fortunate mind of an inspired scientist to create a mathematical framework for this theory, long before any experimental hints pointing towards the true existence of such objects in nature could be observed. Einstein (1916) provided, with his general relativity, an instrument to describe the theory and Schwarzschild (1916) found the first mathematical solution for it. This mathematical framework and its success in the scientific community paved the way for many follow up theories, considering charged (Reissner, 1916; Nordström, 1918), spinning (Kerr, 1963) and both spinning plus charged (Newman et al., 1965) black holes.

Following the argumentation in Zamaninasab (2010a), the no hair theorem provides solutions of the Einstein-Maxwell equations in four space-time dimensions that can be uniquely characterized by three variables: mass, electric charge, and angular momentum. In a static case with a spherical symmetry, no angular momentum and no electric charge, the Schwarzschild metric (Schwarzschild, 1916) can be used to describe the environment of a black hole. The additional consideration of electric charge of the mass is included in the formalism of the Reissner-Nordström metric (Reissner, 1916; Nordström, 1918). A more generalized description of the Schwarzschild metric is provided by the Kerr metric and charged-spinning solutions by the Kerr-Newman-metric (Kerr, 1963; Newman et al., 1965). The latter is both a spinning generalization of the Reissner-Nordström and an expansion of the Kerr metric, considering electric charge of the mass.

Most of the massive objects in astrophysics are surrounded by plasmas which inherit charged particles. If this matter comes within the gravitational influence of a black hole it will start falling towards its center, and the charged particles will preferably couple with those of opposing charge, forming a neutral stream towards the center of gravitation. Therefore, in most cases only angular momentum needs to be accounted for and the charge of these particles can be neglected.

The most interesting physical effects occur at the singularities of these metrics. Following the Kerr equation, singularities appear at $\rho = r = 0$ ($\rho^2 = r^2 + a^2 \cos^2 \theta$)and at $r_\pm = 1 \pm \sqrt{1 - a^2}$, where $a = \frac{J}{M}$ is the angular momentum per unit mass. These singularities represent the outer and inner horizons. There are ongoing discussions

about the singularity at $r = 0$ which violates the rules of physics in the framework of general relativity. Some approaches try to accounted for this by a revised quantized version of general relativity. Within the Kerr metric two special regions can be defined, delimited by the marginally stable orbit, below which all matter will free fall towards the horizon and marked by the photon orbit, an orbit of particles with infinite energy per unit rest mass. The latter is the minimum scale at which photons might orbit the gravitational several times before they reach the observer, leading to weaker, time-delayed secondary images (Luminet et al., 1979).

After Einstein postulated his field equations, it still took until the late 1960s for the community until these objects reached the status of a real feature occurring in nature and not being only a mathematical consequence of this theory. The first experiments trying to find observational evidence for such objects, that were assumed to inherit strong X-ray radiation, was performed in 1962 by Riccardo Giacconi (Giacconi et al., 1962). But it took until 1965 for Bowyer et al. (1965) to perform airborne X-ray observations of Cyg X-1, surveying sources above the atmosphere with rocket-mounted Geiger counters, that revealed the first candidate of a black hole. Further observations of the Cygnus region proofed existence of a secondary radio source HDE 226868 close to the origin of its X-ray radiation. The orbital period of this binary system was determined to be $(5.600 \pm 0.003)\,\mathrm{d}$ and implied that the secondary source is a black hole of about $10\,M_\odot$ (Bolton, 1972). The results showed that these very bright and compact objects posses much more energy than can be produced by nuclear fusion. A solution for this problem was found by Schmidt (1963) and Shakura & Sunyaev (1973) who explained this excessive high energy by the release of gravitational bounding energy of the matter accreting towards a very compact gravitational center.

This started a variety of observations which discovered many candidates of black holes in form of extremely luminous and compact sources that are, in some cases, located at the very center of galaxies. Most of these active galactic nuclei (AGN) form jets originating from their compact centers visible in the radio and sometimes in the optical. Lynden-Bell & Sanitt (1969) related the power of these radio counterparts with the strong gravitation of black holes. Follow-up observations investigated the kinematics of stellar and ionized gas close to galactic nuclei and found more evidence for black holes existing in the centers of galaxies (Kormendy & Gebhardt, 2001; Ferrarese & Merritt, 2000). This raised the question whether such a strong gravitational object could also be present in the Milky Way.

2.1 The Galactic Center Black Hole

Observations of the Galactic Center are limited by obscuring dust and gas that affects the electromagnetic radiation originating from sources within. But the observational methods are able to overcome these limiting factors to some extend and are capable to produce very high angular resolution images of this region. Within the central parsec around the black hole the stellar population consists of early-type and old evolved stars (Schödel et al., 2009). Peebles (1972) state that the stellar density within a relaxed

dense stellar cluster will be increasing towards the influence of a black hole following a power law of $\rho \propto r^{\gamma}$.

According to Meyer (2008a), an old stellar population outside of the black hole's radius of influence is expected to be in a relaxed equilibrium state, since the relaxation time of $\sim 4 \times 10^8$ years is much smaller than the age of these objects. Therefore, the stellar density will follow an isothermal profile and the stellar distribution of these stars should be described by a single energy variable which is proportional to r^{-2} (e.g., Binney & Tremaine 1987). But this power law breaks at the radius of influence of the central black hole at about 2.3−3.8 pc (Feldmeier et al., 2014; Chatzopoulos et al., 2015), which is a solid evidence for its existence. Numerical simulations provide a γ in the range of $-3/2 \geq \gamma \geq -2$ for a dynamically relaxed star cluster depending on the mass of considered objects (Young, 1980; Alexander, 1999). Observations show that within the central $\sim 0.25 - 0.35$ pc this power law breaks and follows $\gamma = -1.3$ to -1.4 (Genzel et al., 2003a). Schödel et al. (2007) report a more accurate value of $\gamma = -1.20 \pm 0.05$ at $6''$. Later observations provided power-law indices for two stellar groups discerned by their masses. Values of $\gamma = -3/2$ (Alexander, 2005) to $-7/4$ (Quinlan et al., 1995) can be found for lower mass stars, while values of $-7/4$ are valid for the weak mass segregation regime (Alexander & Hopman (2009); see also Genzel et al. (2010) and references therein). Rare high-mass stellar objects on the other hand follow a power law with an index of $-2 \geq \gamma \geq 11/4$ (Preto & Amaro-Seoane, 2010).

In contradiction to theoretical predictions, the density of old and dynamically relaxed stars was found to be flat within a projected radius of ≈ 0.5 pc (Buchholz et al., 2009; Do et al., 2009; Bartko et al., 2010). Current theories try to explain this circumstance by either assuming a common representative density distribution for all stars within the NSC (Merrit & Szell, 2006; Merrit et al., 2010), a hidden cusp (Dale et al., 2009; Amaro-Seoane & Chen, 2014) or a migration of black holes towards the center that expels lighter stars (Löckmann et al., 2010).

Meyer (2008a) reports, that in addition to intuitively expected old, low-mass stars in a relaxed state, a population of younger stars with mass ranges of $30-100\,M_{\odot}$ can be found (e.g., the IRS 16 cluster) which appear to be a population of stars evolved away from the main-sequence and are probably approaching the state of Wolf-Rayet stars (Krabbe et al., 1995). These stars are expected to have formed around $(2-9) \times 10^6$ years ago and thus, haven't evolved to their equilibrium state yet. The fact that these stars have formed recently in the vicinity of Sgr A* is still under investigation and needs proper explanation. These massive early-type stars located in the inner $1''$-$10''$ are found within two counter-rotating thin discs (Genzel et al., 2003a; Paumard et al., 2006). The discussion of the existence of the counter-clockwise disc is still not settled (Lu et al., 2006), but it is assumed to have a radius of $4''-7''$ (Genzel et al., 2003a; Paumard et al., 2006), which is less compact than the clockwise disk at a radius of $2''-4''$. These stars are still under discussion and several models like stellar mergers, their origin from a former infall and dissolution of a young cluster with an intermediate central black hole or formation of stars within the accretion disc are considered (e.g. Ghez et al. 2003a; Eisenhauer et al. 2005; Paumard et al. 2006).

While theories about the origin of the S-stars in the central arcsecond are still

unsettled, their proper motions yields information about the gravitational center and their orbital parameters can be used to determine the interacting mass distribution. The pioneer experiment of Eckart & Genzel (1996) paved the way for many follow-up observations trying to further put constraints on the position and mass of the central high mass source Sgr A*. There are several suitable stars within the Galactic Center that offer a short observable periodicity, while being well above the detection limit. Acceleration measurements (Ghez et al., 2000) and fitting Keplerian orbits of six S-stars within the central arcsecond led to the current accepted theory of a compact and heavy dark mass object which is assumed to be a SMBH. Fitting the enclosed mass versus radius, a black hole with a mass of $(3.6 \pm 0.4) \times 10^6\,M_\odot$ (Ghez et al., 2003b) ($\sim 4 \times 10^6\,M_\odot$, Gillessen et al. (2009)) concealed in a radius of $\leq 0.6\,\mathrm{mpc}$ at $\sim 8\,\mathrm{kpc}$ provided the best fit to this graph (Eckart & Genzel, 1997; Eckart et al., 2002; Schödel et al., 2002; Ghez et al., 2003c). The estimation errors currently amount to $< 10\%$ in mass and $< 5\%$ in distance (Schödel et al., 2015). The velocity dispersion as a function of their radial separation from the gravitational center are in good agreement with expected Keplerian orbits in the reach of a point-like mass (Eckart & Genzel, 1996). S2/S0-2 is the best candidate among these objects and provides the most accurately determined orbit around Sgr A*, which has an eccentricity of 0.87 and a period of 15.2 yr (see Fig. 2.1). This star will have its next pericenter passage around the Galactic Center in 2018 and offers a great opportunity for subsequent observations (e.g., Genzel et al. 2010; Schödel et al. 2014 and references therein). At the time of this thesis, size and motion measurements of this black hole have been performed by analyzing orbital parameters of about two dozen stars (see Fig. 2.2).

The mass density as a function of projected distance from Sgr A* excludes other possible models like a dark mass cluster or other exotic particles (Schödel et al., 2002, 2003; Ghez et al., 2005; Eisenhauer et al., 2005). It has to be kept in mind that kinematic mass estimations underestimate the mass by about 30-50% (Schödel et al., 2015) and are subject to several biases, such as anisotropy effects and the flattened stellar core of this cluster (Fritz et al., 2014). Since the first evidence of black holes in galaxies, the current picture evolved to a point in which it is assumed that most galactic nuclei, or even all, contain a black hole of very high mass at their centers (e.g., Richstone et al. 1998; Gebhardt et al. 2000; Ferrarese & Merritt 2000; Gültekin et al. 2009; Seth et al. 2014).

2.2 Alternatives to a Galactic Center Black Hole

According to Genzel et al. (2010), there are also alternatives, besides a black hole, that could explain the very high mass density in the Galactic Center. The current literature provides a strikingly consistent picture of a black hole at the position of Sgr A* and is the most reliable explanation, but these alternatives should not be excluded to gain a complete overview.

A first alternative explanation was the existence of a dark cluster, consisting of faint stars, dark stellar remnants or other collisional matter. The first detections of

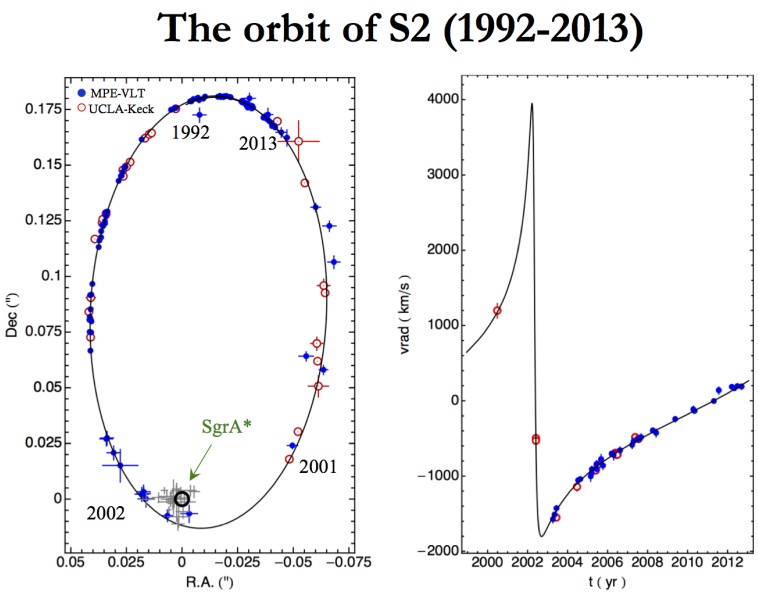

Figure 2.1: Orbit of S2 between 1992 and 2013 with respect to Sgr A*. Source: MPE-IR Galactic Center Group (Genzel, R.) and UCLA group; http://www.mpe.mpg.de/369216/The_Orbit_of_S2.

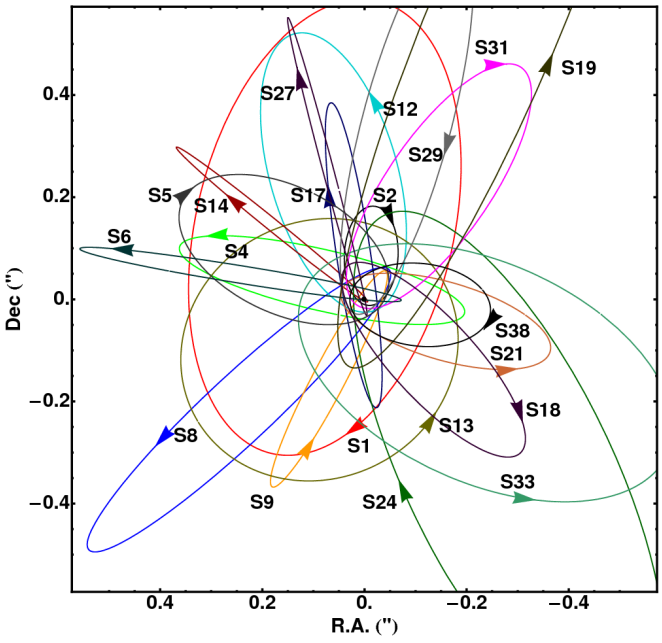

Figure 2.2: Illustrative orbits of stars in the central arcsecond around Sgr A*. The coordinate system origin is defined as the position of Sgr A*. Source: (Gillessen et al., 2009).

orbiting S-stars within $\leq 0.02\,\mathrm{pc}$ implied a density of $\geq 10^{12}\,\mathrm{M_\odot pc^{-3}}$ in 1996−1998 (e.g., Eckart & Genzel (1996)). This high density causes the enclosed objects to collapse or evaporate on a time scale of $\sim 10^{7-8}\,\mathrm{yr}$, due to collision and relaxation (Maoz, 1998). This short time scale makes such a configuration hardly probable and improved orbital measurements until 2002 (e.g., Schödel et al. 2002) raised the density to be $\sim 10^{16}\,\mathrm{M_\odot pc^{-3}}$ which completely excludes this scenario.

Viollier et al. (1993) proposed that compact fermion balls might be present in galactic nuclei and quasi-stellar objects (QSO). These balls would consist of hypothetical massive neutrinos supported by degeneracy pressure. Such a configuration would require the fermion ball at the position of Sgr A* to extend over 15 light days (Munyaneza et al., 1998) and therefore, exceed the orbits of the stars S2 and S14 by a factor 36. While more massive fermions could cause a smaller region, the required masses of such particles would exceed the current limits by a factor 2×10^5.

A boson star has also been considered by Torres et al. (2000) as a possible scenario to account for the high mass in the Galactic Center. These stars can be realized at the masses of black holes, but due to their weakly self-interacting particles, the formation process of such an object is unclear. The most contradictory aspect of this hypothesis is the presence of baryonic accretion, which occurs frequently in the Galactic Center and would cause such a star to collapse into a black hole. Despite this contradictory evidence, future observations at improved resolutions should be capable to discriminate between the boson star and black hole scenario, because a boson star will be a factor of a few larger than the event horizon of a black hole, as long as the general relativity is still applicable for the properties found at Sgr A*. If this is not the case, some sources propose that, if quantum phenomena are considered, the matter will be evaporated by Hawking radiation before it is able to condense into a black hole (Vachaspati et al., 2007).

Alternatively, quantum phase transitions could cause the formation of a "gravastar" (Mazur & Mottola, 2001), which is a high mass object, that is capable of blue-shifting incident electromagnetic radiation to a wavelength beyond the Planck length. This is, therefore, no longer measurable outside of this region and results in a central gravitational vacuum surrounded by a Bose-Einstein-condensate. Furthermore, a "dark energy" star was proposed by (Chapline, 2005), which has a central de Sitter vacuum solution of general relativity with $\rho = -p$ within $R_{\mathrm{grava}} \sim R_s + O(\lambda_P = 1.6 \times 10^{-33}\,\mathrm{cm})$ at the scale of the event horizon of a black hole. The similar scale makes it very hard to discriminate this hypothesis from the black hole scenario by observational evidence (Abramowicz et al., 2002; Broderick & Narayan, 2006b).

This thesis assumes the currently accepted black hole scenario for Sgr A*, but this section gives an overview of alternative theories that are capable of describing the properties of this source. The next generation of telescopes (e.g., Event Horizon Telescope) are currently close to commissioning. Their improved resolution will make it possible to verify or exclude the most likely super-massive black hole in the Galactic center and theories, like a boson star. While others, such as a "gravastar" or "dark energy" star, need other parameters to be analyzed.

Chapter 3

Sagittarius A*

The Galactic center offers a unique opportunity to study phenomena and physical processes as they occur in many other galactic nuclei at an unparalleled resolution and sensitivity. The presence of a SMBH at the position of Sgr A* is currently proven beyond reasonable doubt and a radio source at the expected position can be associated with this mass. The observable electromagnetic radiation is not originating from the black hole itself but rather from hot plasma within the radius of its gravitational influence. At these scales accreting matter is the source of such radiation at NIR, radio and X-ray wavelength.

Since our solar system is located within the Galactic Plane and electromagnetic radiation has to pass through its disc (see Chap. 1), observations of the GC are subject to significant interstellar extinction. Following the argumentation in Meyer et al. (2006), this extinction amounts to $A_V \geq 30$ mag at visible, 2-5 mag in the NIR (2.2 μm) and has a minimum around 3-5 μm (Nishiyama et al., 2008; Fritz et al., 2011). Observations of the GC are even more challenging due to the fact that interstellar extinction varies significantly on short angular scales of a few arcseconds (Schödel et al., 2010). The stellar density per square arcsecond within the NSC is in the range of several tens (at ≤ 1 pc) to a few objects (at ≈ 100 pc). This crowding leads with the current resolution of telescopes to a brightness limit for stellar counts of K$\leq$15 (Schödel et al., 2015). The source associated with the SMBH in the center of our galaxy is continuously above the detection limit of current radio single dish and interferometric telescopes, which is only true for NIR observations during its flaring states. Sgr A* is also pretty faint compared to other objects of this class, because of it being about nine orders of magnitude lower than its Eddington limit. This is the luminosity limit above which the radiation pressure will exceed the hydrostatic pressure and electrons will be driven away from the source. This arises from its accretion rate being about four times lower than the Eddington accretion rate, which can be measured by tracing gas emission at X-ray frequencies and amounts to $\sim 10^{-5} M_\odot yr^{-1}$ (Baganoff et al., 2003). At these low accretion rates the standard accretion theories would over-predict the luminosity of this object, and thus, the community was in need of a new theory, which are discussed in sections 3.3 and 3.4.

Along with interstellar scatter broadening effects at wavelength above 7 mm (see Sect. 5.3.1), Sgr A* has a low declination of $-29°$ and is, thus, not observable continuously with all telescopes of the Very Long Baseline Array (VLBA), located on the northern hemisphere (see Fig. 5.1), which was used to perform the observations described in this thesis (see Chap. 5.1). The influence of the atmosphere at low declinations is quite strong (see Chap. 5.3) and it is a challenging task to achieve high

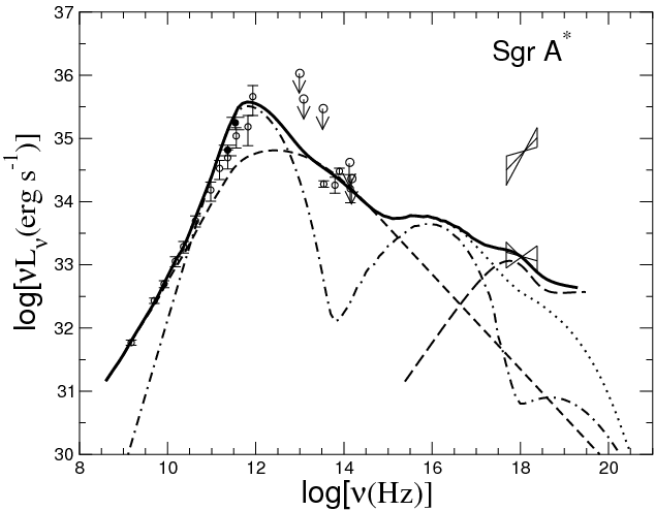

Figure 3.1: Observed spectrum of Sgr A*. Source: (Yuan et al., 2003)

quality images of this source at X-ray, NIR and radio frequencies.

3.1 Spectrum

The Galactic center source Sgr A* has a complex frequency depended spectrum that shows several bumps, which are most probably caused by different energy production mechanisms of the black hole associated with this source (see Fig. 3.1). This makes it a challenging task to find a fitting model that explains the energy production mechanism at different wavelengths. Yuan et al. (2003) provide a model for the quiescent emission of Sgr A* based on radio, NIR and X-ray observations. Following the argumentation in Meyer (2008a), the spectrum raises at higher frequencies towards the sub-mm bump which is assumed to be caused by a self-absorbed synchrotron emission at the innermost region of the accretion flow. Emission at lower frequencies is assumed to be originating from a non-thermal halo surrounding the black hole. The steep drop at sub-mm wavelengths is caused by the transition from optically thick to thin, causing the inner accretion region to become visible and revealing its synchrotron emission. Sgr A* is highly variable at NIR to X-ray wavelengths. Therefore, the power law index is most probably also flux dependent and has to be considered (Gillessen et al., 2006; Hornstein et al., 2006). While it is possible that the variable synchrotron emission radiates in the keV part, a more likely explanation is an upscattering by IC scattering to the X-ray regime of emitted photons on their relativistic host electrons.

3.2 Flare activity

Flux evolution studies of Sgr A* revealed this source to be highly variable at all observable wavelengths with the strongest effect at NIR and X-ray frequencies. The first obstacle in observing the variability of this source is how to discriminate between an

intrinsic flux variation and those caused by statistical variations between individual observing frames. The statistical flux variation of a non-variable source is expected to be well fitted by a Gaussian or normal distribution, while any deviation from this behavior is a strong evidence for a true flux variability. Witzel et al. (2012) have performed an analysis of ten non-variable calibration stars close to Sgr A* and show that their number of measurements in relation to their flux densities are all well fitted by a Gaussian distribution (see Fig. 3.2). Sgr A* however can not be fitted by such a distribution within observational uncertainties and is, therefore, considered to be intrinsically variable.

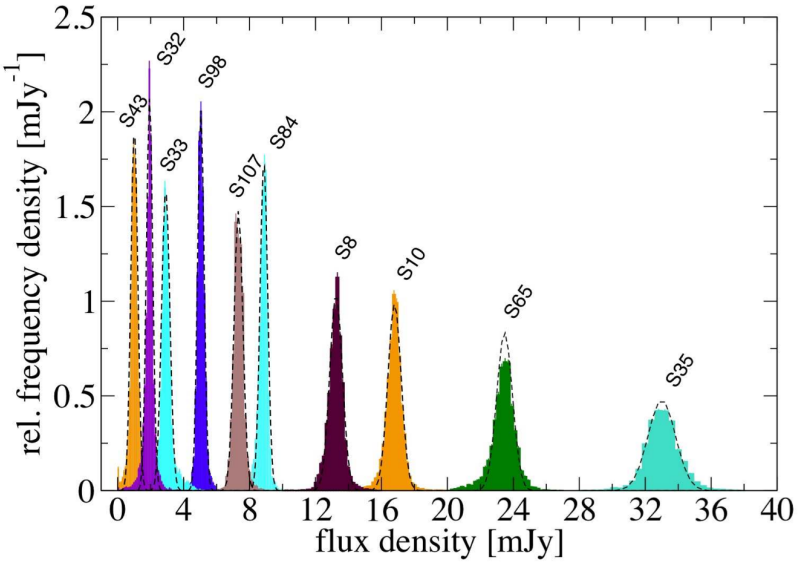

Figure 3.2: Normalized flux density histogram of ten non-variable calibrator sources in the Galactic Center. The dashed lines represent Gaussian fits of the distribution. Source: (Witzel et al., 2012).

Folowing Meyer et al. (2006), the first detections of a flare at X-ray wavelengths have been performed by Baganoff et al. (2001). The authors detected a rare strong flux variation of a factor five within less than ten minutes. Such a strong flare can be attributed to an emission region of only a few Schwarzschild radii based on light crossing arguments. At NIR frequencies the first detection of emission together with a flare of Sgr A* has been performed by Genzel et al. (2003b), who describe a flux variation raising on very short timescales towards its maximum and then falling in the same rapid behavior back to its initial value. These observations also suggest a quasi-periodic substructure superimposed to the flare activity. This substructure can be fitted by a power law, suggesting a quiescent phase of Sgr A* to be caused by a sequence of low intensity flares (Eckart et al., 2004, 2006b).

It is now established that the intensity of Sgr A* shows spontaneous flux density outbursts at radio to X-ray frequencies, commonly referred to as flares (Mauerhan et al., 2005; Marrone et al., 2006; Yusef-Zadeh et al., 2008; Eckart et al., 2008a,b,c, 2009,

2012; Lu et al., 2011b; Miyazaki et al., 2012). These intensity irregularities appear on timescales ranging from 1-2 hours (main-flares) down to 7-10 minutes (sub-flares) (Eckart et al., 2006a), with stronger activity at shorter wavelengths (Baganoff et al., 2001; Genzel et al., 2003b; Aschenbach et al., 2004; Ghez, 2004; Eckart et al., 2006b,c). The underlying physical mechanism leading to these flares is still is the main subject of this thesis and will be discussed in the following sections (3.3 and 3.4).

3.3 Quiescent models

The physical processes, that cause the electromagnetic radiation of Sgr A* are is still under investigation. While black hole accretion is commonly assumed to be the origin of its radiation, there are several proposed models that try to explain the observed broad band quiescent emission of Sgr A*. Following Lu (2010), the currently most favored ones are Bondi-Hoyle type models (Melia, 1994; Melia & Falcke, 2001), which explain radiation by an accreting gas flow, advection-dominated accretion flow (ADAF) and radiatively inefficient accretion flow (RIAF) (Narayan et al., 1995, 1998; Quataert, 2003; Yuan et al., 2002, 2003, 2004). Different variants of ADAF models have been discussed but are less favored for Sgr A*, such as convection-dominated accretion flows (CDAF) (Quataert & Gruzinov, 2000; Narayan et al., 2000, 2002; Ball et al., 2001; Igumenshchev, 2002) and advection-dominated inflow-outflow solutions (ADIOS) (Blandford & Begelman, 1999), as well as ejection-dominated accretion flow (EDAF) in form of a jet plus wind model (Donea et al., 1999).

In particular, the Bondi-Hoyle models explain the radiation of Sgr A* by spherical free-fall accretion of plasma into the black hole. This causes a Keplerian disc to be formed at small radial scales. The process is assumed to have a low radiative efficiency because the time scale for radiative cooling is much larger than the accretion time of protons falling into the black hole. Therefore, only electrons have enough time to radiate before they get accreted into the black hole. These electrons only carry a fraction of the total energy and can, therefore, explain the observed low luminosity of Sgr A*. A major disadvantage of these models is that the accreting gas is assumed to have no angular momentum and is, thus, just a simple approach of the true underlying physical process.

As described in Meyer (2008a), the ADAF model, proposed by Narayan & Yi (1994), can explain the spectrum of Sgr A* by a radiatively inefficient accretion flow of two temperatures with suppressed radiation. The accretion flow of this model inherits electrons that are decoupled from non-radiating ions. These ions are accreted into the black hole and carry the potential energy.

Many variants of the RIAF models can also match the observed spectrum of Sgr A* (see Fig. 3.1) and are still under investigation (Blandford & Begelman, 1999). Yuan et al. (2003) proposed an enhanced version of the ADAF model by adding a significant outflow and non-thermal particles, as well as increasing the turbulent heating. This approach and its ability to adequately explain the spectrum of Sgr A* developed the picture, based on energy arguments, that some kind of outflow needs to be present (e.g.,

Loeb & Waxman 2007). The low frequency radio emission of Sgr A* is assumed to be originating from outside of the innermost region and is likely from a non-thermal halo surrounding the black hole. Some authors relate this expanding halo to a jet, which might be hidden by the scattering screen (Markoff et al., 2001, 2007). It is currently unclear whether there is a short jet or a non-collimated outflow.

ADAF models on the other hand consider an angular momentum and viscosity of the infalling plasma. In this scenario the low luminosity of Sgr A* is explained by the circumstance that electron heating is inefficient. Viscous energy only heats ions and since their coupling to electrons is weak at low accretion rates, most of the viscously dissipated energy is stored in the medium, that is falling into the black hole. These ADAF models work quite well to explain mid- to high-frequency spectra but underpredict fluxes at lower wavelengths (Narayan et al., 1998).

As described by Lu (2010), radiatively inefficient models, that assume a mixed population of thermal and non-thermal electrons, have been proposed to explain the high frequency spectrum of Sgr A* (Özel et al., 2000; Yuan et al., 2003). Such a set of particles is reasonable since Coulomb collisions and synchrotron self-absorption are inefficient thermalization processes. The presence of the non-thermal electrons leads to a larger source size and alters the frequency dependence of the brightness temperature up to $\sim 10^{11}$ Hz. At high radio frequencies linear polarization detections suggest a low accretion rate. This can be explained by the circumstance that a majority of the initial mass is lost in convective circular motions or a flow which leads to a low gas density and therefore, low accretion rates at smaller radii. This is an advantage of the RIAF over ADAF models. The RIAF hypothesis can explain many feature of the spectrum of Sgr A*. In this model non-thermal electrons lead, by synchrotron emission, to the observed radio and IR spectrum. Synchrotron emission of thermal electrons can produce the sub-millimeter bump, and, taking bremsstrahlung emission at radii $\sim 1''$ into account, even the extended quiescent emission at X-ray frequencies can be explained (Quataert, 2002).

Jet models on the other hand can also adequately describe the quiescent spectrum of Sgr A* by invention of a nozzle component (Falcke & Markoff, 2000). Jet formation is a common process and because it is capable of mitigating the angular momentum of an accretion disk it is a commonly accepted model. The nozzle component forms a collimated plasma feature that is accelerated away from the black hole. This mechanism is also capable of explaining the sub-mm bump and the high energy range of the spectral energy distribution (SED) by synchrotron and inverse Compton (IC) emission originating in this component. In this context a narrow electron energy distribution is required to explain the observed IR SED. A problem with this jet model is its inconsistency with the extended non-thermal quiescent X-ray emission of Sgr A*.

In case of a mixed Jet-ADAF model (Yuan et al., 2002), a coupled jet together with an accretion disc model is used in which Bondi-Hoyle accretion of a hot plasma feeds an ADAF accretion flow. The jet is formed by a small fraction of the accretion flow which is ejected close to the black hole. The resulting spectrum of Sgr A* will be a superposition of the jet and ADAF emissions and is capable of explaining the predicted X-ray slope and the observed radio spectrum.

3.4 Flare models

The compact radio source Sgr A* is showing spontaneous intensity variations in a (quasi-)periodic behavior at X-ray to radio wavelengths (see Chap. 3.2). Following Lu (2010), IR flares show a high degree of linear polarization and a rather constant flare intensity, which is an indication for a synchrotron origin of this effect. X-ray flares offer a wide range of peak intensities and an undetermined spectrum, making it a challenging task to generate an explanatory model and put constraints on statements regarding the underlying mechanism. The current most probable origin of these flares are local events, rather than a global increase of its accretion activity (Markoff et al., 2001).

X-ray flare models favor IC scattering processes over synchrotron models (Eckart et al., 2004, 2006b; Liu et al., 2006). The fact that the cooling times are much smaller than the typical X-ray flare lengths would require very high energy electrons to be injected continuously into the accretion flow, which is very unlikely to happen and therefore, are a contradiction to a synchrotron origin of the X-ray spectrum (Dodds-Eden et al., 2009). Considering a pure synchrotron model for IR- and X-ray flares, Yuan et al. (2003, 2004) propose that a part of the electrons could be heated/accelerated by magnetic reconnection, shocks and stochastic acceleration which cause an IR flare through synchrotron emission. Whereas, in case of a synchrotron + synchrotron self-Compton (SSC) model, an IR flare is produced by synchrotron emission from a single power law distribution of accelerated electrons. While self-Comptonization of IR photons can account for the X-ray flares in this scenario.

Meyer (2008a) reports, that a SSC model is capable of describing the flaring state of Sgr A* by considering up-scattered sub-mm photons, originating in a compact component. In this context the observed X-ray emission can be explained by IC scattering of the THz-peaked flare spectrum by relativistic electrons (Eckart et al., 2004, 2006b). The IR emission mechanism in this model is more complex and is a combination of synchrotron and SSC emission. There are indications of an exponential cutoff of the NIR/MIR synchrotron spectrum, allowing an explanation of the variable and red spectral indices at NIR wavelengths (Gillessen et al., 2006). The main mechanism causing X-ray flares is assumed to be SSC which also explains that NIR flares appear more frequent. Radio and sub-mm flares show indications for the variability to appear on longer time scales than their NIR and X-ray counterparts. This is still under discussion and another aspect, why multi wavelengths observations at radio/sub-mm and NIR/X-ray will produce revealing results on this topic. Amplitudes and time scales of NIR/X-ray and radio flares, are consistent with an expansion and adiabatic cooling mechanism of the emitting material (Yusef-Zadeh et al., 2006b). Yusef-Zadeh et al. (2006a) also try to explain the X-ray flares by IC scattering of IR and sub-millimeter photons.

According to Lu (2010), a hot spot model is an alternative approach to explain the flaring activity of Sgr A* (Broderick & Loeb, 2006a; Meyer et al., 2006; Eckart et al., 2006c; Trippe et al., 2007; Eckart et al., 2008a). This model is supported by a correlation of the NIR flaring activity with polarization changes (Zamaninasab et al., 2010b; Nishiyama et al., 2009). Even though it only considers a single frequency, it has

the advantage of explaining the quasi-periodic nature of these flares by matter orbiting the inner parts of the accretion disc (e.g., Genzel et al. 2003b). The hot spot model proposed by Yuan et al. (2009) describes, in analogy to the coronal mass ejection of the sun, that magnetic flux ropes can be formed in the accretion disc by Parker instabilities (see Fig. 3.3). If this system looses its equilibrium stability, the material is rapidly expelled and the flux rope is propelled away from the accretion disc.

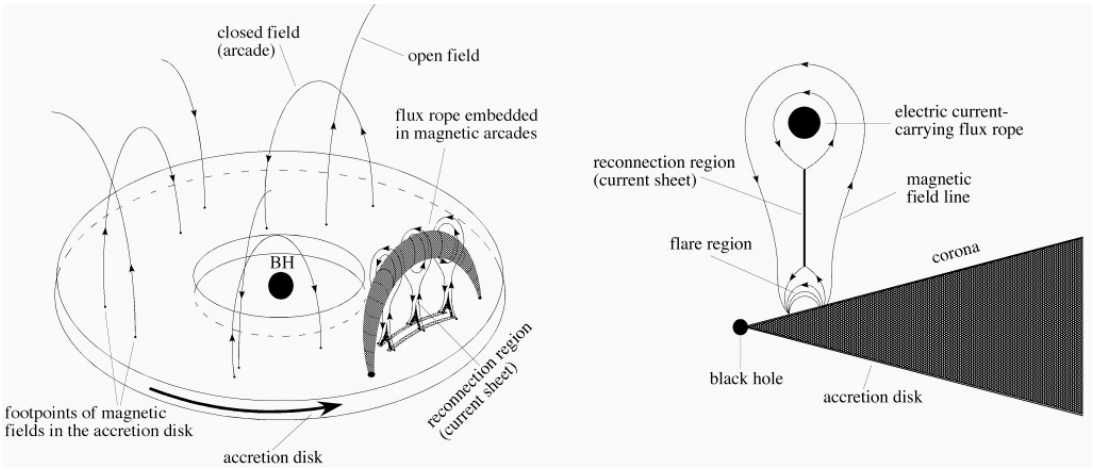

Figure 3.3: Illustration of the hot spot model proposed by (Yuan et al., 2009). A flux rope can be formed as a result of the foot point motion and subsequent magnetic reconnection. This feature can be ejected and results in a flare. Source: (Yuan et al., 2009).

Another currently discussed model is a temporary jet anchored at Sgr A* (e.g., Markoff et al. (2007)). A jet can be induced by an increase in accretion rate compared to quiescent states or by other instabilities in the accretion flow. A mixed Jet-ADAF model, as it has been proposed by Yuan et al. (2002), is also capable of explaining the rapid variability of Sgr A* at short time scales by strong emission from a jet, dominating the bremsstrahlung from the ADAF.

There are several parameters that can be used to discriminate between these flare models. Relativistic Magnetohydrodynamics simulations predict a constant size and shape of the Sgr A* emission region (e.g., Chan et al. 2009). An adiabatic expanding feature will be detectable in a change of the morphology and/or FWHM. According to Zamaninasab et al. (2008), a steady, asymmetrically located (with respect to the emission center) or orbiting expanding feature, as described in the hot spot model, would also be detectable by a position wander (Broderick & Loeb, 2006a; Broderick & Narayan, 2006b; Paumard et al., 2006; Zamaninasab et al., 2008; Hamaus et al., 2009). In this case the increased asymmetry of the source will cause non-zero closure phases and would also reflect periodic changes in source structure on the orbital time scales. Therefore, the best properties to investigate the nature the described flare activity are the position, the morphology and the FWHM Gaussian size of the compact radio source Sgr A*. Several authors have already tested the position wander at mm, sub-mm and NIR wavelengths, and could rule out hot spots brighter than 30% of the total 7 mm intensity at radii exceeding $15GM_{Sgr\,A*}/c^2$ Reid et al. (2008).

Chapter 4

Radio interferometry

Astronomers studied celestial sources for centuries at optical wavelength, but observations at radio bands have not been performed until the first approach of Jansky (1933). The Earth's atmosphere contains high amounts of H_2O, CO_2, O_2 and O_3 that absorb a significant fraction of the incident electromagnetic waves. This leaves only a few frequency windows, that can be used for Earth bound observations (see Fig. 4.1). Since the radio window offers a very wide and transparent wavelength regime, this band was a natural choice besides optical frequencies. Observing through this window opened a whole new astronomical science area to study effects not observable at shorter wavelengths. While longer wavelengths offer poorer angular resolution, single dish telescopes could only achieve resolutions up to 10 arcmin. According to Kellermann & Moran (2001), the discouraging low resolution at radio frequencies hindered progress in this area until Reber (1944) published a map of Galactic radio emission at a resolution of 12° and reported a first detection of the radio galaxy Cygnus A (Reber, 1948).

This has proven astronomical radio science being capable of producing relevant scientific results and raised interest in higher resolutions at these wavelengths. The region within which the variance of the difference of the phases at two points along the wavefront equals $1\,\mathrm{rad}^2$ is much higher at radio than at optical frequencies (3 cm at 0.5 μm compared to 600 m at 1 cm). This translates into a fluctuation time scale of 3 ms (optical) and 60 s (radio), which make it much easier to implement data processing algorithms at longer wavelengths (Kellermann & Moran, 2001). Therefore, interferometry at these wavelengths is easier achievable, but full imaging was still impossible until the invention of aperture synthesis techniques (see Sect. 4.2). Longer wavelengths additionally offer more convenient mechanical tolerances on telescopes and, thus, lower the challenges in constructing telescopes capable of diffraction limited imaging at resolutions up to 0.001 arcsec. The interesting discovery that many sources still remained point sources at this improved resolution raised the need of even further improvements in terms of resolution.

4.1 Principle of radio telescopes

Radio telescopes are in many ways equal to ordinary radio receivers, but since the desired signals are much weaker, they have to be processed before analysis. The following section is based on Klöckner (2014) and Klein (2006). Incident electromagnetic waves are reflected on the primary parabolic onto a secondary reflector and then focused to a feed horn. The signal is then passed on to the processing hardware. A basic simple

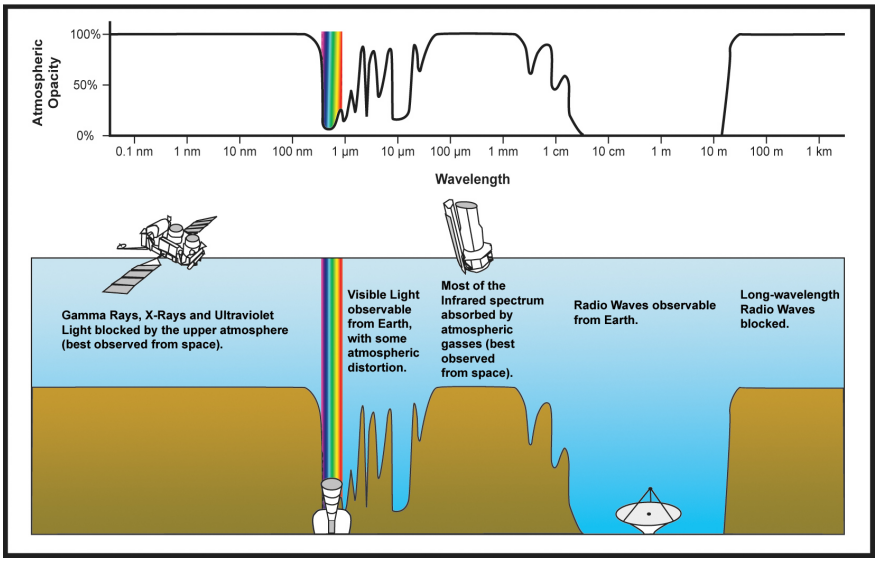

Figure 4.1: Atmospheric opacity as a function of wavelength. Source: NASA/IPAC

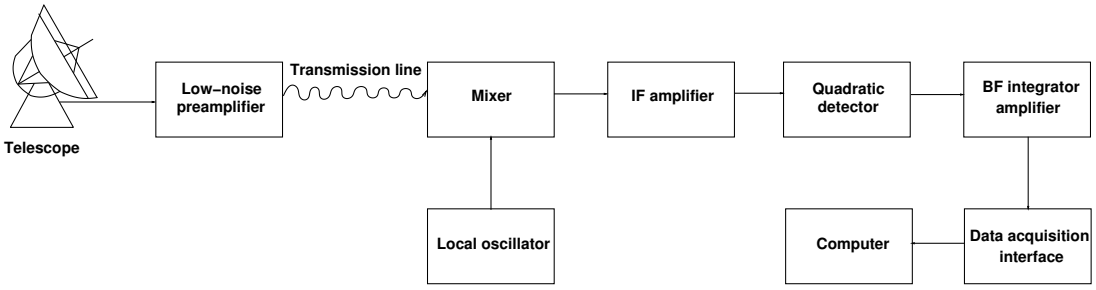

Figure 4.2: Schematic overview of the receiver setup of a radio telescope.

heterodyne total power radio telescope consists of several stages shown in Fig. 4.2. The antenna translates incident electromagnetic energy into a measurable electric current. Bigger dishes offer higher sensitivity because more electrons are focused onto the receiver. Every antenna has a structure dependent beam pattern, which represents the angular performance of the telescope, and has to be aligned with the target region.

The incident signal is fed into a preamplifier, where each antenna output is amplified by a factor 10^8 to 10^{10}. The challenging task of this device is to amplify the source amplitude, while retaining low noise levels, which are also intensified during this process. The resulting signal is then passed on to a mixer, which down mixes the frequency after their first amplification in order to achieve higher receiver stabilities. This is necessary, since electronic components involved in the data processing are much more effective at lower frequencies and also to provide the processed signal to retroactively produce a feedback on the incident radio waves. Together with a local oscillator (LO) this component produces two additional outputs. The LO adds a generated signal with a frequency close to the observing frequency. One result is the sum of the input frequency and the LO frequency, the other is their difference (e.g., Rohlfs (1986)). The

lower frequency is selected by a filter in the intermediate frequency (IF) amplifier. LOs should offer a stable output, in order not to drift into an interfering signals frequency or infringe upon the bandpass of the antenna or filters before the mixer. The IF amplifier amplifies the signal and usually offers bandpass filtering, which only allows a selected range of frequencies to pass through. The signal arriving at the quadratic detector oscillates in polarity around a central voltage. A semiconductor diode selects only one direction from this signal. The resulting output is the square of the input signal and is, thus, proportional to the power of the output provided by the receiver. The resulting direct current (DC) signal is still polluted by noise, which is usually much higher than the amplitude of the source. Therefore, the additional noise of the receiver needs to be lowered before the DC output is amplified. An offset circuit subtracts a steady DC voltage from the signal. The noise also adds rapid fluctuations to a steady voltage pattern, which need to be smoothed by an integrator in form of a capacitor. This component averages the signal over time, which greatly increases sensitivity. The remaining output is then amplified so that it matches the range of the recorder, where it is converted into digital signal and recorded.

The complete set of these instrumental sources of error deteriorate all astronomical data. The possible effect on the presented results of this thesis, as well as methods to reduce their impact and discriminate the intrinsic source signal from these errors are described in chapters 6 and 7.

4.2 Interferometry

According to Fizeau (1868), a mask with two pin-holes, covering a telescope's aperture, will produce an interferometric image, corresponding to the field of view of the original telescope. The beam combining mechanism of two separated telescopes is equal to such a masked telescope.

An interferometer is an array of at least two antennas that simultaneously observe the same target of interest. The signal of several telescopes is recorded together with a common time reference frame of an atomic clock. These signals are then correlated and the resulting interferometric pattern can be used to generate an image of improved resolution. The acquired resolution is equal to the performance of a single telescope with a diameter equal to the maximum baseline within the array and offers the light collecting capability defined by the apertures of the individual telescopes.

In order to regain the information about the source from observed fringes, it is crucial to align the data of each antenna as accurate as possible. Following Middelberg & Bach (2008), different signal path lengths to individual antennas make it necessary to correct for a time delay between these signals (see Fig. 4.3). This geometric time delay $\tau = \frac{\vec{B}\cdot\vec{s}}{c}$ has to be corrected by an additional time delay τ_0 which is inserted in the intermediate frequency (IF) line. Observed signals are received and amplified by each antenna before the digitized signal is send to a correlator that correlates and Fourier-transforms the output from each pair of antennas in the observing array.

According to Clark (1999), an interferometer can be described as a device that

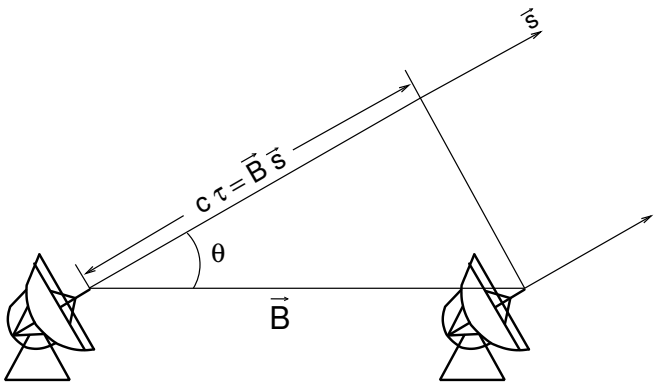

Figure 4.3: Schematic overview of the time delays between individual telescopes. $\vec{B}$ is the vector along the baseline of individual telescopes and $\vec{s}$ is the vector of unity in the direction of the observed source.

measures the spatial coherence function. If this visibility function is known at two points ($V_\nu(\vec{r_1}, \vec{r_2})$), it is possible to reconstruct the spatial intensity distribution of the observed source at the chosen frequency (I_ν). $V_\nu(\vec{r_1}, \vec{r_2})$ describes the similarity of the electromagnetic field at two locations. For celestial sources this similarity has a large spatial incoherence at astronomically relevant frequencies. Therefore, only very small angles offer coherent waves, which leads to the definition of the spatial coherence function ($V_\nu(\vec{r_1}, \vec{r_2})$):

$$V_\nu(\vec{r_1}, \vec{r_2}) = \langle E_\nu(\vec{r_1}) E_\nu^*(\vec{r_2}) \rangle \tag{4.1}$$

$$V_\nu(\vec{r_1}, \vec{r_2}) \approx \int I_\nu(\vec{s}) e^{-2\pi i \nu \vec{s}(\vec{r_1} - \vec{r_2})/c} d\Omega \tag{4.2}$$

$V_\nu(\vec{r_1}, \vec{r_2})$: Spatial coherence function for the locations $\vec{r_1}$ and $\vec{r_2}$.
$E_\nu(\vec{r})$: Sum of all monochromatic waves emitted by sources at a frequency ν.
$E_\nu^*(\vec{r})$: Complex conjugate of $E_\nu(\vec{r})$.
I_ν: Spatial intensity distribution of the observed source at a frequency ν.
$\vec{r_i}$: Observer location.
$\vec{s}$: Unit vector towards source.
$d\Omega$: Surface element of the celestial sphere.

The visibility function is, therefore, a function of the separation and relative orientation of two locations, which only depends on the coordinates of the antennas projected onto the plane perpendicular towards the line of sight. These equations are the Fourier transform between the spatial coherence function ($V_\nu(\vec{r_1}, \vec{r_2})$) and the intensity distribution in the sky (I_ν). The plane orthogonal to the line of sight is called the (u, v)-plane (see Fig. 4.4). The defined axes u and v of this plane describe the projected separation and orientation of the interferometer elements, measured in units of wavelengths. The effective baseline of the interferometer antennas is the projected baseline onto this plane.

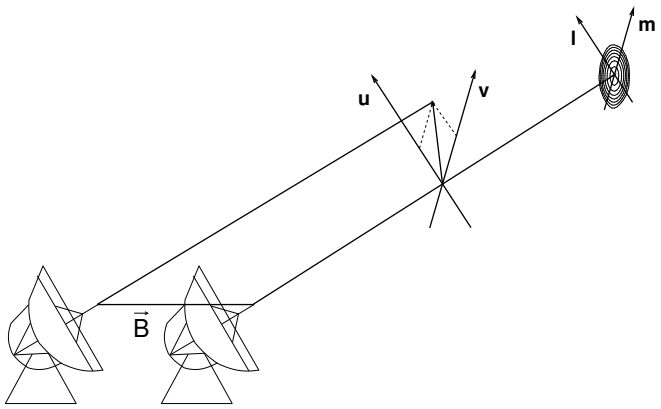

Figure 4.4: Illustration of (u, v)-plane and (l, m)-coordinates. Schematic overview, according to Middelberg & Bach (2008).

A complex source structure will have different visibility functions for every point in the (u, v)-plane which makes it necessary to measure as many points as possible. A stationary array produces a point in the (u, v)-plane for each set of two antennas in the array. Because of the Earth's rotation with respect to the source, the position and orientation of the baseline is continuously changing which results in elliptical (u, v)-tracks. These tracks are not necessarily centered at zero, which would only be the case for an east-west interferometer.

The upper left frame of Fig. 4.5 shows a non-continuous track of a single baseline. Within 24 hours this track will form an ellipse, if the changes in the relative orientation of Earth and science target within a single day are disregarded. In the special case of sources in the celestial pole these tracks will be circles. Since the second half of the observed ellipse is equal to its complex conjugate, it is common to additionally plot the point reflection of this track. Therefore, 12 hours of observation form a closed elliptical track in the (u, v)-plane. Longer baselines correspond to ellipses with bigger semi-major axis in this plot. The upper right frame of Fig. 4.5 shows the corresponding (u, v)-track for an array of antennas. Each pair forms a track at a radius corresponding to their baseline and their opening angle is related to the observation time of the antenna pair. Observing a band of distinct frequencies will result in broader (u, v)-tracks (see Fig. 4.5 bottom two panels). This method of using the Earth rotation to gain an improved (u, v)-coverage is commonly referred to as aperture synthesis.

In the (u, v)-plane the spatial coherence function translates into:

$$V_\nu(u, v) = \int\int I_\nu(l, m) e^{-2\pi i(ul+vm)} dl dm. \tag{4.3}$$

With the coordinates l and m being the direction cosines pointing at the source. The sensitivity of an interferometer element as a function of the angle on the sky can be accounted for by introducing a factor A_ν to these equations.

This results in a spatial coherence function of:

$$V_\nu(u, v) = \int\int A_\nu(l, m) I_\nu(l, m) e^{-2\pi i(ul+vm)} dl dm. \tag{4.4}$$

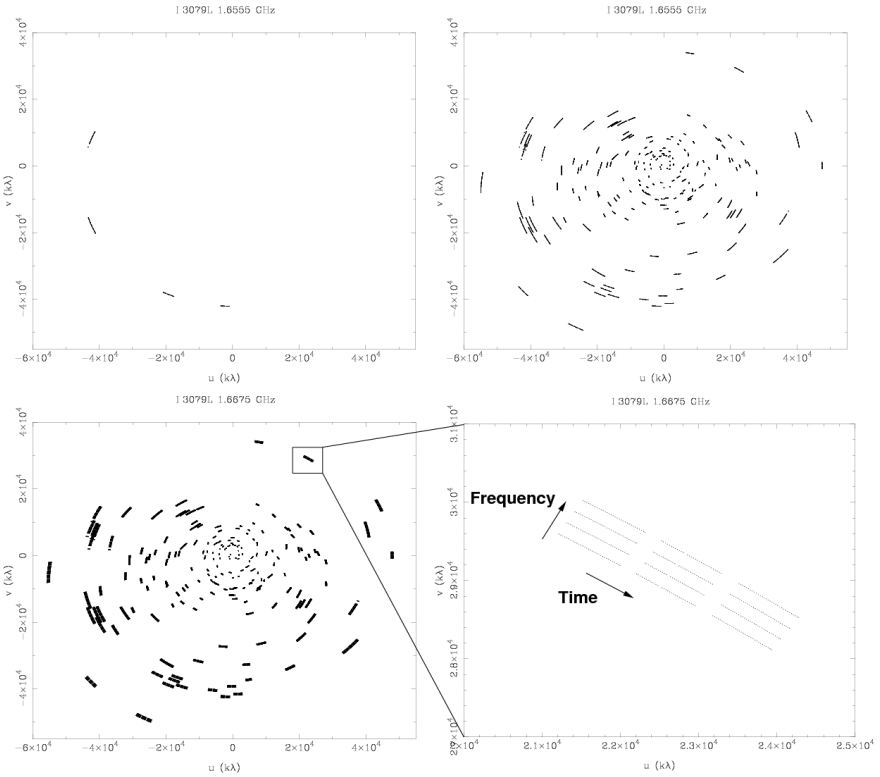

Figure 4.5: Overview of an exemplary (u, v)-track. Top left: (u, v)-track of a single baseline. Top right: (u, v)-track of a telescope array forming several baselines. Bottom left: (u, v)-track of a telescope array forming several baselines observing at multiple frequencies. Bottom right: Detailed view of a multi-frequency (u, v)-track segment. Source: (Middelberg & Bach, 2008)

4.3 Very Long Baseline Interferometry

VLBI is a technique that achieves high-resolution radio images using baselines ranging from hundreds to several thousands of kilometers. Even though linked interferometry and VLBI are very similar, there are some practical differences, for instance separated clocks, allowing for rapid changes in instrumental phases. According to Walker (2002), another distinction is that due to the large dimensions of such arrays, individual antennas are observing through separate areas of the atmosphere and, thus, have to be considered as independent. Together with the circumstance that individual antennas might observe the science target at different elevations, this causes rapid phase variations and large gradients, which imply a differential delay between the two elements of an interferometer. The model uncertainties can be large compared to linked interferometers, because the required accuracy to determine source positions, station locations, and Earth orientation parameters to a fraction of the observing wavelength is challenging. The final, fine determination of these parameters is performed at the so called "fringe search" process.

4.3.1 VLBI arrays

An array of N telescopes offers baselines, which sample the visibility function at $N(N-1)/2$ instantaneous positions in the Fourier (u, v)-plane at a given time, each one corresponding to a projected baseline vector in the plane of the sky. The information of all baselines is not combined until the imaging stage and is conceptionally and practically comparable to a two-element interferometer. All telescopes need to be observing the same source at once, which is not always possible if the interferometer elements are spread over a large surface area. Following Middelberg & Bach (2008), electromagnetic waves arriving at the telescopes have to pass different atmospheric conditions before arriving at the telescopes, which results in different observed flux values. This requires a fine tuning of the LO (see Sect. 4.1). It is crucial that the LO is stable and operates at a well-known frequency to ensure that all telescopes are observing at the same frequency. The data are then digitized and stored for further analysis.

A correlator aligns the streams of all sets of baselines together with adding time delays and phases. The data of each pair of antennas is then cross-multiplied and Fourier transformed from the temporal into the spectral domain. While Equation 4.4 is only true at a single monochromatic frequency and the VLBI observing bands require frequency averaging. This introduces an additional source of error, by the deviations of the true frequencies from their mean value. This error is reduced by splitting the bands into several frequency channels.

4.3.2 VLBI Surveys and observable parameters

AGN observations at wavelengths ranging from 7 mm to 21 cm are regularly performed with VLBI. While there are currently many surveys at these frequencies, few data were available at the beginning of the VLBI age. The commissioning of the VLBA (see Fig. 5.1) in the early 1990s significantly improved this number of performed VLBI

Program	λ	N_{sources}	N_{epochs}[a]	**Time**	**Ref.**
GMVA 3mm	3 mm	121	2	2004-	Lee et al. (2008)
Boston Univ.	7 mm	35	50	2007-	Marscher et al. (2011)
TeV Sample	7 mm[b]	7	5	2006-	Piner et al. (2010)
MOJAVE/2 cm Survey	2 cm	300	20	1994-	Lister et al. (2009)
Bologna low-z	2/3.6 cm	42	2	2010-	Giroletti et al. (2010)
TANAMI	1.3/3.6 cm	80	5	2008-	Ojha et al. (2010)
VIPS	6 cm	1127	1	2007	Hemboldt et al. (2007)
VIPS subsample	6 cm	100	2	2010-	Taylor (2010)
CJF	6 cm	293	3	1990s	Pollack et al. (2003)
ICRF	3.6/13 cm	500	10	1990s	Ojha et al. (2004)
VCS	3.6/13 cm	3400	1	1990s	Kovalev et al. (2007)

[a] Typical number of epochs per source

[b] Also including λ1.3 cm & λ3.6 cm

Table 4.1: Summary of VLBI surveys. Source: (Ros, 2012)

observations. There are several other consolidations of radio telescopes that regularly observe and provide long time surveys of AGN, like the European VLBI Network (EVN) or the Long Baseline Array (see e.g., Ros (2012)). These surveys gathered data for hundreds of sources, which can be used as calibrators and determining geophysical (e.g., tectonic motion, Earth orientation parameters), as well as astronomical parameters.

Currently available and ongoing surveys are the VLBA Imaging and Polarimetry Survey (VIPS), which is a polarimetric single epoch 5 GHz survey (mid 2000s), the Boston University Blazar Program, monthly 43 GHz observations since 2007, the Monitoring of Jets in Active Galactic Nuclei with VLBA Experiments (MOJAVE), observing 135 objects at 15 GHz in dual polarization mode above $-30°$ ($\sim$300 sources in catalog) and the Tracking Active Galactic Nuclei with Austral Milliarcsecond Interferometry (TANAMI) project, covering many sources below $-30°$ since 2007 at 8.4 GHz and 22 GHz. A summary of all mentioned VLBI surveys is shown in Tab. 4.1 and a more detailed description of the results of every survey can be found in (Ros, 2012).

The current resolution and sensitivity of VLBI arrays enables measuring several parameters of single or combined (in frequency or time) VLBI images. The observable parameters are summarized in Tab. 4.2. These parameters can be directly measured (apparent speed (β_{app}), flux density (S), brightness temperature (T_b), misalignment angle of pc- and kpc-scale jets ($\Delta\phi$), jet-counterjet ratio, apparent (ψ) and intrinsic (ψ_{int}) opening angle, polarization level (m), polarization angle (χ), Faraday rotation measurement (RM)) or indirectly derived from these parameters (variability Doppler factor (δ_{var}), Lorentz factor (Γ), viewing angle (θ) and the ejection time of components (t_0)).

While these surveys provide access to informations about many celestial sources, they are a very useful to acquire calibrator sources. Such sources are required to be close to the science target and crucially affect the results that can be gained from various observations. In this context, these surveys are a reliable source for phase referenc-

Radio		
Parameter		Units
Radio detection		
Apparent speed	β_{app}	c
Flux density	S	Jy
Brightness temperature	T_{b}	K
Apparent opening angle	ψ	deg
Luminosity	L_{R}	$\mathrm{W\,Hz^{-1}}$
Jet-to-counterj. ratio	R	–
P.A. misalignment[a]	$\Delta\phi$	deg
Spectral index	α	–
Polarisation angle	χ	deg
Polarisation level	m	%
Faraday rotation	RM	$\mathrm{rad\,m^{-2}}$
Viewing angle	θ	deg
Lorentz factor	Γ	–
Doppler factor	δ	–
Ejection epoch	t_0	yr

[a] Kiloparsec- and parsec-scale misalignment

Table 4.2: Observable parameters by VLBI. Source: (Ros, 2012)

ing calibrators, that can significantly improve the accuracy of position measurements presented in this thesis, as they are described in section 7.3.

4.3.3 VLBI imaging

As described in Middelberg & Bach (2008), the (u, v)-track of every observation resembles an imperfect coverage of the total observable Fourier space (see Sect. 4.2). Therefore, the quality of the Fourier reconstruction of this image, in terms of reconstructing its original structure, is defined by the completeness of its (u, v)-coverage. During the imaging process, the true brightness distribution of the source is convolved with the point-spread-function (PSF) of the observing instrument. This defines the PSF as the Fourier transform of the (u, v)-coverage ($B(l, m) = F[S(u, v)]$), with $S(u, v)$ being unity at the positions of data points and zero elsewhere. The transformed image will have more artifacts in form of sidelobes, the fewer data points its (u, v)-track offers. In order to achieve a better approximation of the real source's brightness distribution, it is necessary to fill the gaps in the (u, v)-plane by interpolating the visibilities with the standard CLEAN algorithm, which is included the DIFMAP software (Shepherd et al., 1994).

4.3.3.1 Cleaning the image

Middelberg & Bach (2008) describe how CLEAN, introduced by Högbom (1974), iteratively lowers the image artifacts of interferometric data caused by imperfect (u, v)-coverage. This algorithm iterates the dirty image by the following logic:

1. Find the brightest pixel of the dirty image ($I^{'}(l_i, m_i)$).
2. Shift the central pixel of the dirty beam $B(l, m) = F(S(u, v))$ to the position of $I^{'}(l_i, m_i)$. Introduce a scaling factor c so that $I^{'}(l_i, m_i) = cB(l_i + \Delta l, m_i + \Delta m)$.
3. Subtract the dirty beam, multiplied by a loop gain value $\gamma << 1$, from the dirty image. Keep the residual: $R(l, m) = I^{'}(l_i, m_i) - c\gamma B(l_i + \Delta l, m_i + \Delta m)$.
4. Add a delta component $(l_i, m_i, \gamma I^{'}(l_i, m_i))$ to the clean image.
5. Restart the loop.

With every iteration a delta component model of the true source is compiled and gets more accurate with every completed loop. These steps are iterated until the sidelobes of the residual image are much lower than the image noise. Then the final clean image can be compiled by convolving it with the clean beam and adding the residual image. The clean beam is approximated by fitting two-dimensional Gaussians to the center of the dirty beam image.

This approach offers the possibility to analyze different aspects of the source by weighting down different baseline regimes during the imaging process. Short baselines can be used to emphasize sensitivity to extended structure, while considering only long baselines offers higher resolution to image fine structures. All maps of this thesis presented in chapter 7 have been produced according to this image cleaning method. The approach of defining delta components in the dirty image can cause pixels of high noise values to be detected as faulty components, which then leads to a wrong model, that is used to display the clean image. This makes it necessary to carefully test the derived model by the methods described in section 7.2.

Chapter 5

Observations

This thesis is based on VLT-NIR-triggered 7 mm radio data carried out on May 16 to 18 2012 by the VLBA, which offer ten 25 m telescopes mainly located across the northern hemisphere (see Fig. 5.1). The 43 GHz observations started less than one hour after the detected NIR flare was reported to the observing team of the NRAO staff. The following sections discuss the observational results in detail. While the 43 GHz data are the main subject of this thesis and have been published in Rauch et al. (2016), all NIR observations have been performed by and published in Shahzamanian et al. (2015). The NIR data is only used as a reference to analyze the time delay between flares of Sgr A* at these two wavelength regimes.

5.1 VLBA data

On May 16-18 2012 the VLBA observed three six-hour (u, v)-tracks at 7 mm. The corresponding data (project code: BE061) of this thesis are presented in Rauch et al. (2016). A total of nine VLBA stations participated in this measurement campaign. These were Fort Davis (FD), Hancock (HN), Kitt Peak (KP), Los Alamos (LA), Mauna Kea (MK), Owens Valley (OV), Pie Town (PT), Brewster (BR), and North Liberty (NL). The provided maximum baseline of this array amounts to about 8000 km, that is ∼1140 wavelengths, which provide a resolution of (8.7×10^{-4}) rad.

Each station recorded in dual circular polarization mode at an aggregate bit rate of 2 Gbps (8 sub-bands or IF channels at 32 MSamples/sec of 2 bit) using the VLBA/MkIV correlator. This results in an expected theoretical thermal noise level of 0.27 mJy/beam at 43 GHz, assuming a degradation factor of 1.5 due to atmospheric absorption of the theoretical value of 0.18 mJy/beam and detections in the complete array. The VLBA correlator in Socorro, New Mexico (USA) correlated the data with an integration time of 1 s at 512 spectral bands per baseband channel.

The extragalactic sources 3C 345, NRAO 530, and 3C 279 served as fringe tracers and amplitude calibrators during the observations. The former two of these have been observed every hour for 2 min, while the latter was only irregularly targeted at the beginning of each observation for 2 min (once on May 16 and 17; thrice on May 18). In-between these calibrator slots, the science target Sgr A* was observed in a duty cycle of 60 s between each pointing at two compact extragalactic sources (J1745−283, J1748−291), which were used as phase referencing calibrators. The duty cycle over a duration of 60 s, results in a scan length of 6 s per source, including some slewing time between switches and has been performed in the following order:

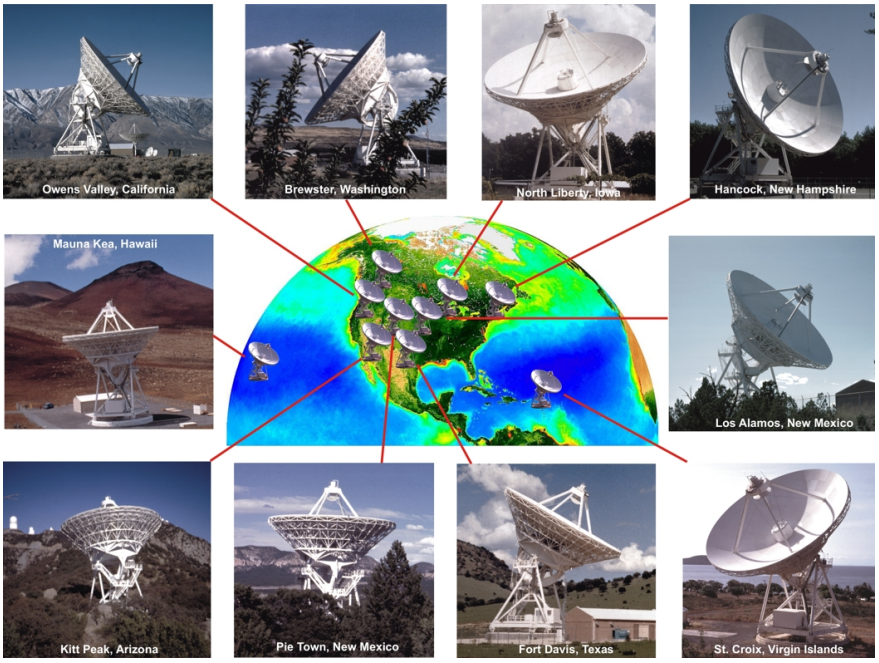

Figure 5.1: Telescope sites of the VLBA. All antennas offer a diameter of 25 m and form an array with a maximum baseline of about 8000 km. Source: NRAO.

$$\text{J1745}-283 \rightarrow \text{Sgr A*} \rightarrow \text{J1748}-291 \rightarrow \text{Sgr A*} \rightarrow \text{J1745}-283$$

Rapidly switching between Sgr A* and the phase referencing sources causes Sgr A* to be targeted for $\frac{12}{60} = 0.2\,\text{min}^{-1}$, which results in an effective on source time of 72 min for a 6 hour (u, v)-track.

5.2 NIR data

The presented 7 mm VLBA observations were triggered on preceding NIR observations, that are discussed in Shahzamanian et al. (2015) in more detail. The K_s-band ($2.2\,\mu m$) data, plotted in Fig. 7.1, were performed on May 17 2012 between 4:49 and 9:53 UT at the VLT (UT4) using the adaptive optics (AO) capabilities of the NACO instrument (Nasmyth Adaptive Optics (NAOS), Coudée Near Infrared Camera (CONICA)). The included Wollaston prism together with a rotatable half wave plate was used to measure dual polarization images at a resolution of 13 mas per pixel. The NIR source IRS 7 ($K_s \sim 6.5 - 7.0\,\text{mag}$), separated by $\sim 5.5''$, was used to close the AO loop. The AO corrections were stable and provided acceptable performance for the whole dataset. The data were calibrated by Shahzamanian et al. (2015), using several close-by calibrators and the common reduction strategies described in Witzel et al. (2012). Sky and flat field subtraction, as well as bad pixel correction ensures a stable image background. In order to remove fluxes of very close sources, a Lucy-Richardson deconvolution (Richardson, 1972; Lucy, 1974) has been performed, using a PSF that has been determined from

several point like stars in the vicinity of Sgr A*. Flux densities have been corrected for residual background flux, determined from defined apertures at areas free of resolved source fluxes. The total error in flux amounts to ~ 0.25 mJy, mostly caused by imperfect AO performance.

5.3 Observational constrains

There are several sources of error that can affect interferometric observations. Compared to single-dish experiments, interferometric arrays are influenced by similar effects, but the individual elements can be remotely located from each other, which causes local conditions to be significantly different at individual telescope sites. The strongest effect on the data arises from the Earth's atmosphere, mainly in the ionosphere and troposphere. Figure 5.2 shows the current model of Earth's atmospheric layers.

While, according to Middelberg & Bach (2008), tropospheric and other errors follow a linear dependence on frequency and can be more easily predicted, the effects of the ionosphere are inversely proportional to the square of the frequency. Therefore, the effect of the ionosphere is more dramatic at lower frequencies. Radiation of the Sun ionizes this utmost layer of the atmosphere, which, therefore, changes on seasonal and diurnal time scales and depends on the solar activity. The plasma frequency of its particles is close enough to the observing bands at low GHz frequencies to have a significant impact.

Turbulences, inhomogeneities in its composition and the density of the medium (e.g., caused by wind) that electromagnetic waves have to pass through cause different travel paths towards the observing telescope. This results in the arriving signal to have different Phases at different telescopes. Therefore, visibilities are scattered away from their real value and will reduce the signal to noise ratio (SNR). In order to overcome these phase errors, atmospheric models are applied at the correlator stage which accounts for most of the long time variations. But the atmosphere also causes phase variations on very short time scales that still affect the corrected visibilities and result in residual phase errors.

Due to their dipole momentum, the total electron content (TEC) of the ionosphere is the most important value that influences the travel path of electromagnetic waves and needs to be monitored continuously due to its short timescale. As described in Sect. 5.3.2, these effects have a smaller impact at short wavelengths, like 7 mm, while tropospheric effects (see Sect. 5.3.3) have a stronger impact at these frequencies. Besides these effects, the most significant errors arise mainly from uncertainties in the telescope array. Since the performance of an interferometer crucially depends on the phase alignment of its elements, the position of each telescope has to be known to a fraction of the observing wavelength.

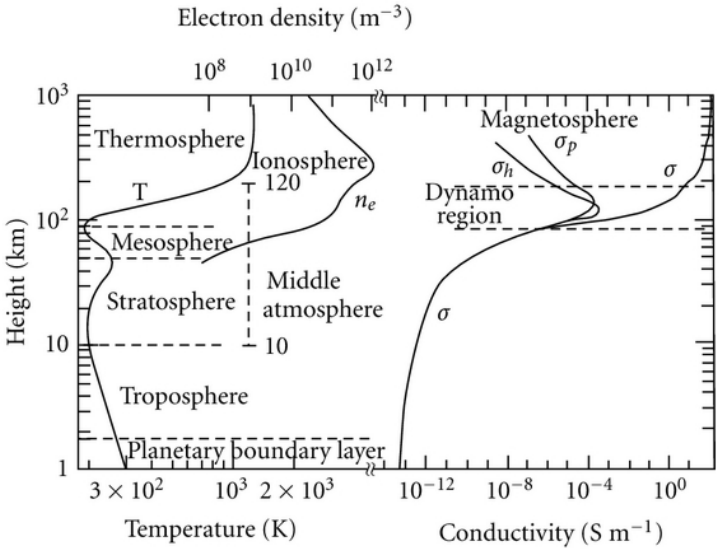

Figure 5.2: Earth's atmospheric layers. The most significant effects on astronomical observations arise from the amount of electrons in the ionosphere (n_e) and the quantity of water vapor contained in the troposphere. Source: Singh et al. (2004)

There are several fundamental reference frames that are used to address these effects:

1. International Celestial Reference Frame (ICRF).
2. International Terrestrial Reference Frame (ITRF).
3. Earth rotation and orientation relative to an inertial reference frame of a spatially constant source (e.g., quasars).

These frequency, baseline length and time of the year dependent errors and other irregular effects need to be corrected to gain a reliable image of the observed source.

5.3.1 Scatter broadening

The radio images of Sgr A* are broadened by interstellar scattering on an ionized medium (van Langevelde, 1992). Density fluctuations cause the power spectrum to be $\propto k^{-\beta}$, with k being the wavenumber of these fluctuations (Romani et al., 1986; Lo et al., 1998). The scattering angle θ_{sca} scales as $\lambda^{1+\frac{2}{(\beta-2)}}$ (Lo et al., 1998). The exponent of this power law is still under investigation and is crucial for intrinsic measurements of source sizes. The power law exponent is currently assumed to be about two (e.g., Romani et al. 1986; Narayan & Goodman 1989; Backer et al. 1993; Rogers et al. 1994; Krichbaum et al. 1998; Lo et al. 1998; Doeleman et al. 2001; Bower et al. 2006; Krichbaum et al. 2006; Lu et al. 2011a and references therein).

The intrinsic source size should follow an exponent between λ and λ^2 since the resolution of the observing telescope is proportional to $\frac{\lambda}{D}$, with D being the instruments diameter or baseline (Bower et al., 2004). In good agreement with this, Lu et al. (2011a) detect sizes at 22, 43 and 86 GHz which follow $\lambda^{1.4...1.5}$, while Bower et al. (2006) report $\lambda^{1.3...1.7}$ at wavelengths ranging from 0.35 to 6 cm.

The intrinsic source size can be estimated from the observed angular size and the scattering size following:

$$\theta_{int} = \sqrt{\theta_{obs}^2 - \theta_{sca}^2} = \sqrt{\theta_{obs}^2 - (a\lambda^\beta)^2}. \tag{5.1}$$

A power law index with an β is assumed and a can be measured. This law breaks at 43 GHz (7 mm) and, thus, observations at shorter wavelengths offer the possibility to detect the intrinsic unscattered source size. Krichbaum et al. (2006) report sizes of $223\pm63\,\mu$as (7 mm), $134\pm27\,\mu$as (3.4 mm), $\leq 581\,\mu$as (2 mm) and $98\pm54\,\mu$as (1.4 mm).

There are no measurements for the presented data set, that allow to gain the intrinsic source size of Sgr A*, but in section 8.1, we discuss observed time delays as a function of its theoretical intrinsic source size derived from a power law given by Falcke et al. (2009).

5.3.2 Ionospheric effects

The ionosphere represents the outer layer of Earth's atmosphere, located between the thermosphere and exosphere at an altitude of about 80-1000 km. It consists of particles, that have been partially ionized by absorbing high energy ultraviolet radiation. While electromagnetic waves reach the Earth's atmosphere with only minor deviations from their original properties, they are strongly affected on the last few hundred kilometers. According to Moellenbrock (2002), the ionosphere is birefringent, and the circular polarization of one side is delayed with respect to the other, which introduces a phase shift of:

$$\Delta\phi = 0.15\lambda^2 \int B_{||} n_e ds. \tag{5.2}$$

$[\Delta\phi]$= deg
$[\lambda]$= cm
$[n_e ds]$=10^{14} cm^{-2}
$[B_{||}]$=G.

This phase shift causes the linear polarization position angle to rotate and is called Faraday rotation. Its λ^2-dependence causes this effect to be most important at long wavelengths and during phases of high ionospheric activity, which are at their maximum at sunrise/-set or during periods of high solar activity. The defining quantity of this effect is the TEC ($\int n_e ds$).

The ionospheric delay can be corrected by dual band observations or by GPS ionosphere models. Therefore, it is very important to gain an accurate map of the amount

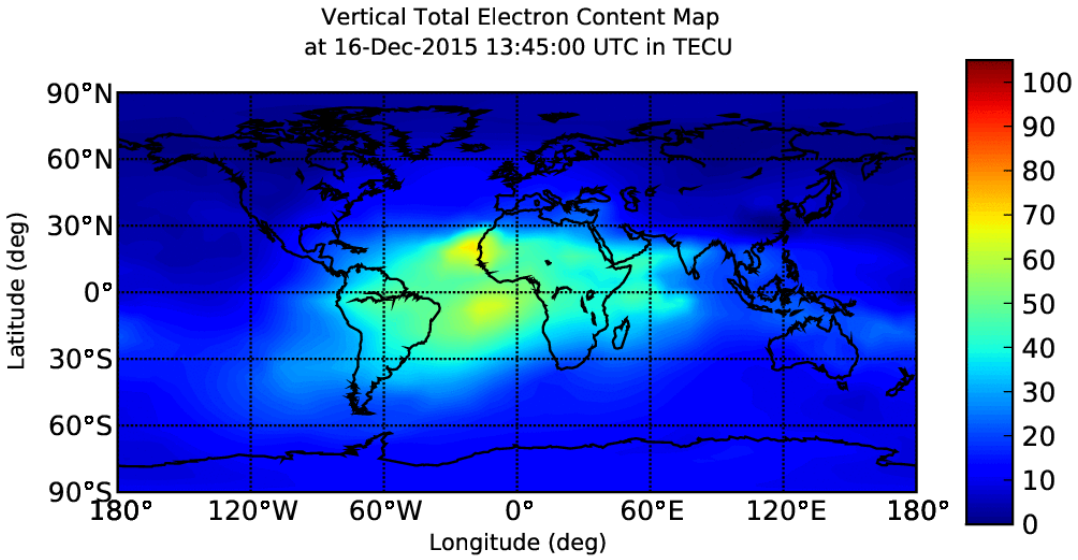

Figure 5.3: Global map of the total electron content in the ionosphere taken on 16 Dec 2015. The color scale on the right represent total electron content units in $10^{16}\mathrm{m}^{-2}$. Source: NASA Jet Propulsion Laboratory.

of electrons in the ionosphere. Such a map is presented in Fig. 5.3. Following Moellenbrock (2002), the effects of on the signal can be expressed by the following matrix:

$$\bar{F}^{RL} = \begin{pmatrix} e^{i\Delta\phi} & 0 \\ 0 & e^{-i\Delta\phi} \end{pmatrix}. \tag{5.3}$$

5.3.3 Tropospheric effects

The troposphere is the lowest atmospheric layer up to 10 km in which all weather effects take place. It contains 99% of the vaporized water amount in the atmosphere, which can change significantly during observations. According to Moellenbrock (2002), the effect of these molecules is strongest at high frequencies above their absorbing/emitting frequency ($\nu > 15\,\mathrm{GHz}$) and during phases of high amounts of water in the atmosphere (e.g., during sunrise or wet seasons). The tropospheric influence depends, like the ionospheric effects, on the amount of atmosphere that electromagnetic radiation has to pass through and is, therefore, elevation dependent.

In contrary to the ionosphere, this atmospheric layer is not affecting the polarization, but it has a certain opacity which can change the measured amplitudes. In addition, the troposphere is refractive and introduces another phase effect in the order of 2 m (7 ns) compared to their vacuum phases at zenith. Therefore, astronomical data needs to be corrected for the mentioned opacity effects. The electronic gain of an telescope array changes for example with the amount of atmosphere the electromagnetic waves have to pass through (see Fig. 5.4). Following the notation in Moellenbrock

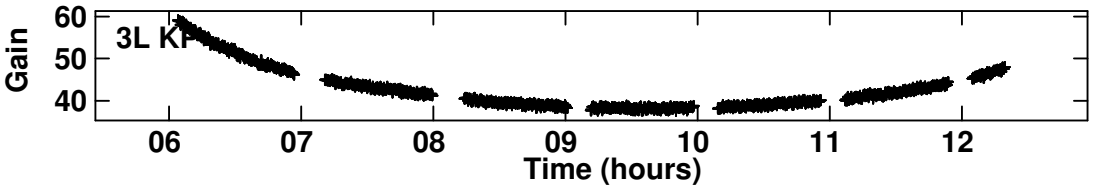

Figure 5.4: VLBA antenna (KP) gain as a function of time observed on May 17 2012. This plot shows the effect of changing elevations on the amplitudes of Sgr A*.

(2002), this effect is mathematically described by:

$$T^{\bar{p}q} = \begin{pmatrix} t & 0 \\ 0 & t \end{pmatrix} = t \begin{pmatrix} 1 & 0 \\ 0 & 1 \end{pmatrix}. \tag{5.4}$$

5.3.4 Parallactic angle

The orientation of the receiver with respect to the field of view can change during observations because of the Earth's rotation and introduces a time depended parallactic angle which is present in the phases. According to Moellenbrock (2002), this value is, therefore, only constant for equatorial telescopes and varies with:

$$\chi(t) = \arctan \frac{\cos(l)\sin(h(t))}{\sin(l)\cos(\delta) - \cos(l)\sin(\delta)\cos(h(t))}. \tag{5.5}$$

This introduces a rotation of the linear polarization position angle. In the context of the mathematical framework provided by Moellenbrock (2002), the parallactic angle affects the signal as described by:

$$P^{\bar{R}L} = \begin{pmatrix} e^{i\chi} & 0 \\ 0 & e^{-i\chi} \end{pmatrix}. \tag{5.6}$$

5.3.5 Antenna Voltage Pattern

According to Moellenbrock (2002), all antennas have direction dependent gain values. The effects caused by this are important if the observed region in the plane of the sky is $\geq \frac{\lambda}{D}$ or for long observations during which the source elevation changes significantly. This is the case for the presented measurement campaign of this thesis and gains importance towards lower frequencies, because the radio surface density is greater at these frequencies. The effects manifest as a matrix in the form of:

$$E^{\bar{p}q} = \begin{pmatrix} e^{p}(l,m) & 0 \\ 0 & e^{q}(l,m) \end{pmatrix}. \tag{5.7}$$

5.3.6 Polarization leakage

Orthogonal polarizations are not completely isolated and can be affected by a frequency dependent leakage. This leakage has to be corrected for polarization observations, since it imposes crucial effects on linear polarization imaging data, which are affected as $\sim dI$. The effect on the total intensity of dual circular polarization systems is less important (only for high dynamic range imaging) and is affected as $\sim dQ, dU$.

The polarization of high performance feeds is in the order of a few percent (Moellenbrock, 2002) and can be described as:

$$D^{\bar{p}q} = \begin{pmatrix} 1 & d^p \\ d^q & 1 \end{pmatrix}. \tag{5.8}$$

5.3.7 Radio frequency interference

Another observing constraint is radio emission of human origin. The variety of these effects are consolidated under the term of radio frequency interference (RFI), which has a strong effect on the data quality. RFI increases the total noise and complicates amplitude calibration, because it correlates with the signal of real observed source structure. Such interference can also correlate between antennas close to each other, if they are in the range of the same source of RFI, and obscures natural emission in spectral line observations. These effects can only be mitigated but not completely removed from the data by electronic designs of the antennas and choosing interference-free frequencies. It is also possible to observe continuum channels in spectral-line mode in order to edit bad channels.

5.3.8 Electronic gain

The electronic gain represents the scaling factor to translate the electronic response of a telescope into astronomical units and is usually not constant during observations. Following Ros & Kadler (2009), the electronic gain of a telescope is elevation dependent, because different orientations of the antenna cause gravitationally induced distortions (see Fig. 5.4) and is also affected by many of the amplitude and phase altering effects introduced by electronic components, such as amplifiers, mixers, quantizers and digitizers. These effects have the strongest impact on the data and are frequency independent. The observed signal of the electronics (S_{ij}) can be described by:

$$S_{ij} = A_{ij} b \sqrt{\frac{T_{s_i} T_{s_j}}{K_i K_j}}. \tag{5.9}$$

A_{ij}:measured visibility amplitude (raw correlation coefficient)
b: digitization loss
K_i: antenna sensitivities in $\frac{K}{Jy}$
T_{s_i}: System temperature in K.

The system temperature is usually expressed in terms of the system equivalent flux density (SEFD):

$$SEFD_i = \frac{T_{s_i}}{K_i}. \tag{5.10}$$

The sensitivity of an interferometer is then described by:

$$\Delta S_{ij} = \frac{1}{\eta_s}\sqrt{\frac{SEFD_i \cdot SEFD_j}{2\Delta\nu\tau_{acc}}}. \tag{5.11}$$

η_s: Electronic losses
$\Delta\nu$: Observing bandwidth
τ_{acc}: Accumulation time

The corresponding matrix, according to Moellenbrock (2002), is described by:

$$\bar{G^{pq}} = \begin{pmatrix} g^p & 0 \\ 0 & g^q \end{pmatrix} \tag{5.12}$$

5.3.9 Bandpass Response

The bandpass response represents the response of all antenna electronics dealing with the frequency of the observing signal. It describes the frequency dependence of the electronic devices and accounts for effects caused by non-square filters, as well as optical-/electronic reflections, that introduce noise across the bands. The non-square filters, used to select pass-bands, causes the amplitudes to be lower than the original signal at both ends of these bands (see Fig. 6.1). According to Moellenbrock (2002), this can be expressed by:

$$\bar{B^{pq}} = \begin{pmatrix} b^p(\nu) & 0 \\ 0 & b^q(\nu) \end{pmatrix}. \tag{5.13}$$

5.3.10 Summary of effects

All these previously mentioned effects can, according to Moellenbrock (2002), be condensed into a total measurement equation:

$$\begin{aligned} \vec{V_{ij}} &= \bar{M_{ij}} \int \bar{B_{ij}}\bar{G_{ij}}\bar{D_{ij}}\bar{E_{ij}}\bar{P_{ij}}\bar{T_{ij}}\bar{F_{ij}}\vec{SI_\nu}(l,m)e^{-i2\pi(u_{ij}l+v_{ij}m)}dldm + \vec{A_{ij}} \\ &= \bar{M_{ij}} \int \bar{J_{ij}}\vec{SI_\nu}(l,m)e^{-i2\pi(u_{ij}l+v_{ij}m)}dldm + \vec{A_{ij}} \end{aligned} \tag{5.14}$$

with

$$\bar{J_{ij}} = \bar{B_{ij}}\bar{G_{ij}}\bar{D_{ij}}\bar{E_{ij}}\bar{P_{ij}}\bar{T_{ij}}\bar{F_{ij}}. \tag{5.15}$$

S: Charts the stokes vector I to the polarization basis of the instrument.

$\bar{M_{ij}}$: Multiplicative baseline errors.

$\vec{A_{ij}}$: Additive baseline errors.

The errors described by $\bar{J_{ij}}$ are usually orientation depended, but it is often more practical to ignore the dependence of the calibration components. This makes the measurement equation a relation between observed ($\vec{V}_{ij}^{\text{obs}}$) and ideal visibilities ($\vec{V}_{ij}^{\text{ideal}}$):

$$\vec{V}_{ij}^{\text{obs}} = \bar{J_{ij}}\vec{V}_{ij}^{\text{ideal}} = \bar{B_{ij}}\bar{G_{ij}}\bar{D_{ij}}\bar{P_{ij}}\bar{T_{ij}}\bar{F_{ij}}\vec{V}_{ij}^{\text{ideal}}. \tag{5.16}$$

In case of a calibrator of known structure (ideal visibility), this equation can be solved for individual components:

$$(\vec{V}_{ij}^{\text{corrected·obs}}) = \bar{J}_{ij}^{\text{solvable}}(\vec{V}_{ij}^{\text{corrupted·ideal}}). \tag{5.17}$$

Simple matrix operations can then be used to regain information of individual components.

For example:

$$(\bar{G}_{ij}^{-1}\bar{B}_{ij}^{-1}\vec{V}_{ij}^{obs}) = \bar{D_{ij}}(\bar{P_{ij}}\bar{T_{ij}}\bar{F_{ij}}\vec{V}_{ij}^{\text{ideal}}). \tag{5.18}$$

5.3.11 Isoplanatic patch

Properties of the atmosphere change as a function of altitude and area in the plane of the sky. As described in Bertram (2007), the, so called, effect of anisoplanatism is caused by different atmospheric perturbations, which wavefronts encounter on their way to the observer, if they originating from two different points in the sky. Signals arriving from two distinct directions are considered to be statistically correlated, as long as they are within an isoplanatic patch defined by an isoplanatic angle (θ_0) (Fried, 1982). This angle is defined by the separation under which the phase decorrelation is less than $1\,\text{rad}^2$:

$$\theta_0 = 0.0581 \cdot \lambda^{\frac{6}{5}} \Big[\int dz C_n^2(z) \cdot z^{\frac{5}{3}} \Big]^{-\frac{3}{5}} \propto \lambda^{\frac{6}{5}}. \tag{5.19}$$

$C_n^2(z)$: Refractive index structure constant.

$z = h\cos\gamma$

The λ-dependency of this equation results in less Fried cells to be present across a considered area at lower frequencies. Therefore, long wavelength observations are

less sensitive to the atmospheric turbulences. A typical value for isoplanatic patches at infrared wavelengths are $\theta_0 = 20''$. This angle forms a boundary condition for a reliable performance of data calibration with respect to well known calibrator sources, as described in chapter 6, and also crucially affects the performance of the phase referencing results presented in this thesis (see Sect. 7.3).

5.3.12 Calibrator choice

Even though, VLBI observations usually offer fringe amplitude accuracies around 5% at 1-10 GHz, it is required to observe calibrators in order to accurately calibrate the source amplitudes. Calibrators should offer well known, preferably constant fluxes and source structures. Therefore, the best candidates are close-by spatially constant point sources, because their visibilities can be accurately predicted. The following is a list of requirements on calibrators related to their individual sources of error, as described in Moellenbrock (2002):

T, G: Close-by; high flux; point-like; observe on short time scales: 10 s (low frequencies) to <1 min (high frequencies); observe at least one calibrator of known flux.

B: Strong source; in case of wide bandwidth a point-source should be chosen to avoid visibility changes across the band; time scale: often enough to track variations.

D: High flux; unpolarized; in case of a polarized source, it has to be observed over a broad range of parallactic angles.

F: Strongly polarized source; time scale: often enough to track variations; in case of a stable ionosphere, rely on ionosonde observations for empirical corrections.

A: A list of candidates for calibrators can be found at `https://science.nrao.edu/facilities/vlba/data-archive/surveys/` .

The complete set of described observational errors are, in addition to the instrumental effects of section 4.1, accounted for during the a-priori calibration process and can further be lowered by self-calibrating the source, as it is described in the sections 6.1 and 6.4.

Chapter 6

Calibration

Every scientific data need to be calibrated in order to remove instrumental errors in the measurement, caused by imperfect electronic components, as well as interstellar and atmospheric influences. According to Ros & Kadler (2009), telescopes have several sources of errors, that affect the data. The most significant effects arise from inaccuracies of the radiation collecting surface and receiver noise levels. All other technical devices and their processes (e.g., frequency conversion, digital sampling), participating in the process of data acquisition, yield additional sources of error. And, of course, a variety of control failures during observations, such as scheduling and observing errors (of human origin or technical problems) need to be corrected. The amount of error sources and their significant effect on the data (e.g., wrong source position, slewing times different than expected, other effects described in chapter 5.3) show the need of calibration before an accurate analysis can be performed.

There are different calibration methods that can be applied to correct the data for the afore mentioned effects. A first direct calibration can be derived from the known parameters of the instrument, like the geometry of an interferometer (see Sect. 6.1). While this is possible for simple and symmetric arrays, in case of VLBI, this is not feasible, since the stations are spread over large baselines and in most cases form an asymmetric array. Therefore, VLBI requires calibrator sources of well known properties in order to determine the amplitude and phase of each telescope by monitoring their gain and phase. Lastly most of the residual errors can be removed by self-calibration (see Sect. 6.4).

6.1 A priori calibration

Following the notations in Ros & Kadler (2009), if the correlation of the electric field (voltage) sampled at a pair of telescopes (i, j) has been obtained (see Eq. 4.1), the signal of antenna i $(x_i(t))$, consists of the signal of the source $(s_i(t, x, y))$ and a corrupting factor $J_i(t, x, y)$, integrated over the sky, as well as a noise term $(n_i(t))$:

$$x_i(t) = \int J_i(t, l, m) s_i(t, l, m) dl dm + n_i(t) = s'_i(t) + n_i(t). \tag{6.1}$$

$J_i(t, x, y)$ is an antenna based factor, that contains all effects that need to be calibrated (see Eq. 5.15). In some cases the contained effects can not be corrected, which only leaves careful editing of the data as a method to account for this factor.

If the signals of two telescopes (x_i, x_j) are correlated, the noise can be corrected, since the noise term does not correlate. This de-correlation can be derived from the following equation:

$$\begin{aligned}\langle x_i \cdot x_j^* \rangle &= \langle (s_i' + n_i) \cdot (s_j' + n_j)^* \rangle = \langle s_i' \cdot s_j'^* \rangle + \langle s_i' \cdot n_j^* \rangle + \langle n_i \cdot s_j'^* \rangle + \langle n_i \cdot n_j^* \rangle \\ &= \langle s_i' \cdot s_j'^* \rangle = \langle \int J_i(t) s_i(t) dl dm \cdot \int J_j^*(t) s_j^*(t) dl dm \rangle \\ &= \langle \int J_i(t) J_j^* s_i(t) s_j^*(t) dl dm \rangle.\end{aligned} \tag{6.2}$$

Even for $n_i >> s_i$ the correlation separates the desired signals from the noise term.

The dataset BE061 offers sufficient quality, so that the noise can be significantly lowered by an a priori calibration. Measured antenna system temperatures and gain elevation curves of each antenna have been used for this matter (see also Rauch et al. (2016)).

6.2 Bandpass calibration

As described in section 5.3.9, the selected pass bands have lower amplitudes at the edges of their bands (see Fig. 6.1), which have to be corrected, to regain the source flux. This bandpass filtering is performed by the Astronomical Image Processing System (AIPS) task BPASS and enabling the DOBAND option in subsequent tasks. 3C 279 served as a bandpass tracer for this correction, with LA as a reference antenna. All other antennas have been equally weighted. The corrected amplitudes are shown in Fig. 6.2 and display that this method was capable of correcting the inaccurate amplitudes at the edges of the pass bands.

6.3 Data based calibration

After all corrections that can be gained from known properties of the measurement setup have been applied, there are still residual errors present in the data which need to be analyzed carefully to regain the most accurate picture of the original source. These residual errors are still present in phase slopes, different gains across stations or channels at each station and irregular data points caused by unpredictable events. All data observed with antennas during periods of technical problems have been flagged. Additional editing of the data for outliers and suspiciously high/low flux values, further improves the performance of this a priori calibration. A summary of all flags is shown in Tab. 6.1. The following section describes the techniques on how to address these residual errors with data-based calibration.

6.3.1 Amplitude Calibration

The initially measured amplitudes are still in engineering dimensions which need to be translated into real measured flux values in Jansky by a conversion factor. This needs

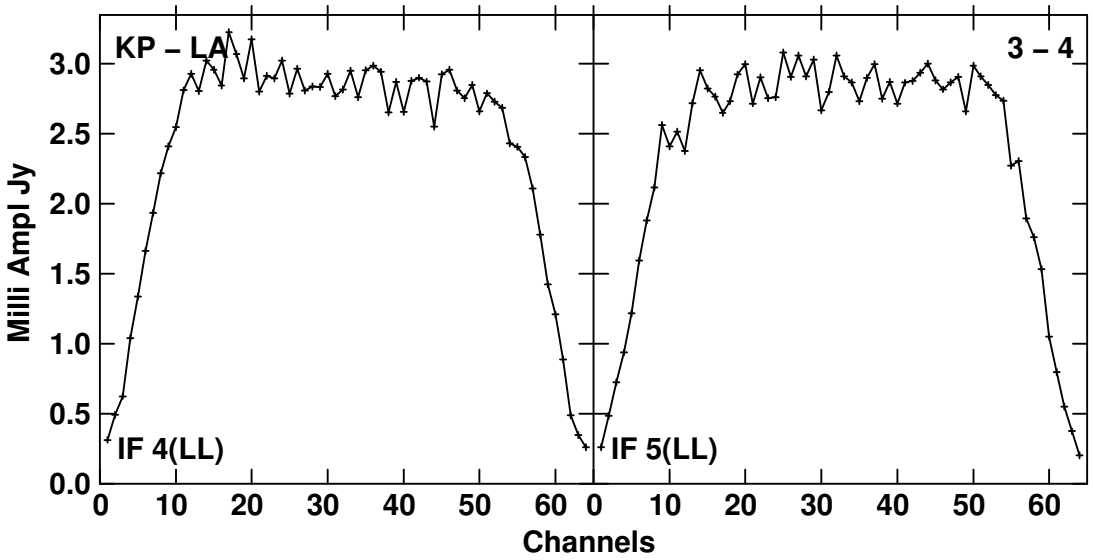

Figure 6.1: Uncalibrated amplitudes of NRAO 530 for the baseline KP-LA in LCP as a function of frequency for two subbands (IFs). Time range: 9:08:28 to 9:10:28 h UT.

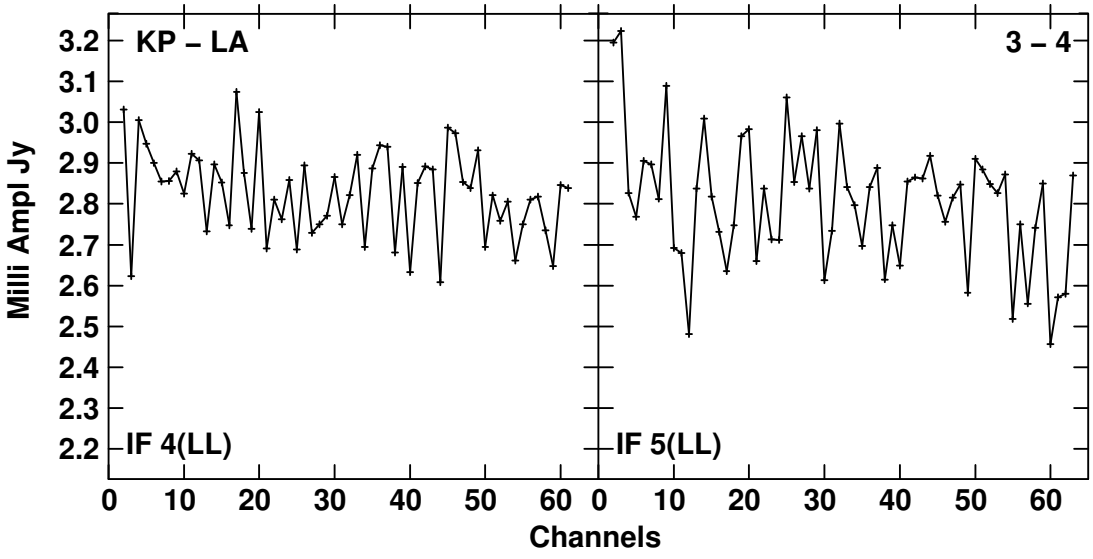

Figure 6.2: Bandpass calibrated amplitudes of NRAO 530 for the baseline KP-LA in LCP as a function of frequency for two subbands (IFs). Vector averaged cross-power spectrum. The amplitude scale has been changed compared to 6.1 in order to better show the residual small fluctuations. Time range: 9:08:28 to 9:10:28 h UT.

Station	May 16	May 17	May 18	Reason
FD		05:45-05:53		Reboot control computer
			07:30-12:30	Communication loss
	08:20-09:00, 10:40-11:01			Faulty flux values
HN		06:29-06:38	07:30-07:40	Communication loss
			07:30-07:40	Reboot control computer
		07:15, 08:30, 09:45		Faulty flux values
LA		06:04-06:20, 06:30-06:50		Faulty flux values
NL	07:42-12:30	05:45-12:30		Air Condition defective
OV	07:42-12:30	05:45-12:30	07:40-12:30	Saturated T_{sys} (LCP)
PT		10:21-10:27		Power glitches
		06:25-06:38, 09:10		Faulty flux values
			08:42-08:49	Communication loss
BR	07:42-12:30	05:45-12:30		Wideband installation maintenance

Table 6.1: Summary of flagging applied to the dataset BE061 before calibration. KP and MK had no failures.

the knowledge of the on-source system noise in Jy (SEFD, see Sect. 5.3.8). The system temperature (T_{sys}) of every antenna is continuously recorded during observations and translates into the SEFD by equation 5.10. This conversion can be performed by the (AIPS) task APCAL, by dividing the T_{sys}-values by the antenna gains contained in the TY and GC tables.

The task APCAL also includes routines to correct the data for atmospheric opacity, based on weather tables (WX table). Errors caused by opacity gain significance towards higher frequencies and can have huge effects at these bands (Moran & Dhawan, 1995). According to Leppänen (1993), the standard amplitude calibration methods were designed to operate at lower frequencies, which are less affected by atmospheric errors than at mm-wavelengths (see also Chap. 5.3). This causes a priori calibration errors to often exceed 50%. This shows the need of opacity correction, implemented optionally in the APCAL task.

A smaller effect on the amplitudes is caused by non-optimal setup of the quantizer thresholds in 2 bit (4 bit) sampling (Kogan, 1995). The AIPS task ACCOR accounts for these errors, that can cause systematic effects, by sampling based calibration adjustments.

An advanced script VLBACALA, is included in the VLBAUTIL package. This task offers the specialized VLBA algorithms and combines the antenna and quantizer calibrations described into a single task. As described in Rauch et al. (2016), these additional calibration scripts of the VLBAUTIL package have been used to accurately calibrate the presented data set.

Higher orders of error correction caused by opacity (see Sect. 5.3.3) were addressed using the AIPS task APCAL by plotting system temperatures against air mass and fitting the variations. The effects caused by the total electron content in the ionosphere (see Sect. 5.3.2) have been corrected using the AIPS script VLBATECR.

6.3.2 Positional calibration

As previously described (see Sect. 5.3), precise knowledge of the spatial antenna positions are required to gain accurate observations. This includes knowing the Earth orientation parameters, that relate the terrestrial and celestial reference frame. It describes the irregularities in the rotation of the Earth. This includes precession and nutation of the celestial ephemeris pole, which is slightly moving across the surface. Since the Earth and its atmosphere are not rigid bodies, any motion of mass within or on the surface, causes changes in its rotation. The rotation time is observed in universal time (UT1) and measures the excess time between the sidereal and terrestrial time (UT1-UTC) (see also Ros & Kadler (2009)). These parameters are applied by the AIPS task VLBAEOPS, that corrects the Earth orientation parameters provided by the VLBA correlator based on values contained in a CT table. This procedure is highly recommended for phase referencing experiments, such as the data presented in this thesis, as well as any astrometric observation.

Additional errors may arise from a non-corrected time dependent parallactic angle as described in section 5.3.4. Parallactic angle corrections have been determined by the AIPS script VLBAPANG and applied to the data set BE061.

6.3.3 Fringe fitting

In addition to the variety of already mentioned errors (see Chap. 5.3), according to Ros & Kadler (2009), imperfect geometric and clock models affect the phase to be additionally delayed. The data can also be affected by baseline-based errors which are not included in the antenna based factors. Even though correlators are designed to prevent this and time/frequency averaging is capable of additionally lowering these effects, imperfect electronics and correlated noise (RFI), which can not be distinguished from the real effects of source structure on the data (see Sect. 5.3.7), cause a certain amount of residual effects to remain in the data. Therefore, raw correlator data still has phase slopes in time (fringe rate) and frequency (delay) (see Fig. 6.3). The fringe rate causes a slope in the phases, while a delay will manifest in phases being non zero. Both are related to each other by $\phi = \nu t$. The strong effect of tropospheric water vapor on high frequencies causes the fringe rate to show significant fluctuations at these wavelengths (see Sect. 5.3.3). The effect of electrons in the ionosphere, on the other hand, is the reason for the phase delay and, therefore, has its strongest effect at lower frequencies (see Sect. 5.3.2). These slopes and delays can be corrected by fringe fitting, which self-calibrates data with first derivatives in time and frequency.

Fringe fitting is usually performed in two steps. At first, rates and delay to a chosen reference antenna are estimated by a two-dimensional Fast Fourier transform (FFT). The estimated values are then used as a first basis for a least square fit to the phases. This process will correct the offsets between different IFs and then solve for the phase to equal zero and have no delay.

Fringe fitting has been performed by solving for a minimum of two antennas and combining all IFs. The best solutions have been found for a defined SNR cutoff of 5

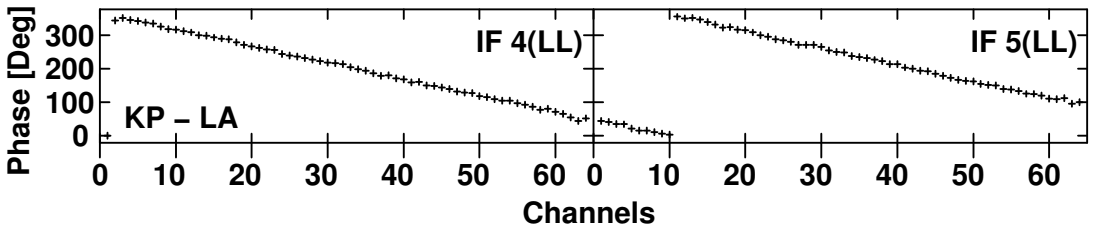

Figure 6.3: Uncalibrated phases of NRAO 530 for the baseline KP-LA in LCP as a function of frequency for two subbands (IFs). Time range: 9:08:28 to 9:10:28 h UT.

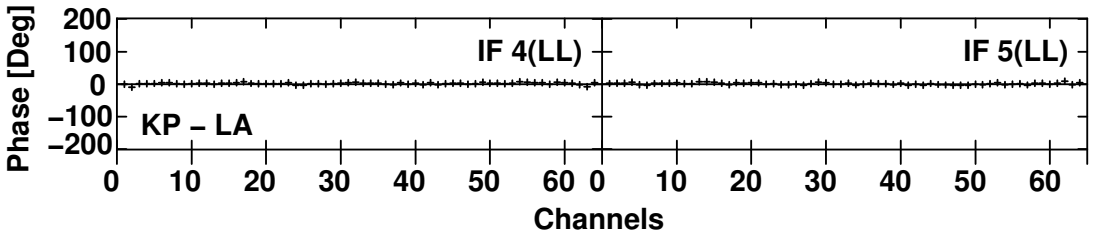

Figure 6.4: Fringe fitting results (delay-corrected solution) of the baseline KP-LA in LCP for NRAO 530 as a function of frequency for two subbands (IFs). Time range: 9:08:28 to 9:10:28 h UT.

with exhaustive baseline search of fringes in a delay window of 400 ns and 400 mHz rate window. Each target itself served as a calibrator for fringe-fitting, which has been performed using a two-point interpolation of delays and delay rates with a solution interval of 30 s. This results in 40712 good and 12568 bad solutions, which is an acceptable success rate. The calibrated phases of the presented data set are shown in Fig. 6.4.

6.4 Self-calibration

Because of residual phase errors which could not be corrected at the correlator stage, VLBI visibilities need further calibration in order to form a high quality image. Self-calibration of the data is required to remove unknown errors introduced by the instruments and residual atmospheric errors. This task is performed by using a model of the source in order to find phase errors and corrections to align this model with the real visibilities. According to Middelberg & Bach (2008), baseline-dependent errors can be described as antenna-based effects, which makes the phase error of a visibility a combination of all antenna-based errors (e.g., atmospheric delays, antenna position uncertainties, electronic drifts). The number of visibilities usually exceeds the amount of unknown phase errors and can, therefore, be used to gain additional information to generate a preliminary model. The DIFMAP task CLEAN performs this task very well and was used for all data presented in the context of this thesis (Shepherd et al., 1994).

In case of a perfect model resembling the original source properties, the residual

phase errors will only be caused by instrumental and residual atmospheric errors, which then can be corrected. This method crucially depends on the chosen model and since the true properties of the original source are in general not well known, this is an iterative process. The most simple starting model would be a point source and is commonly used as a first guess. While this will not resemble the source very well, in most cases, the first application of determined phase errors allows the evolution of this model towards a better approximation of the real source structure based on residuals caused by the different visibilities between data and model.

According to Walker (2002), the iterative process starts by solely self-calibrating the phases. If the progress of this self-calibration slows, amplitude calibrations may be added. It is possible to emphasize different parameters during this hybrid mapping process, such as taper, robustness, or (u, v)-range. This process is now continued with an improved model until the modeled and observed visibilities converge and thermal noise level is reached. It is important to compare the iteratively generated model with the initial, not self-calibrated, data in order to avoid the data converging towards a faulty model. This comparison has been performed for all maps shown in chapter 7 and shows the necessity of the robustness tests performed in section 7.2.

A requirement for this method to produce reliable result is that the SNR has to be least 5 times higher within the atmospheric coherence time, which is the time it takes for the fastest component to change a few tens of degrees (Cotton, 1995). This makes the time scale of tropospheric water vapor content fluctuations a limit for the integration time used in the cleaning process. This scale is frequency depended and the integration times range from 2 min (5 GHz) to 30 s (43 GHz). At higher frequencies (tens of GHz) VLBI stations are less sensitive, which limits the observable sources at these frequencies, but fainter sources can still be observed within the atmospheric coherence time using phase referencing.

According to Middelberg & Bach (2008), the performance of an array, in terms of regaining complex structures, depends on the number of stations and forms another boundary condition for this method. The number of antenna gains for N stations is (N-1), because one stations phase is a free parameter and set to zero. This makes the ratio of number of constraints to the number of antenna gains the quotient of number of baselines ($N(N-1)/2$) and number of antenna gains ($N-1$):

$$N/2 = N(N-1)/2 \times (N-1)^{-1}. \tag{6.3}$$

6.4.1 Model fitting

The model generated during the iterative process of self-calibration is commonly first realized by a model of delta components at the position of pixels with expected fluxes, as described in section 4.3.3.1. Even though, this pixel based model is capable to accurately resemble fine source structures, in cases of small numbers of free parameters, it is useful to generate a much simpler model based on circular or elliptical components. This simple approach also offers a good possibility to test a previously generated delta component model. DIFMAP offers the possibility to define components by their positional parameters flux, radius, and position angle; as well as their structural parameters

major axis, axial ratio, and angle of the major axis. In parallel to the previously described self-calibration procedure (see Sect. 6.4), these parameters can then be fixed or left variable during the iterative process of self-calibration until the model and real visibilities converge at thermal noise levels. Such a model fitting has been performed for the maps shown in Fig. 7.3.

6.5 Calibration and Imaging

The included standard algorithms of AIPS are capable of phase and delay calibration as well as fringe fitting. The additional calibration scripts of the VLBAUTIL package, offering specialized VLBA algorithms, has also been used to accurately calibrate the presented data set.

Maps of all sources have been produced using the standard hybrid mapping process as described in chapter 6.4. Standard CLEAN methods included in the AIPS and DIFMAP software (Shepherd et al., 1994) package have been used to produce maps averaged over 15 s at a resolution of 0.3 mas. During the iterative determination of the model, the beam has been enlarged in three stages starting from 1/3 over 1/2 to its initial value.

Sgr A* offers a flux around 1 Jy at 7 mm, based on previous observations, which makes it challenging to detect this low-elevation source at the longest baselines for the scatter-broadened image, which implies low visibilities at these baselines. The data set BE061 was subject to many data deteriorating problems and technical difficulties during the observations, such as cooling problems (NL), technical maintenance for a wideband upgrade (BR) or saturated system temperatures (OV), resulted in a changing array setup during the observations and left only a maximum of up to 6 stations for analysis (see Tab. 6.1 for a summary of these problems). The maximum detected baselines on each day reached $220 \times 10^6\lambda$ (May 16; stations: FD, KP, LA, OV, PT), $110 \times 10^6\lambda$ (May 17; stations: FD, KP, LA, PT), and $340 \times 10^6\lambda$ (May 18; stations: BR, KP, NL, OV, PT). The only stations, present on all three days, are KP, PT, and MK. In any case Sgr A* has not been detected on the longest baselines towards MK. Even though a few detections at expected flux values are present, these could not be modeled accurately, because their values raised to implausible fluxes during the hybrid mapping process and have, therefore, been excluded from the analysis. Gwinn et al. (2014) and Johnson & Gwinn (2015) report that these long baseline visibilities might by caused by scattering, which can introduce substructures at these baselines. This scattering would add noise to long-baseline visibilities, which could explain the detected visibilities. Additionally, left-handed circular polarization (LCP) provided acceptable data quality (except OV) and therefore, right-handed circular polarization (RCP) data was disregarded from the flux analysis, but still provides a good test for the later described change in source structure (see Sect. 7.2). The corresponding LCP map of every day, covering a time range of 6 hours each, are plotted in Fig. 6.5.

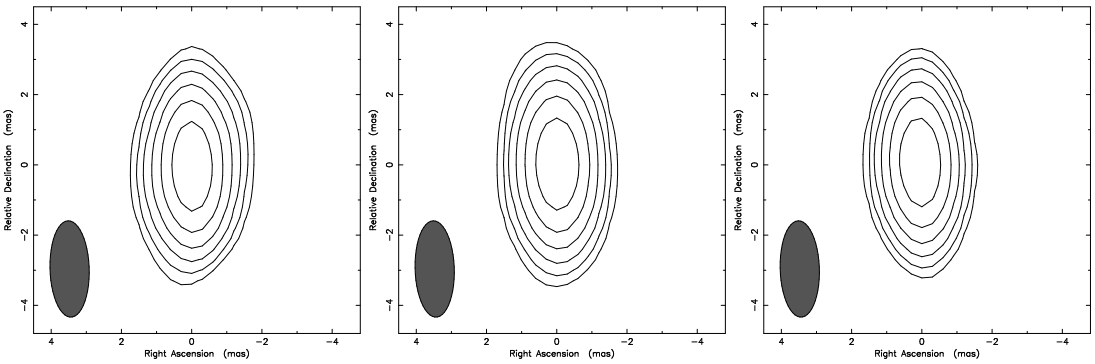

(a) (b) (c)

Figure 6.5: Uniformly weighted LCP contour images of Sgr A*. The corresponding dates and peak flux intensities are: (a) May 16 2012 8-12 h UT, 1.11 Jy/beam. (b) May 17 2012 6-12 h UT, 1.34 Jy/beam. (c) May 18 2012 8-12 h UT, 1.17 Jy/beam. All maps have been convolved with a common beam of 2.74×1.12 mas at 1.76°. The plotted contour levels represent 1.73%, 3.46%, 6.93%, 13.9%, 27.7%, 55.4% of the peak flux intensity (taken from Rauch et al. (2016)).

6.5.1 Calibrators

According to Rauch et al. (2016), the data set BE061 offers three calibrators, which deal as fringe tracers and amplitude calibrators and have been observed regularly during the measurement campaign (see Sect. 5.1). All of these are extragalactic sources of well known properties. 3C 345 and 3C 279 showed changing system temperatures and other uncorrectable station and scan based flux errors and have therefore, not been considered for analysis, except for bandpass calibration and testing the a-priori calibration to be reliable. The remaining calibrator NRAO 530 fortunately has been observed with acceptable data quality and has been used for all calibration tasks. The flux of this source remained constant at (2.42 ± 0.04) Jy during the whole experiment and serves as a reliable offset calibrator for all other flux measurements. This results in a relative error of 1.7% which has been adopted for all amplitude measurements within this data set. The separation of this calibrator from the science target of $\sim 16°$ offers the possibility of errors arising from effects on smaller scales to still be present within the data, but closer calibrators, such as the phase referencing sources, which were too faint to serve as a calibrator, are not available within this data set. These residual errors on the presented flux measurement are considered to be lower than the detected changes of its intensity and therefore, the presented flux analysis is reliable.

In order to test the applied calibration, the correction factors for each station compared to their uncalibrated values have been plotted for NRAO 530 and Sgr A* (see Fig. 7.1). Different correction factors between these sources would mean, that residual errors have not been calibrated accurately. For this analysis, a few bad visibilities from PT at the start and end of the data set had to be excluded. Visibilities detected at FD showed uncorrectable offsets with respect to the other stations and has also not been

considered for this test of calibration accuracy. The systematic station based correction for NRAO 530 are in the order of ∼18% and are found to be in good agreement with the factors of Sgr A*. This shows that the applied calibration was capable of correcting these offsets consistently.

6.6 Constraints on the data

As described in Rauch et al. (2016), 7 mm observations of Sgr A* are subject to several limiting effects at very low elevations. The VLBA was designed to operate at longer centimeter wavelengths, steeper gain curves as well as higher residual and focus errors. In addition to these effects, there are several other sources of deteriorating effects which affect the data (see e.g., Lu et al. 2011b). At these high frequencies, changing weather conditions and opacity fluctuations have a more significant effect, compared to other radio bands (see also Sect. 5.3.2 and 5.3.3).

The low elevation of Sgr A* at the VLBA stations, located on the northern hemisphere (see Fig. 5.1), makes it impossible to correct all extrinsic effects and causes residual calibration inaccuracies to remain present within the data. As a result of its low elevation the (u, v)-track and beam sizes are elliptical (see Fig. 6.6), which causes a direction depended positional accuracy. For a beam size of 1.116×2.743 at $1.757°$, as it has been used for all maps concerning Sgr A*, the highest accuracy is provided along the minor axis at $91.757°$.

Despite these constraints, it was possible to accurately calibrate the data and produce clean maps of Sgr A* that are discussed in the following chapter. Several light curves have been derived from the intensities provided by these maps that show consistent values and trends with respect to directly measured flux estimates of the direct Fourier transform (DFT) (see Fig. 7.1).

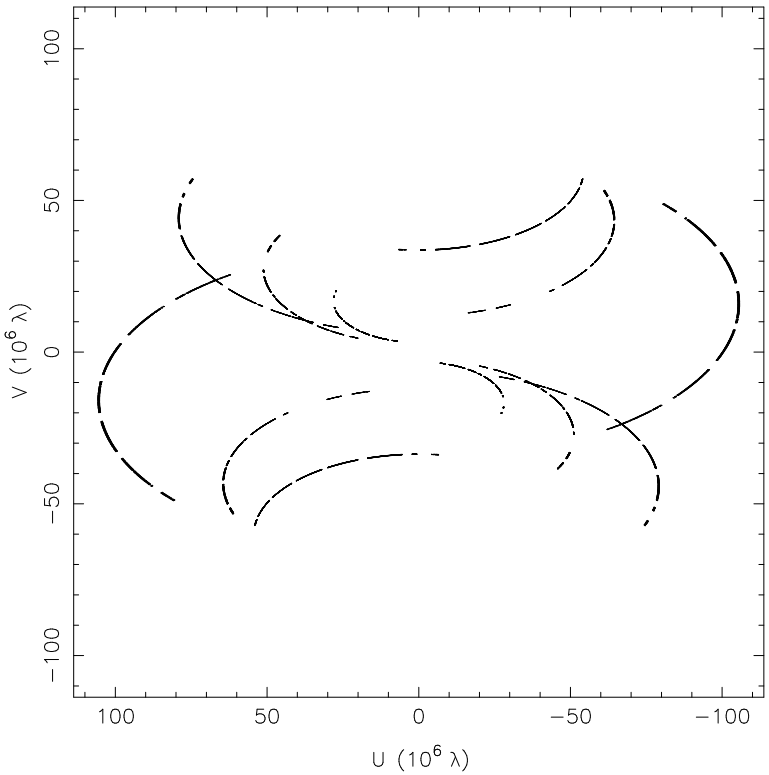

Figure 6.6: (u, v)-coverage of Sgr A* on May 17 2012 (6-12 h UT). Available stations FD, KP, LA, and PT (taken from Rauch et al. (2016)).

Chapter 7

Results and analysis

This chapter summarizes all results that can be gained from the calibrated data of the measurement campaign BE061 performed on May 16 - 18 2012 in parallel to NIR VLT-observations. Clean maps of the 7 mm (43 GHz) data have been generated and used to determine a light curve and time delay with respect to the NIR observations. All methods to achieve these results, together with several tests of their robustness are described in detail in the following sections.

7.1 Flux analysis

The presented 43 GHz observation on May 17 2012, as published in Rauch et al. (2016), have been triggered by a previously detected NIR flare at the VLT. The NIR lightcurve shows peak flux values of 6.64 mJy at 5:30 UT (Fig. 7.1). Sgr A* has been detected to remain at constant flux values of 1.14 ± 0.02 Jy on May 16 and 1.0 ± 0.02 Jy on May 18, based on their map peak values. On these dates the source showed no excessive flux and is, therefore, determined to be in a quiescent state. The mean value of (1.07 ± 0.02) is, thus, considered as the flux of Sgr A* during its non-flaring state and will be used as the basis to detect the flares of Sgr A*.

The 7 mm light curve of May 17 has been determined by plotting the DFT of Sgr A* and NRAO 530 (Panel (b) in Fig. 7.1). The DFT is a reliable method to measure the intensity evolution of a source, since it is not affected by errors arising from the iterative calibration process and is, therefore, considered an unprejudiced approach. The calibrator NRAO 530 shows small variations of its flux that are caused by residual uncertainties. These fluctuations have been removed to gain more accurate flux values of Sgr A*. The difference of every data point of NRAO 530 from its expected mean value has been determined and then subtracted from the values of Sgr A* in percentages of its mean value. This will lower the observational errors to a level close to the real intrinsic flux of Sgr A*. The resulting detrended light curve of Sgr A* is shown in panel (c) of Fig. 7.1.

The detrended light curve shows an increasing flux density of Sgr A* from 0.97 Jy to 1.17 Jy peaking at ∼9:30 UT. The intensity raises within ∼2.5 hours towards its maximum and then starts to drop again at 10-12 h UT, just before the end of the observing session. The rising flux rate of this intensity outburst amounts to (0.08 ± 0.02) Jy hr^{-1} over 2.5 hours. The incomplete coverage of the flare towards its end makes it impossible to determine the rate at which the flare falls back to its quiescent level, but it is expected to be the same as the rising rate.

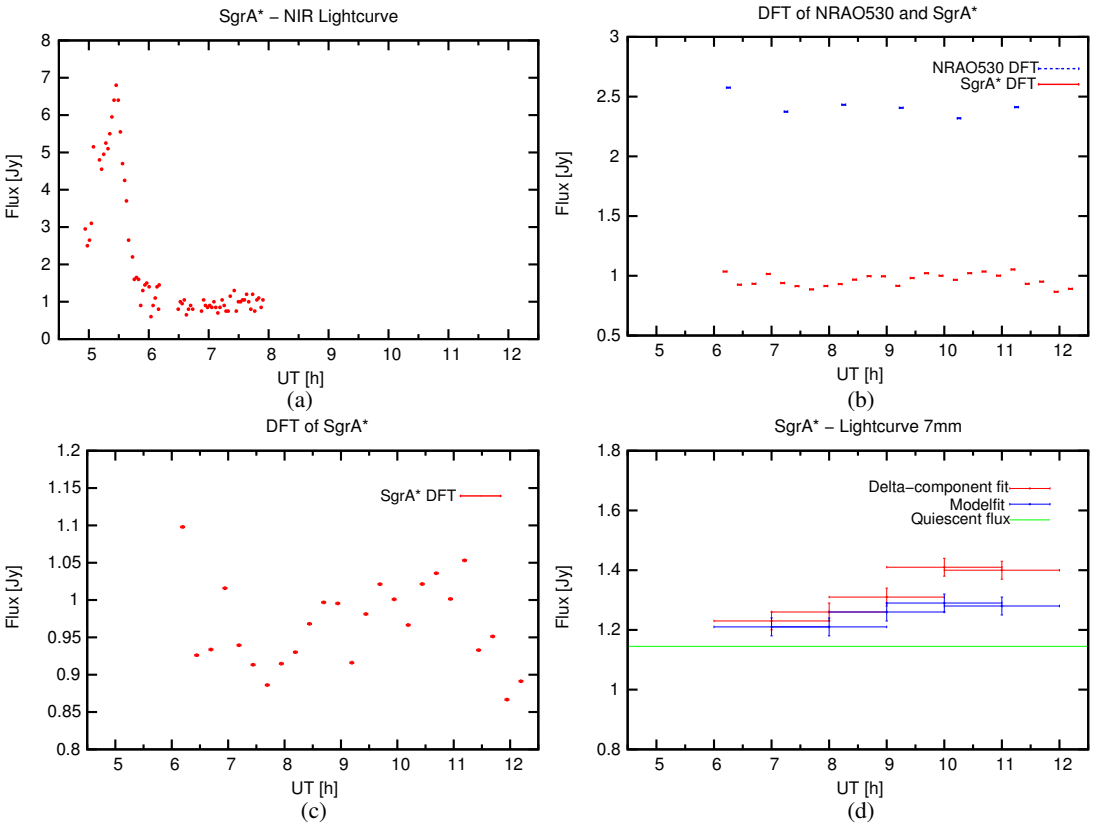

Figure 7.1: 7 mm and NIR light curves of Sgr A* on May 17 6-12 h UT 2012. (a) NIR K_s-band (2.2 μm) light curve, produced by combining 0° and 90° polarization channels (taken from Shahzamanian et al. (2015)). (b) DFT of the 7 mm flux of Sgr A* (red) and the calibrator NRAO 530 (blue) (taken from Rauch et al. (2016)). (c) Detrended DFT of Sgr A* at 7 mm (taken from Rauch et al. (2016)). (d) 7 mm light curve provided by the intensities of the two-hour maps of Sgr A* (see Fig. 7.2, taken from Rauch et al. (2016)). Obtained fluxes are based on delta-component maps (red) and model fitting (blue), while the errors are derived from to the formal error of 1.7% found for the calibrator NRAO 530. Systematic errors in the order of ∼18% are not included, which should be corrected in the calibration process.

Time UT on May 17 in [h]	S_{peak} [Jy]	RMS noise [Jy]
06-08	1.23	0.0017
07-09	1.26	0.0017
08-10	1.31	0.0014
09-11	1.41	0.0015
10-12	1.40	0.0016

Table 7.1: Observing times, peak flux and RMS noise values for all maps of May 17 presented in Fig. 7.2. All maps have been restored with a beam of (2.74×1.12) mas at 1.76°. The plotted contour levels represent 1.73%, 3.46%, 6.93%, 13.9%, 27.7%, 55.4% of the peak flux intensity.

Time UT on May 17 in [h]	S_{peak} [Jy]	RMS noise [Jy]
06-08	1.21	0.0016
07-09	1.21	0.0015
08-10	1.26	0.0012
09-11	1.29	0.0013
10-12	1.28	0.0013

Table 7.2: Summary of all map parameters for Fig. 7.3. All maps have been restored with a beam of (2.74×1.12) mas at 1.76°. The plotted contour levels represent 1.73%, 3.46%, 6.93%, 13.9%, 27.7%, 55.4% of the peak flux intensity.

The data of May 17 have been split into five overlapping two-hour bins. Each individual set has been mapped, using the afore mentioned hybrid mapping method (see Sect. 6). The resulting self-calibrated maps convolved with delta components are plotted in Fig. 7.2. Additionally, a model fit has been performed, by putting circular components at the positions suggested by the delta component fit, and then solving for size, radius and positional degree, using the DIFMAP (Shepherd et al., 1994) algorithm MODELFIT. The corresponding maps are plotted in Fig. 7.3. All maps are shown with a common restoring beam of 1.116×2.743 at 1.757°, to make them comparable with each other.

The detected map peak values in Jy/beam derived from delta- and circular components are plotted in panel (d) of Fig. 7.1. Both models are consistent with each other, in terms of accurately reproducing the source structure and flux evolution. The fact that the flux values of the circular component model fits are consistently lower than their delta component values arises from assuming a more simple model, which less accurately resembles the intrinsic source structure and results in loosing some flux. The detected intensity raises from 1.23 Jy (6:00-8:00 UT) to 1.41 Jy (9:00-11:00 UT) on May 17, which is significantly above its quiescent flux level and in good agreement with the flux values detected at the shortest baselines. Short baselines offer a much bigger beam, which covers the whole source and therefore, measure the total observable flux. This makes them a good tracer for the real flux values of the source and can be used to test the current model of the clean maps. Another proof for this variation of intensity to be real is its presence on independent baselines, which excludes station-based errors as a possible source of this flux excess. The flare raises at a rate of $(0.06 \pm 0.02)\,\mathrm{Jy\,hr^{-1}}$ over 3 hours which is consistent with the DFT rate within the given errors.

A lot of information can be gained by the time delay between the individual ob-

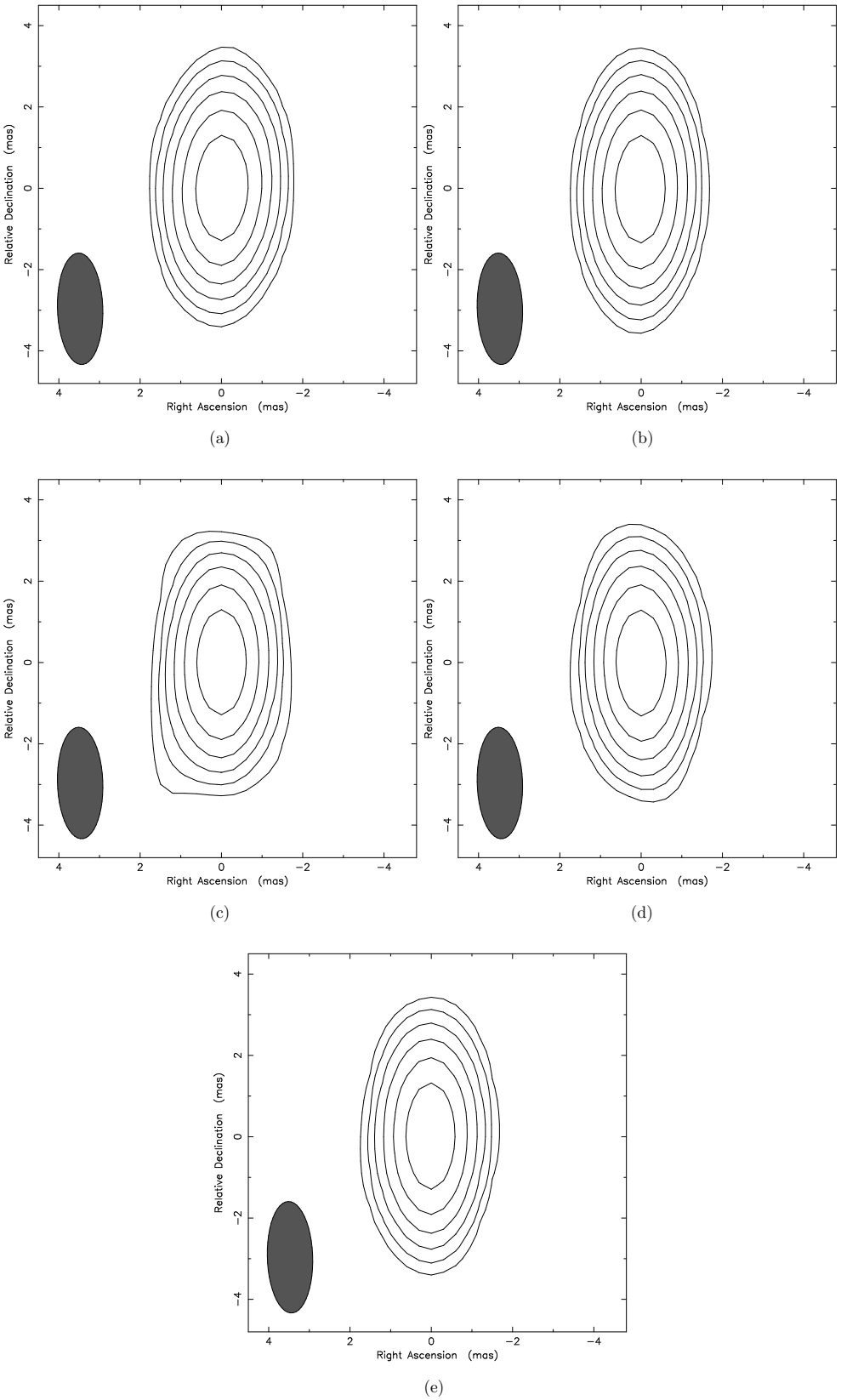

Figure 7.2: Time segmented two hour LCP contour images of Sgr A* observed on May 17 2012. (a) May 17 6-8 h UT. (b) May 17 7-9 h UT. (c) May 17 8-10 h UT. (d) May 17 9-11 h UT. (e) May 17 10-12 h UT. Map parameters can be found in Tab. 7.1 (taken from Rauch et al. (2016)).

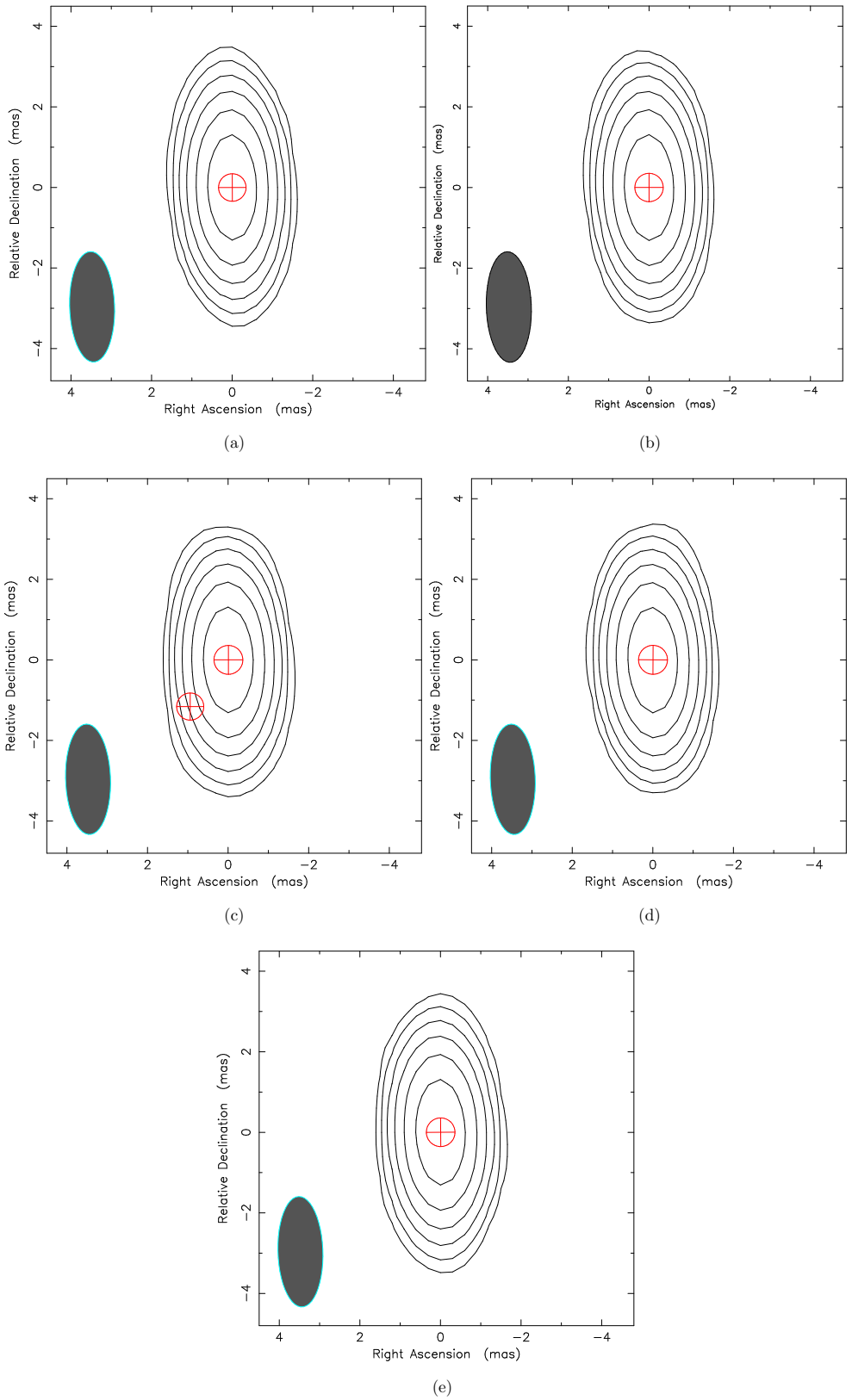

Figure 7.3: Model fits of Sgr A* on May 17 2012 6-12 h UT for five overlapping two-hour segments. The time range of 8-10 h UT (c) is best fitted by a two component model indicating an extended morphology during the flaring state. (a) May 17 6-8 h UT. (b) May 17 7-9 h UT. (c) May 17 8-10 h UT. (d) May 17 9-11 h UT. (e) May 17 10-12 h UT. Summarized map parameters can be found in Tab. 7.2 (altered from Rauch et al. (2016)).

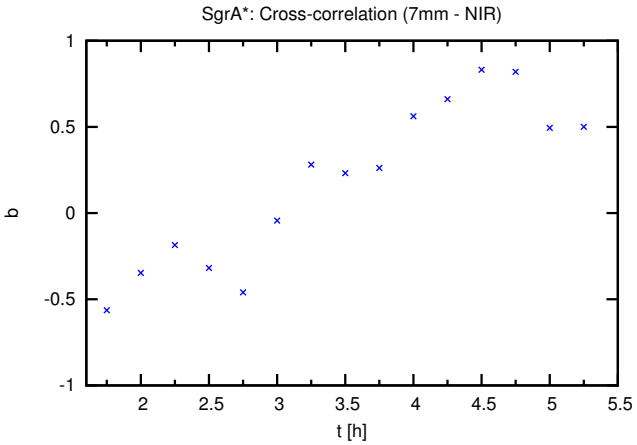

Figure 7.4: Cross-correlation coefficient of the NIR and 7 mm light curves during the flaring phase of Sgr A* on May 17 2012.

serving frequencies. For this reason the delay of the 7 mm data with respect to the NIR data has been determined by a cross-correlation analysis of the corresponding light curves of Fig. 7.1. This method measures the correlation of two series, in terms of a defined correlation coefficient (b), and can be used to determine the incremental difference between two individual data sets. A perfect correlation is described by a values of 1, while a coefficient of -1 indicates a correlation with the inverse of a series. The correlation coefficient is defined by:

$$b = \frac{\sum_{i=1}^{n}(x_i - \bar{x})(y_i - \bar{y})}{\sqrt{\sum_{i=1}^{n}(x_i - \bar{x})^2 \sum_{i=1}^{n}(y_i - \bar{y})^2}}. \tag{7.1}$$

b: Correlation coefficient.
x_i, y_i: Individual points of the data sets x and y.
$\bar{x}, \bar{y}$: mean values of the data sets x and y.

The correlation coefficient for May 17 is plotted in Fig. 7.4. The derived time delay between NIR and 7 mm amounts to (4.5 ± 0.5) h at a value of $b = 0.83$. The error of 0.5 h arises from the time range of coefficient values above 68%. This delay is consistent with values of up to 5.25 h found by Yusef-Zadeh et al. (2009) between NIR/X-ray and 43 GHz observations.

7.1.1 Closure amplitudes

As described in Jennison (1958), it is possible to form a function η from the fringe moduli recorded at different telescopes that represents a relative amplitude measure of the source. η is defined by:

$$\eta = \frac{|AB| \times |AC|}{|BC| \times |A|^2} \tag{7.2}$$

|IJ|: moduli of the fringe systems between stations I and J.
$|A|^2$: total power of the source observed at station A.

This equation can be expressed in terms of voltage gains (g_i), input signals at three stations (α, β, γ) and the amplitudes of the Fourier transform for each baseline ($F(ab), F(bc), F(ac)$). The mean amplitudes are then expressed by $g_1\alpha$, $g_2\beta$ and $g_3\gamma$ with a conversion gain factor (G_i) for the cross multiplying recorder systems between the individual channels:

$$\begin{aligned} |AB| &= G_1 g_1 \alpha g_2 \beta F(ab) \\ |AC| &= G_3 g_1 \alpha g_3 \gamma F(ac) \\ |BC| &= G_2 g_2 \beta g_3 \gamma F(bc) \\ |A|^2 &= G_4 (g_1 \alpha)^2 \end{aligned} \tag{7.3}$$

G_4: conversion gain of the total power recorded at station A.

This transforms equation 7.2 into:

$$\eta = \frac{G_1 g_1 \alpha g_2 \beta f(ab) \times G_3 g_1 \alpha g_3 \gamma f(ac)}{G_2 g_2 \beta g_3 \gamma f(bc) \times G_4 (g_1 \alpha)^2} = \frac{f(ab) \times f(ac)}{f(bc)} \times \frac{G_1 G_3}{G_2 G_4}. \tag{7.4}$$

This does not depend on the gain of the individual telescopes except for the final cross multiplying and power recording unit. If the channels B and C can be connected, the last term yields a normalizing function K that corresponds to a correlation coefficient of unity between these channels:

$$K = \frac{G_1 G_3}{G_2 G_4}. \tag{7.5}$$

A general operational function $\eta^{'}$ can be derived from this equation by substituting K in equation 7.4:

$$\eta^{'} = \frac{|AB| \times |AC|}{K \times |BC| \times |A|^2} = \frac{f(ab) \times f(ac)}{f(bc)}. \tag{7.6}$$

This now only yields amplitude functions of the Fourier transform of the source's brightness distribution and may be used to determine a relative measure of the amplitudes. In this sense it is only required to know the amplitudes of two baselines in order to derive the third amplitude with this formula.

The Closure amplitudes for the presented data of BE061 during its quiescent state on May 16 (red) and during a flaring period on May 17 (blue) are shown in the Fig. 7.5. Since Sgr A* has only been detected by the stations FD, KP, LA and PT on May 17, this set of stations is the only one shown. Even though May 16 would offer

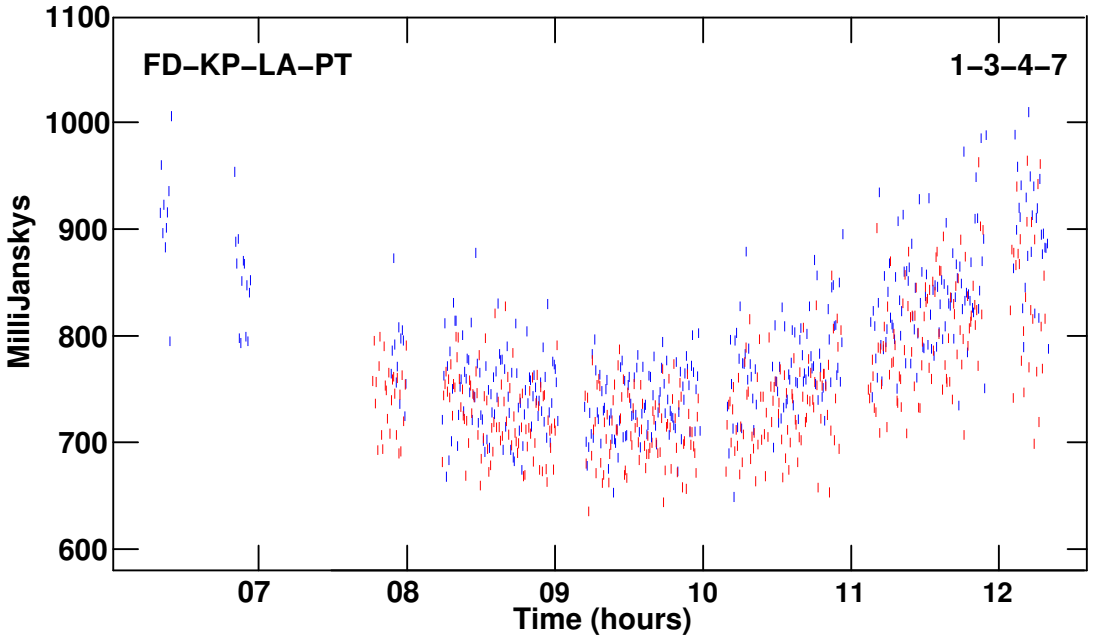

Figure 7.5: Closure amplitudes for Sgr A* on May 16 (red) and May 17 (blue).

other additional stations for this analysis, those have been excluded because they can't be related to any other quadrangle. The data have been averaged over 6 s per point on all baselines, which is equal to the data integration time. This solution interval will disregard inadequately aligned points and prevents negative effects on the data. The shown closure amplitudes are spread over a wide range of about 150 mJy which is probably caused by Rician noise bias due to averaging. This noise makes it hard to see flux changes, but comparing the flaring amplitudes with those obtained for the quiescent phase shows that the amplitudes of May 17 are slightly above the values associated with the quiescent state. Especially for time ranges later than 9:30 h UT the blue points show higher values than their quiescent red counterpoints of May 16. This is another indication for the flux excess on this time range as shown by the light curves in Fig. 7.1.

7.2 Structure analysis

In parallel to Rauch et al. (2016), Sgr A* is considered to be in a flaring state on May 17. The particular analysis of this date shows Sgr A* to appear as a featureless source during its initial quiescent phase (see Fig. 7.2). During the flaring state this source develops a secondary feature at $\sim$1.7$\pm$0.3 mas (delta component model) and 1.5 mas (circular component model) towards the south-east. The most significant change of its structure appears shortly (8:00-10:00 UT) before the peak of the flare at 9:00-11:00 UT. This feature has been tested with different cleaning methods by changing the positions of clean windows and changing the beam enlargement process during the hybrid mapping

process, as described in section 6.5. All approaches produced a somewhat pronounced secondary feature at the expected position. This indicates that this is a real structure, present in the data, because faulty detected components caused by random noise fluxes would appear in a very random fashion. The robustness of this secondary component is way above a random effect and appears continuously even if the detected components are deleted during the mapping process. This excludes false detections caused by clean-window-bias, faulty model components or excessive noise values and shows that all available tools for testing such a feature point towards a real data feature.

The previously described model fit, using circular components, offers an additional, less error-prone, test for such a source structure (see Fig. 7.3). The components of the modeled maps are well above the scattering size at 7 mm and show the same secondary feature, as indicated by the delta component maps. A two-component model at the time of the most significant change in morphology during 8:00-10:00 UT is favored over a single component fit. The best fit of a two component model, consisting of a central 1.55 Jy component and a secondary 0.02 Jy component at a distance of 1.5 mas under 140° (east of north) can be fitted with a reduced $\chi^2 = 0.34$, while a single component approach only yields $\chi^2 = 0.54$.

Furthermore, such a secondary component should be present in both polarizations, because there is no a priori reason to assume that this secondary component will have a polarization above the low polarized central component. Therefore, LCP and RCP should offer an equal source structure. Even though, the RCP data offers poor data quality, it was possible to produce a map of acceptable quality during the flaring period (see Fig. 7.6). This yields another test for the true existence of this secondary component. In order to compare the structure of the RCP map to LCP maps, the areas of detected delta components were determined by deriving a mean position and angle for each map. The position is derived from the center of the area covered by delta components in each map and the error arises from the dimension over which components have been detected by the clean algorithm. The resulting positions of (1.7 ± 0.3) mas at $(126 \pm 16)°$ for LCP and (1.8 ± 0.2) mas at $(138 \pm 9)°$ for RCP are consistent with each other and the circular component fit within their error limits.

Other authors report the 7 mm structure of Sgr A* to be described by an elliptical Gaussian of $35.4 \times 12.6\, R_S$ at an position angle of 95° east of north (Bower et al., 2014). This scale is much lower than the reported structure caused by a secondary component of 0.02 Jy at 1.5 mas at 140° (circular component model), which arises from the poorer data quality of this measurement campaign.

As reported by Bower et al. (2014), scattering still needs to be considered at 7 mm and can cause a secondary component by refractive noise, which is capable of adding artificial compact features at long baselines (Gwinn et al. 2014; Johnson & Gwinn 2015). The refractive time scale for Sgr A* is ∼3 months at 7 mm (Akiyama et al. 2013) and does not affect the presented two hour maps of this thesis. Sgr A* has also only been detected on short baselines up to 110 Mega-λ. These small time scales and short baselines, therefore, exclude interstellar scintillation as an origin of the secondary component.

The consolidation of different cleaning methods, delta- and circular model fits as

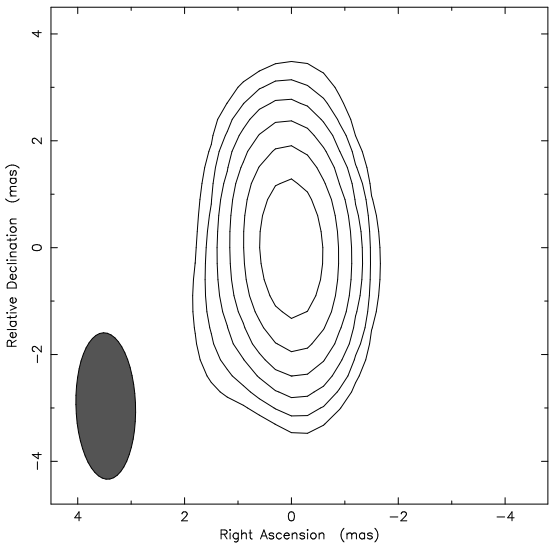

Figure 7.6: Clean map of Sgr A* on May 17 2012 (8-10 h UT) in RCP. The map has been convolved with a beam of 2.74×1.12 mas at 1.76° and plotted with contour levels at 1.73%, 3.46%, 6.93%, 13.9%, 27.7%, and 55.4% of the peak flux density of 1.5 Jy/beam (taken from Rauch et al. (2016)).

well as comparison of LCP with RCP data provides a solid hint towards the existence of this component. While all of these tests are still subject to residual calibration errors (see Sect. 5.3 and Chap. 6) or human bias, it is useful to analyze the closure phases of this date, which provide an unbiased parameter to measure the symmetry of a source.

7.2.1 Closure phases

A set of n stations can span $\frac{1}{2}(n-1)(n-2)$ triangles. Within these closure triangles the phase of the complex Fourier transform can be determined and is a calibration independent measure of the symmetry of the source (see Fig. 7.7). Following the notations of Jennison (1958), if the signal from Antenna A is defined as the phase reference and the origin of the phase transform is considered to be zero within the source, then the argument of the fringes generated in a triangle of telescopes (ABC) by the baselines AB, BC and AC are defined as:

$$AB : \xi_{AB} + \psi_B + \delta_B + \omega_B(t). \tag{7.7}$$

$$BC : \xi_{BC} + (\psi_C - \psi_B) + (\delta_C - \delta_B) + \omega_C(t) - \omega_B(t). \tag{7.8}$$

$$AC : \xi_{AC} + \psi_C + \delta_C + \omega_C(t). \tag{7.9}$$

ξ_{ij}: Phase of the Fourier transform at baseline ij ($\xi_{ij} = \xi_i - \xi_j$).

ψ_i: Phase angle introduced by the position of the source with respect to the collimation plane at i.

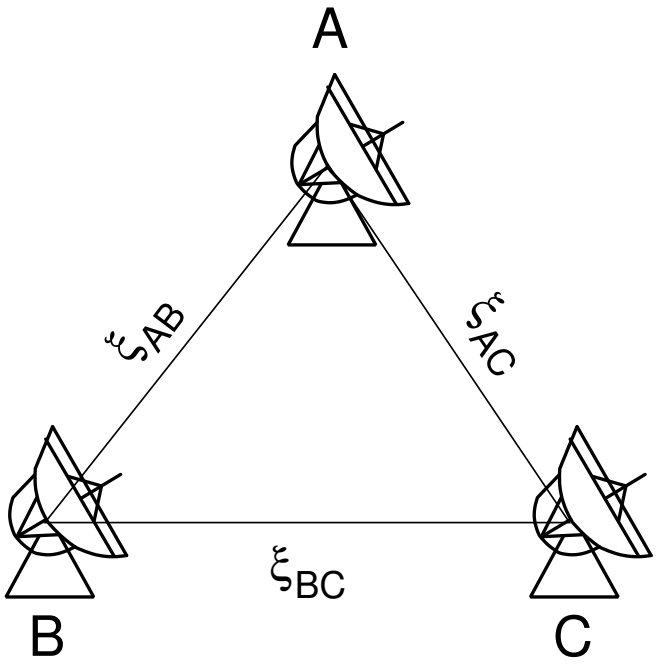

Figure 7.7: Illustration of a closure triangle.

δi: Phase error of the equipment at i.

$\omega_i(t)$: Time variable phase rotation of scans at telescope i.

This results in a total closure phase (ϕ_{ABC}) of

$$\phi_{ABC} = \xi_{AC} - \xi_{AB} - \xi_{BC} = \xi_A - \xi_C - \xi_A + \xi_B - \xi_B + \xi_C = 0. \tag{7.10}$$

This equation is independent of phase errors and angular velocity of the phase rotation. ϕ_{ABC} measures the relative phase contributions solely caused by the structure of the source. Since there is no information of the position of the source with respect to the collimation plane, the absolute phase can not be measured directly, but the symmetry can be analyzed. A deviation from a point source will, therefore, manifest in non-zero closure phases values.

The structure of a source depends on the model, derived during the hybrid mapping process. Even with a cautious and unbiased approach, faulty detected components can produce non-intrinsic source morphologies. Therefore, it is necessary to cautiously test the resulting map (see also Rauch et al. (2016)). Besides the previously described tests, using different methods of model acquisition and analyzing polarizations, closure phases offer a calibration independent measure of the symmetry of a source and are, therefore, a reliable method of testing the deviation of Sgr A* from its assumed point-like structure. Closure phases are the phase quantity of the complex visibilities and are, thus, free of any station based phase errors.

The symmetry of Sgr A* during the flaring period on May 17 has been analyzed by plotting the closure phases of 30 min averaged (u, v)-data. Figures 7.8 and 7.9 show the corresponding four closure triangles in LCP and RCP of this date. Unfortunately, May 18 could not be considered in the context of this analysis, because, owing to a changing array setup, there are no closure phase values for this date, which are also present on the other days. A mean phase for the whole sample, as well as for every set of triangles has been determined and is summarized in Tab. 7.3. The total sample average amounts to $(0.5 \pm 0.2)^\circ$ in LCP and $(0.0 \pm 0.1)^\circ$ in RCP. As comparison to its quiescent state, the closure phases in LCP and RCP on May 16 are shown in figures 7.10 and 7.11. The total sample average of this date amounts to $(0.2 \pm 0.3)^\circ$ (LCP) and $(-1.6 \pm 0.8)^\circ$ (RCP) respectively. Therefore, all closure phases have to be considered to be zero within their error limits.

A closer analysis of the LCP closure triangle FD-KP-PT on May 17 (Fig. 7.8), reveals a slight increase of their phase values that exceed two sigma at 8-10 h UT coinciding with the most significant change of its source structure (see Fig. 7.2). Other LCP triangles on May 17 don't offer a comparable trend, but also show some random values exceeding the range of two sigma. The RCP closure phases of May 17 (Fig. 7.9) show a stronger deviation from zero up to $\pm 5^\circ$ for the triangles FD-KP-PT and FD-KP-LA that also appear during 8-10 h UT as indicated by the LCP phases.

The closure phases of FD-KP-LA provide an additional maximum deviation of its phases during 6-8 h UT which could, even with most careful and exhaustive cleaning, not be reproduced by the corresponding clean maps. A possible reason, that this feature is not present in the source structure might arise from the circumstance that the secondary component is really faint and might still be hidden within the thermal noise on this early time range during which Sgr A* is just slightly above the horizon and encounters a larger amount of atmosphere.

The LCP closure phases observed during the quiescent state of Sgr A* on May 16 show overall values that are closer to zero, which indicates a difference of the source symmetry to be present between these dates. In RCP this date offers some large phases, but the highest values are only found for phases that are subject to huge errors, caused by the previously described lower quality RCP data of this campaign. These phases have therefore to be taken carefully into account.

The higher closure phases during the flaring state of Sgr A* with respect to the quiescent data together with the consistently deviating values during 8-10 UT between LCP an RCP on May 17 point towards a small change in source structure, as it has been detected by the faint secondary component of 0.02 Jy shown in the maps based on delta (Fig. 7.2) and circular components (Fig. 7.3).

Previous closure phase values of $(0 \pm 40)^\circ$ for VLBI observations at 1.3 mm with an Earth scaled triangle of SMT-JCMT-CARMA have been reported by Fish et al. (2011). Broderick et al. (2011) determined, that accretion flow models are capable of producing closure phase values up to $\pm 30^\circ$. The reported maximum 7 mm values of $\approx 5^\circ$ presented in this thesis are much lower and thus, are not excluded by the values of (45-90)° at 1.3 mm, as reported by the current literature (Broderick et al., 2011). Whether such small values can cause the observed secondary component has still to be

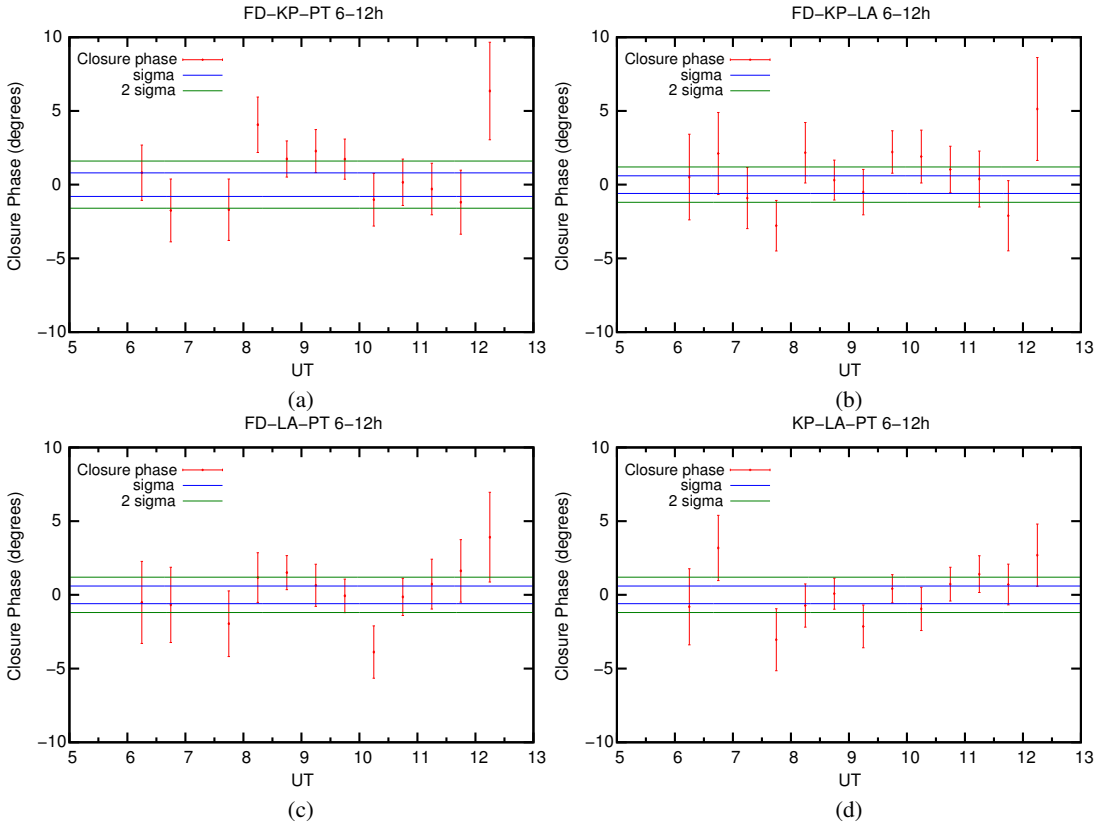

Figure 7.8: Closure Phases and standard deviation levels for all closure triangles of Sgr A* in LCP on May 17 6-12 h UT (altered from Rauch et al. (2016)). (a) FD-KP-PT, (b) FD-KP-LA, (c) FD-LA-PT, (d) KP-LA-PT. All phases are plotted with the standard errors provided by DIFMAP.

Time		FD-KP-LA	FD-KP-PT	FD-LA-PT	KP-LA-PT	Sample mean
8-12 (May 16, 2012)	LCP:	$(0.2 \pm 0.5)°$	$(-0.3 \pm 0.6)°$	$(-0.6 \pm 0.4)°$	$(0.0 \pm 0.4)°$	$(0.2 \pm 0.3)°$
	RCP:	$(-2.0 \pm 1.5)°$	$(-3.4 \pm 1.1)°$	$(-1.2 \pm 0.8)°$	$(0.2 \pm 0.6)°$	$(-1.6 \pm 0.8)°$
6-12 (May 17, 2012)	LCP:	$(0.7 \pm 0.6)°$	$(0.9 \pm 0.8)°$	$(0.2 \pm 0.6)°$	$(0.1 \pm 0.6)°$	$(0.5 \pm 0.2)°$
	RCP:	$(0.1 \pm 0.7)°$	$(0.1 \pm 0.7)°$	$(-0.1 \pm 0.5)°$	$(-0.2 \pm 0.3)°$	$(0.0 \pm 0.1)°$
two hour map:						
8-10 (May 17. 2012)	LCP:	$(0.6 \pm 1.2)°$	$(1.9 \pm 1.1)°$	$(0.2 \pm 0.8)°$	$(-1.1 \pm 0.8)°$	$(0.4 \pm 0.7)°$
	RCP:	$(-0.8 \pm 0.9)°$	$(-1.1 \pm 0.3)°$	$(0.0 \pm 0.3)°$	$(0.3 \pm 0.8)°$	$(0.4 \pm 0.4)°$

Table 7.3: Closure phase values of Sgr A* for all closure triangles on May 16 and 17 (taken from Rauch et al. (2016)).

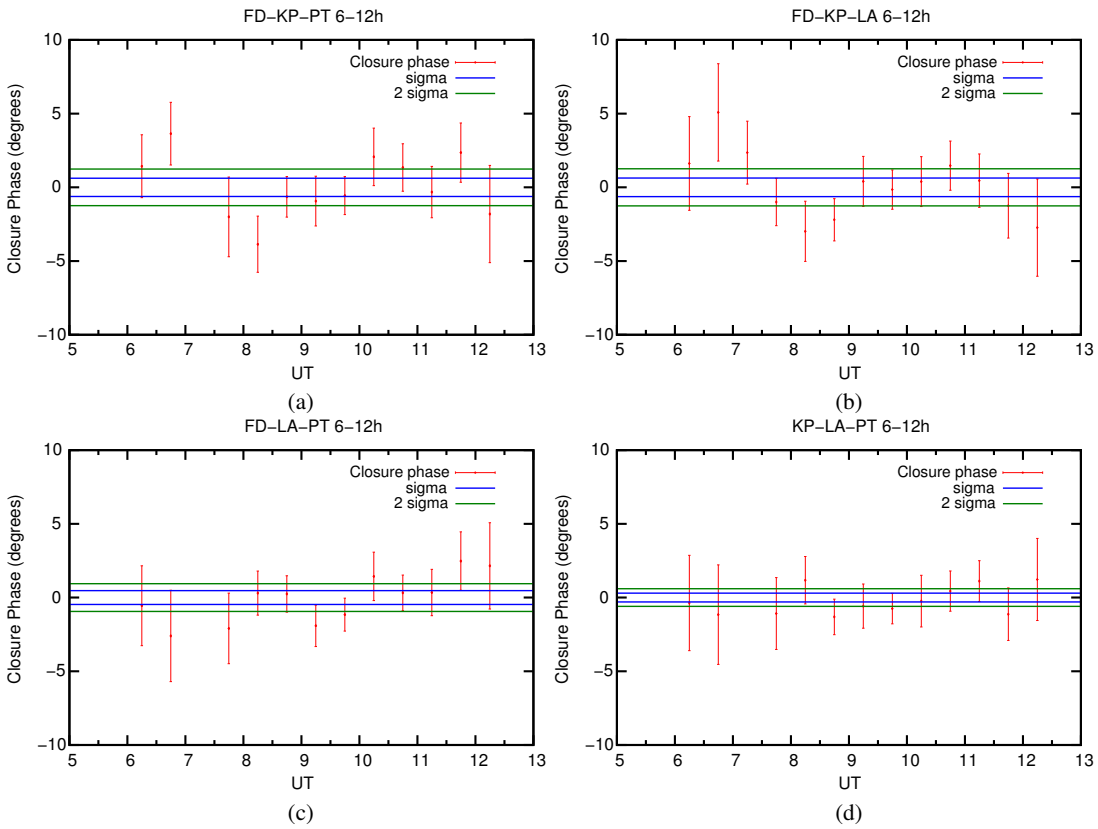

Figure 7.9: Closure Phases and standard deviation levels for all closure triangles of Sgr A* in RCP on May 17 6-12 h UT. (a) FD-KP-PT, (b) FD-KP-LA, (c) FD-LA-PT, (d) KP-LA-PT. All phases are plotted with the standard errors provided by DIFMAP.

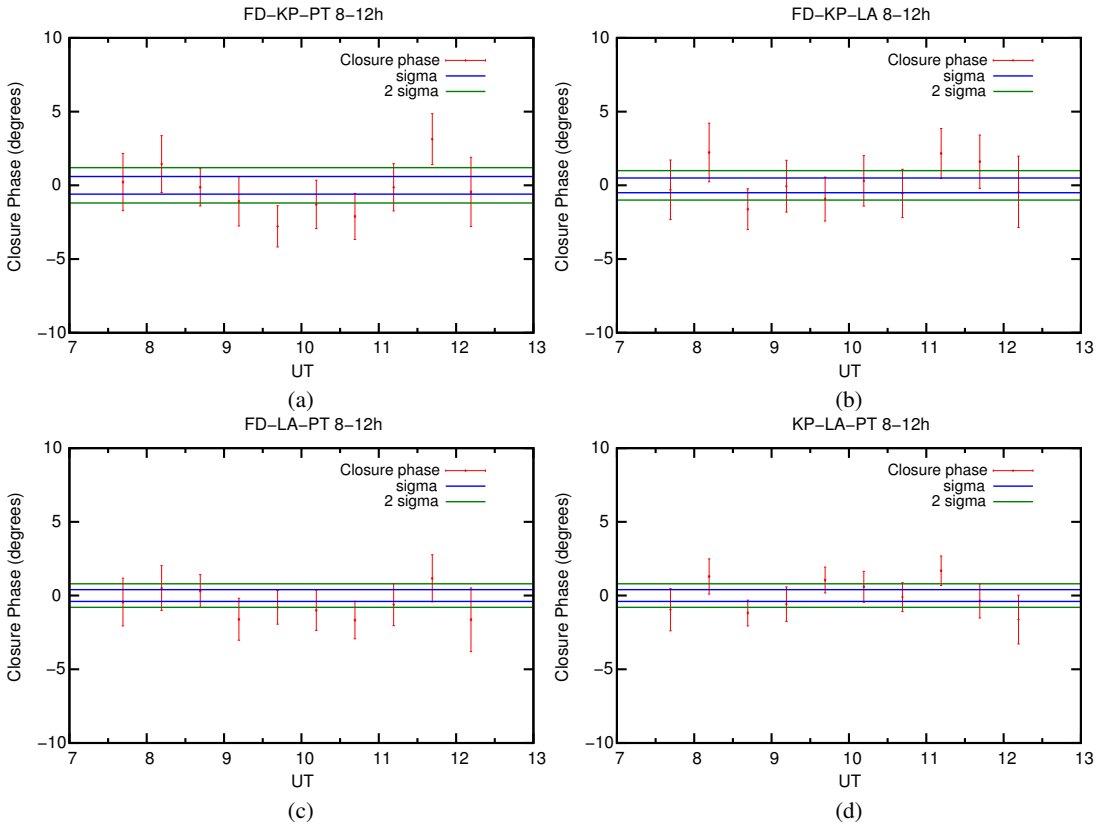

Figure 7.10: Closure Phases and standard deviation levels for all closure triangles of Sgr A* in LCP on May 16 8-12 h UT. (a) FD-KP-PT, (b) FD-KP-LA, (c) FD-LA-PT, (d) KP-LA-PT. All phases are plotted with the standard errors provided by DIFMAP.

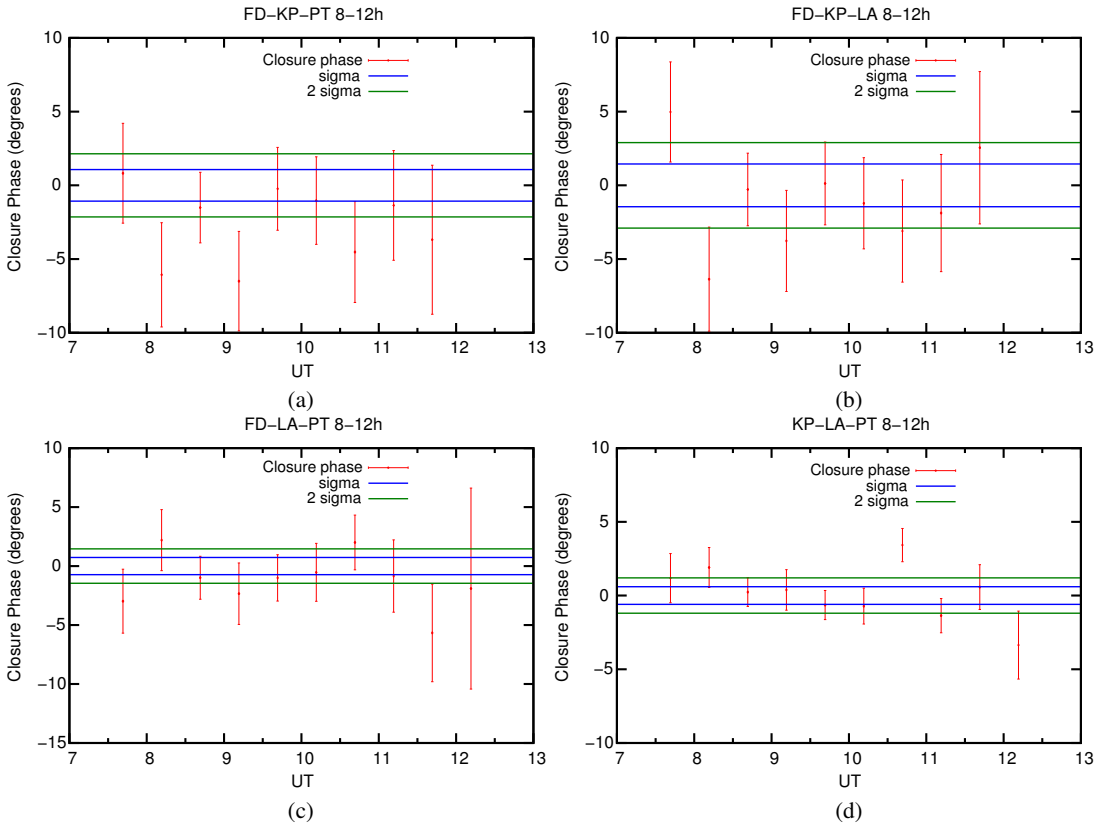

Figure 7.11: Closure Phases and standard deviation levels for all closure triangles of Sgr A* in RCP on May 16 8-12 h UT. (a) FD-KP-PT, (b) FD-KP-LA, (c) FD-LA-PT, (d) KP-LA-PT. All phases are plotted with the standard errors provided by DIFMAP.

tested.

7.2.1.1 Closure phase simulation

A useful tool to test this indication of a non-point like structure is to generate artificial data sets. This task has been performed by the Caltech VLBI analysis program FAKE. FAKE offers routines to define a telescope array and an input model, to which artificial noise is added. The noise can be applied in several ways, such as a simple additive Gaussian noise value added in a random manner defined by a SEED parameter. A more realistic procedure is defining the noise by Tsys, station diameters, as well as station and pointing efficiencies. This program can only deal with single polarization, which is no restriction in the case of the presented work, since only LCP values are considered, in order to circumvent the possibility of additional errors due to the afore mentioned quality problems of this data set between individual polarizations.

Several data sets, covering the period of the most significant asymmetry of Sgr A* on May 17 8-10 h UT, have been simulated, by changing the parameters, comparable to the presented measurement campaign, within justifiable limits. The results of these simulations are summarized in Tab. 7.4. The effect of several input models has been simulated, in order to determine the closure phases such a source structure would produce. The two component model, derived from the previously mentioned circular model fit (central component: 1.55 Jy, secondary component: 0.02 Jy at 1.5 mas under 140°), served as a first input model. This model was altered by changing the position of the secondary component to be at 0.7 mas, 0.3 mas and, finally, a single central component.

In addition to these simulations, based on the most realistic application of noise, derived from the afore mentioned station parameters (T_{sys}, diameter, efficiencies), several data sets have been simulated by adding different amplitudes of Gaussian noise, as well as a perfect simulation, free of any noise. The generated closure phase errors appeared to have much higher errors, ranging from 0.8 to 6.7, than those of the real data set. All closure phases of these simulations are zero within their error limits. Only the 'perfect' simulation (visibilities without uncertainties) was capable of producing comparable noise levels and shows low closure phase values ranging from 1.35 to 0.08, that exceed three sigma and thus, showing the effect of a two component model. This shows, that such a weak secondary component is easily hidden within the noise levels and only careful investigation can reveal such a structure. The simulation of a single central component also excludes the different (u, v)-coverage during 8-10 UT as a possible cause for a secondary component.

In order to further analyze the behavior of noise application used by FAKE, different SEED values have been applied. This parameter controls the random number generator of this algorithm and, thus, alters the effects of the applied noise values. The resulting closure phases differ by by ∼10° for each closure triangle depending on this SEED value. This difference has to be considered as an error limit for testing closure phase of the defined observing setup. The real data set shows deviations from zero in the order of ∼5° and therefore, these simulations have to be taken carefully into account.

Models:	FD-KP-LA	FD-KP-PT	FD-LA-PT	KP-LA-PT	Sample mean
Radius = 1.5 mas	2.3±5.5	-2.0±2.7	2.7±4.6	-1.6±2.0	0.4±1.3
Radius = 0.7 mas	1.2±5.5	-2.8±2.7	2.4±4.7	-1.6±2.0	-0.2±1.3
Radius = 0.3 mas	1.0±5.5	-2.9±2.7	2.3±4.6	-1.6±2.0	-0.3±1.2
Single component	2.7±2.0	-2.5±1.6	2.5±0.8	-2.7±1.7	0±1.6
Errors:					
Perfect	1.35±0.09	1.00±0.06	-0.44±0.04	0.08±0.01	0.7±0.3
ERRADD = 0.02	2.4±5.6	-1.6±2.5	2.5±4.6	-1.5±1.8	0.5±1.2
ERRADD = 0.01	2.5±5.7	-1.5±2.5	2.5±4.6	-1.5±1.7	0.5±1.2
ERRADD = 0.005	2.5±5.7	-1.5±2.5	2.4±4.6	-1.5±1.7	0.5±1.2
SEED-parameters:					
SEED = 3456757	2.4±5.5	-2.0±2.7	2.8±4.6	-1.6±2.0	0.4±1.3
SEED = 3000000	-1.2±4.6	1.8±1.6	-3.9±3.3	-0.9±5.4	-1.1±1.2
SEED = 1278562	8.6±1.9	1.9±2.4	-0.4±3.8	-7.2±6.7	0.7±3.3

Table 7.4: Simulated closure phase values of Sgr A* for all closure triangles on May 17 8-10 h UT (taken from Rauch et al. (2016)).

Despite this boundary condition, it can be said that a secondary component, separated by 1.5 mas at 140°, will have the most significant effect on triangles, with an axis of maximum resolution close to this angle. The axis of the closure triangles, defined by the elliptical beam, are 97° (FD-KP-LA), 101° (FD-KP-PT), 125° (FD-LA-PT) and 65° (KP-LA-PT). Therefore, the effect of a secondary component at an angle of 140°, should be stronger on the former three triangles than on KP-LA-PT. This trend is well reproduced by the perfect simulation, but the simulations also show that this can change significantly by the chosen SEED value. All simulations offer the highest closure phase values to be present at one of these three favored triangles, but a simulated SEED value was also capable of producing a value of 7.2° for KP-LA-PT, which is the second highest within this simulation, showing, that noise can significantly alter this trend. This is also the case for the real data set, which offers the second highest mean closure phase for KP-LA-PT and the highest value of $(1.9 \pm 1.1)°$ (LCP) and $(-1.1 \pm 0.3)°$ (RCP) for FD-KP-PT.

The given boundary conditions of these simulations do not allow to put hard constraints on the mapped two component source morphology, but it shows, that such a source structure is capable of producing the observed closure phase values, under certain noise conditions. Together with the consistent deviation of phases present in LCP and RCP this provides another indication of an asymmetric structure of Sgr A* during its flaring states.

7.2.2 Size measurements

Additional information can be gained by further analyzing the circular models used to generate the maps shown in Fig. 7.3. The best fitting models favor a two component structure for Sgr A* on May 17 8-10 h UT, shortly before the flare described in section 7.2 reaches its peak value. A possible change of the source structure or FWHM of the emission region would point towards an adiabatically expanding feature as described in chapter 3.4.

The modelfit algorithm of DIFMAP will change the free parameters of the input model in such a way, that the final model will be fit according to the fluxes of the map. Thus, an observed extended source will be modeled by larger components. For this analysis, the secondary component of 8-10 UT has been excluded and only the central component was considered. The major axis sizes of all central components found for the two hour model fits are plotted in Fig. 7.12. The plotted size angles are observed sizes, which are still scatter broadened and have to be corrected by an assumed power law of this effect (see Sect. 5.3.1). Since the exact exponent of this power law is still uncertain and it breaks down at the observing frequency of 43 GHz, the size measurements have not been corrected for this effect. This still yields a relative size measurement of all two hr data bins with respect to each other. Such a correction will also only lower these sizes by a constant factor, which will not change the observed trend.

The size error amounts to 0.08 mas and was derived from different model results of repeatedly performed model fitting, that reproduced the trend, but showed slightly different major axis sizes. The error in time corresponds to the two-hour binning of the maps. Sgr A* shows size changes, which appear to be simultaneous to the change of its total flux shown in Fig. 7.1. The initially observed size angle of 0.68 mas for the model fitted to the visibilities of 6-8 h UT rises to a peak size of 0.72 mas on 8-10 h UT and then drops slightly to 0.71 mas, which are equal within their error limits. This trend is also found for the flux values, which is another hint towards a connection between size changes and changes of the total intrinsic source flux. This indicates that the observed flare is accompanied by a structural change, as it has been expected by the proceeding closure phase analysis in section 7.2.1. While the errors do not allow for any statements about a significant change of the source size, this is another test pointing consistently towards a change of the FWHM size of Sgr A* during phases of higher flux levels.

7.2.3 Radial plot

As shown in Rauch et al. (2016), a radial plot of the (u, v)-data is a way of showing the visibility amplitudes of a dataset as a function of their baselines. Short baselines contain the total amount of source flux, while longer baselines offer smaller beams, that only cover a fraction of the source and therefore, only partially measure the flux values. This results in a typical form of a Gaussian with higher flux values towards the shortest baselines. In case of a complex, multiple component source, each component will appear as a secondary area of data points, shifted according to their amplitudes. These secondary areas appear on all scales at which their dimension can be detected

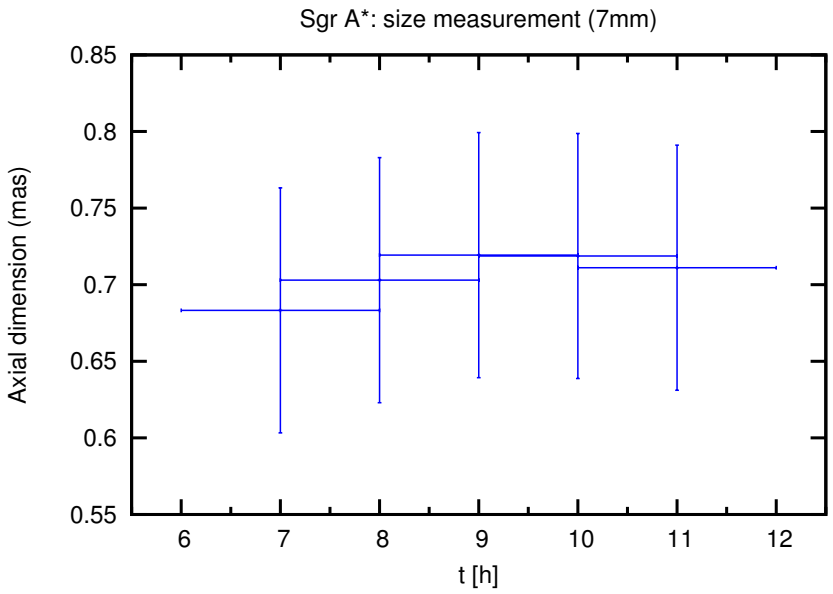

Figure 7.12: Angular size of Sgr A* in mas derived from central circular model fit shown in Fig. 7.3 as a function of time. For the time range of 8-10 h UT only the central component has been considered.

at the resolution defined by the baselines. This makes this form of displaying the data another reliable test of accurately detected components. The corresponding radial plot of the presented data set is shown in Fig. 7.13. It illustrates the models derived for the three maps of highest flare activity and change in source structure as 8-10 h (red), 9-11 h (orange) and 10-12 h (blue). The models of 8-10 h and 9-11 h clearly show a secondary feature for (u, v)-ranges between 40 - 80 Mλ, which is consistent with the maps shown in Fig. 7.2. As indicated by these maps, the radial plot at 10-12 h does not contain a strong secondary feature. This fits into the previously described tests of the source structure of Sgr A* and further improves the robustness of a secondary component to be present during flaring states.

7.2.4 Three day map analysis

Combining the data of all three days into a single six hour data set offers another possibility of testing of the true existence of an extended structure of Sgr A*. The map shown in Fig. 7.14 was generated in the same way as the previously shown maps of Sgr A*. The resulting clean image has no indication of a deviation from a point source. The determined symmetric model can serve as a tracer for differences form its point-like structure by convolving this model with different time ranges, especially those of detected two component source structures. The resulting noise of any non-point like structure will, if it is convolved with a point model, result in higher residual noise levels. Therefore, the three day data was split into two-hour bins according to the maps in Fig. 7.2 and convolved with the model of the three day map. The residual noise has

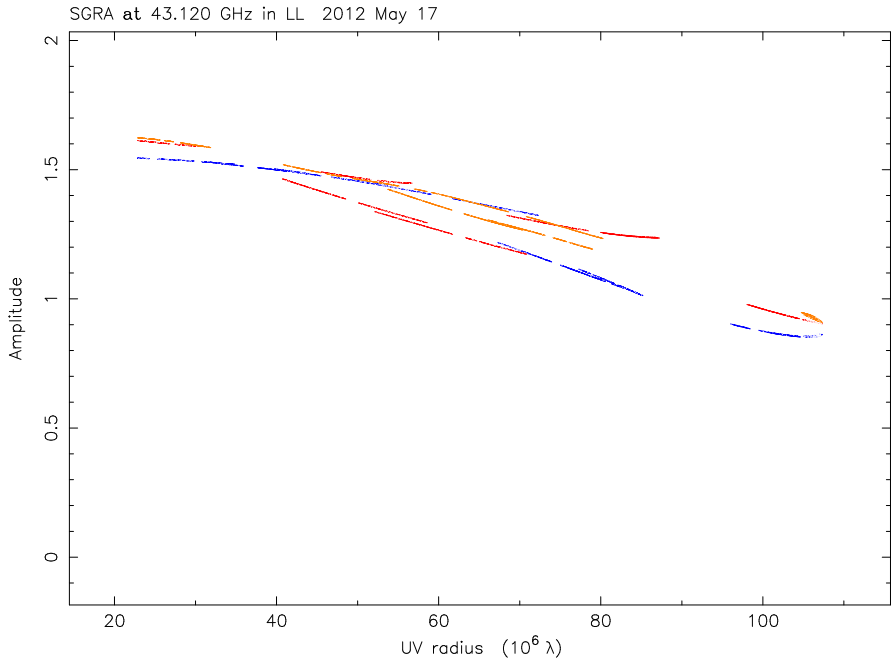

Figure 7.13: Radial plot of Sgr A* during its period of strongest flaring activity on May 17 2012. The colors of the fitted models correspond to the time ranges 8-10 h UT (red), 9-11 h UT (orange) and 10-12 h UT (blue) (taken from Rauch et al. (2016)).

been determined by measuring the fluxes at areas outside of telescopes beam. These areas only contain thermal noise flux without any sources and are, thus, a reliable noise measure. The noise values are summarized in Tab. 7.5.

Time UT in [h]	RMS noise [mJy]		
	3 day map	May 16	May 17
06-08	3.9		2.8
07-09	1.4		3.6
08-10	1.5	2.2 (no OV) 2.5 (OV)	2.1
09-11	1.3		1.64
10-12	1.9		8.3

Table 7.5: Summary of residual noise values, if convolved with the 3 day delta component model on May 16 and 17.

Higher noise levels at start and end of the observations are expected to be caused by the lower elevation of Sgr A* at these times and a lower data density, caused by changing starting times of the individual observations of each date. Despite this behavior, the two hour data bins of the three day map provide the highest noise during the time range of 8-10 h. This is consistent with the detected change in morphology during this date. This detection is remarkable, since the effects of a secondary component within approximately 1/3 of the data is much lower in a combined three day map, compared to a single day data set, because 2/3 of the data will resemble a point source. But since

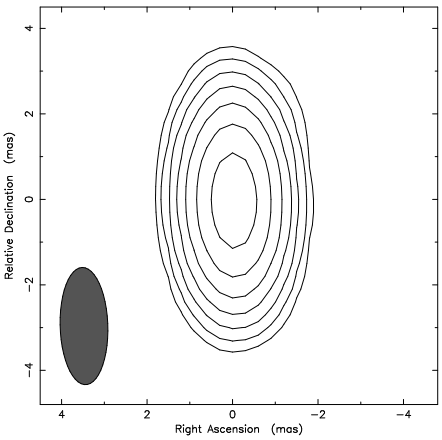

Figure 7.14: Three-day map of Sgr A* (Fourier deconvolution of all observed visibilities).

the noise difference is in the order of 10%, this still lies within the error limits.

Further testing of this trend was performed by comparing the noise levels of the two hour maps on May 17 in the same manner (see Tab. 7.5). For comparison the noise level of the two hour bin on May 16 8-10 UT has been plotted for the same array setup as on May 17, as well as including the additionally available station OV. May 18 has a completely different array setup and is therefore, not useful for this analysis. While May 17 offers an overall lower noise level compared to May 16, due to its higher data quality, the previous trend of higher values during 8-10 h of the three day map could not be reproduced. The noise levels of May 16 (no OV) and May 17 are in the same range and show now significant deviation from each other. As a consequence the noise analysis does allow for any hard conclusions beyond another indication towards the true detection of a secondary component at the position of Sgr A*.

7.2.5 Residual map symmetry analysis

Further insights on the reliability of the detected change in source structure can be gained by looking at the residual map of Sgr A* during the time of a possible deviation from a point source. The residual map of a point source will show only point symmetric features and any deviation from this symmetry will point towards a non-point like structure in the Fourier space.

It is reasonable to assume that two areas mirrored at the center of the map will contain the same amount of flux in the case of a point symmetric source structure. The residual flux map of May 17 8-10 h UT is shown in Fig. 7.15. To measure the fluxes at two diametrical points, an area of 0.75×0.75 mas at the position of the detected secondary component has been defined and mirrored at the map center. The flux contained in these areas has then been determined by adding the flux values of each pixel. Comparison of the fluxes contained in these two areas shows an excessive value of 0.24 Jy towards the south-east of Sgr A*. The error of this analysis has been determined by shifting the central component at pixel scales and amounts to 0.4 Jy. This error does not exclude the possibility of a secondary component, but does also

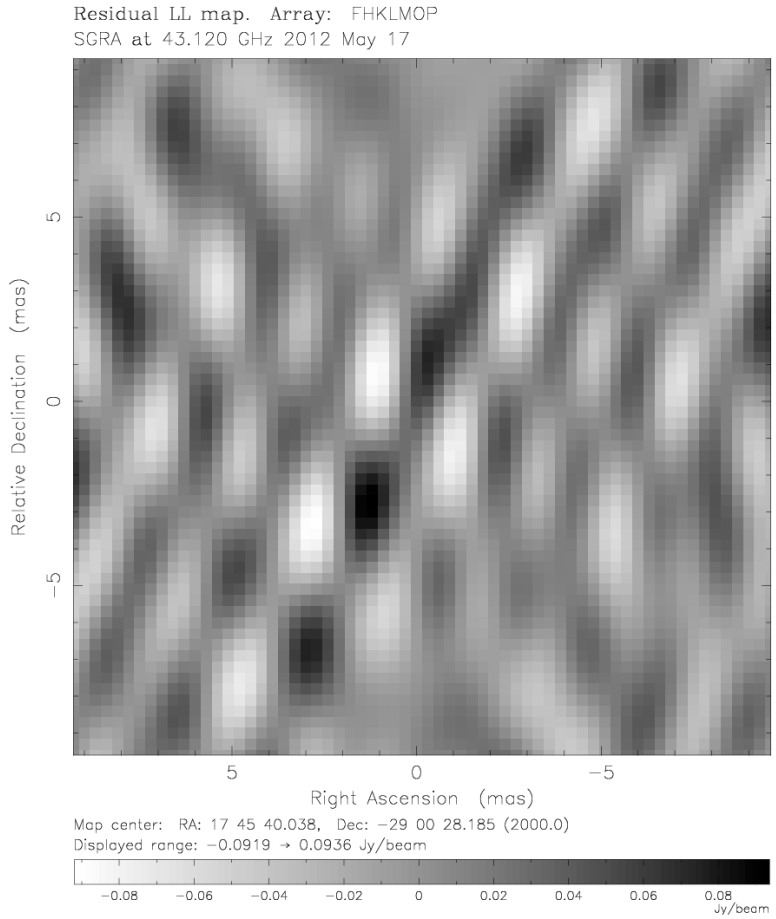

Figure 7.15: Residual map of Sgr A* on May 17 8-10 h UT showing a slight indication of asymmetry along the NW/SE axis. The scale shows higher flux values as darker areas.

not allow us to put hard constraints on it either and provides another indication of a non-point like structure of Sgr A* obscured within the error levels.

7.3 Phase referencing

In case of sources fainter than the detection limit required for self-calibration, the missing information of phase errors can still be obtained by observing nearby calibrator sources of well known and accurately predictable visibilities. In many cases quasars serve this purpose because of their steady position and simple source structure. According to Middelberg & Bach (2008), it is reasonable to assume that the science target and the reference sources are affected by similar phase errors, if they are within the isoplanatic patch (see Sect. 5.3.11), which amounts to a few degrees at 5 GHz. Another value that has to be considered is the timescale of the affecting errors. The assumption of similarity for both sources is justified for the slow regime of error variations such as clock or array geometry errors. In case of fast varying atmospheric deviations this is

only true if the switching time between science target and calibrator is short enough to be smaller than the time scale on which the atmospheric errors change significantly. This limiting time scale within which the similarity assumption is justified is called atmospheric coherence time and forms together with the isoplanatic patch the two boundary conditions for phase referencing.

Another advantage, besides being possible to observe very weak sources, is its performance in determining their relative positions at very high accuracy. The phase difference between a spatially constant calibrator source (e.g. quasar) and the science target yields information about their separation and can, therefore, be used to measure relative positions. If two of such calibrators are used, then the relative position derived from their phase differences can be used to accurately position the science target in the two dimensional observing plane with respect to the calibrators.

The common approach would use two constant extragalactic sources as phase reference centers and determine the relative phase to the science target. Because of the small number of available sources, the best candidates in the vicinity of Sgr A* are J1745−283 and J1748−291. These quasars are very weak which made it necessary to change the usual method in a way, that Sgr A* itself serves as the phase center for the phase referencing analysis. This approach will not change the result, since the determined relative position remains the same and the triangle of these sources can be used to accurately determine the position of Sgr A*.

The generated delta component maps of Sgr A*, covering a time range of two hours, have been used as a phase reference. The two extragalactic sources J1745−283 and J1748−291 are then fringe fitted to the reference center of these maps. The resulting image centered on Sgr A* contains the detected reference sources at their positions relative to it. This method only requires to achieve a detectable flux excess above the noise limit to determine the relative phase, which is the reason for phase referencing being capable of determining relative positions with respect to really faint sources.

Despite these capabilities, the reference sources offer very weak peak flux values (J1745−283: 0.13 Jy/beam; J1748−291: 0.09 Jy/beam) and are subject to all previously mentioned data deteriorating effects, which only made it possible to reliably detect them during the midst 4 hours ranging from 7-11 h UT on May 17. The determined flux peak positions are summarized in Tab. 7.6. All positions have been derived from the highest flux pixels found at the expected positions of J1745−283 and J1748−291. Therefore, the positional errors are ±1 pixel or 0.3 mas, based on the cell size of the Sgr A* maps.

Even though it was possible to determine peak flux positions for both reference sources, the values show a significant deviation from the other detections of 1745−283 during the time range of 10-12 h UT on May 17 and of 1748−291 during 7-9 h UT, as well as 10-12 h UT. This indicates that these points are possible faulty detections of excessive noise. The remaining positions of 1745−283 during 7-11 h UT and of 1748−291 during 8-11 h UT are more concise, and have been used to determine a mean relative position with respect to Sgr A* for these sources of (RA: 13.4 ± 0.3, Dec: 24 ± 0.3) mas for J1745−283 and (RA: 14.1 ± 0.3, Dec: 20.0 ± 0.3) mas for J1748−291. The values deviate from this mean value by more than 0.3 mas, which is much higher

than the expected accuracy of phase referencing at 43 GHz, but is still within two sigma of the high error limits provided by the coarse binning of these maps. Together with the low flux values of these sources, being slightly above the noise levels, these detections are suspicious and, thus, the position of Sgr A* is considered to remain constant during its flaring phase.

The large amount of noise could be lowered by accurately determining the atmospheric errors and carefully calibrating the data according to these corrections. This goal can be achieved by including geodetic blocks into the observing plan, that observe several sources at different elevations and areas across the sky to determine a more accurate atmospheric model. A geodetic block was not observed for the current data of BE061. Follow-up observations (BR201) of this measurement campaign, including geodetic blocks, have been performed in the beginning of Oct 2014 and will offer the possibility of a more accurate phase referencing analysis. For the presented data of BE061 the position of Sgr A* on the basis of phase referencing analysis has to be considered constant within the given error limits.

time	1745−283		1748−291	
UT on May 17 in [h]	R. A. [mas]	Dec. [mas]	R. A. [mas]	Dec. [mas]
06-08	13.2	24.3	-	-
07-09	13.2	24.0	14.7	19.5
08-10	13.2	24.3	14.1	19.8
09-11	13.5	23.7	14.1	20.1
10-12	13.5	23.1	14.1	20.4

Table 7.6: Summary of phase referencing positions of Sgr A* on May 17. The error amounts to 0.3 mas for all measurements.

The complete set of presented robustness tests of a secondary component shows many indications in the range of one to two sigma. Since all test consistently point towards the existence of this weak component, a random effect seems unlikely but can not be excluded completely. Together with the flux analysis of section 7.1 that shows a flare of Sgr A*, well above its quiescent emission, detected by all available individual methods of flux estimation, this secondary component appears shortly before the flare peaks at 9-11 h UT. The statements that such a source structure implies are discussed in the following chapter.

Chapter 8

Discussion

This chapter discusses the results described in chapter 7 in detail and will provide statements that can be gained from the detected flare of Sgr A*, its time delay and the possibly existing secondary component of Sgr A* during its flaring state.

8.1 Time delay

As described in section 3.4, Sgr A* shows flaring activity ranging from radio to NIR and X-ray wavelengths. Different frequencies arise from different radial areas within this object (see Fig. 8.1) and, thus, simultaneous multi-frequency observations provide an appropriate method to investigate the spatial evolution of an event at different scales. The provided time delay between the observing frequencies corresponds to the travel velocity an event needs to reach the different mapped regions of an opaque source and, therefore, offers another characteristic to investigate the underlying physical processes of flaring black holes.

Since it is possible that flares observed at different frequencies are not causally connected, the following velocity analysis will show that the reported delay between NIR and 7 mm of this thesis stays at subluminal speeds and, therefore, the peak fluxes can be connected to the same event. The following calculation uses the notation of Rauch et al. (2016). In order to derive the traveling velocity, the reported time delay of (4.5 ± 0.5) h is used, which is in good agreement with the values of ≥ 5.25 hrs reported by Yusef-Zadeh et al. (2009). According to Markoff et al. (2007), a jet feature would have an appreciable inclination (θ) towards the line of sight, which we assume to be 80°. Even though other values are possible, changing this parameter does not alter the results significantly and is, therefore, reasonable. The corresponding traveling velocity (v_t) of an expelled secondary component at 1.5 mas can then be calculated by

$$v_\mathrm{t} = (0.4 \pm 0.2)\mathrm{mas\,h^{-1}} = (1.3 \pm 0.7) \cdot 10^8\,\mathrm{m\,s^{-1}} = (0.4 \pm 0.3)\,\mathrm{c}. \tag{8.1}$$

The real gas velocity (v_g) has to be corrected for superluminal effects ($\beta = v/c$) and can be described as

$$v_\mathrm{g} = \frac{v_\mathrm{t}}{\sin\theta - \beta\cos\theta} = (0.4 \pm 0.3)\,\mathrm{c}. \tag{8.2}$$

As reported by the MHD model of Yuan et al. (2009), the gas can reach velocities of 0.8 c above the accretion disc shortly after it has been expelled. The derived velocity of the presented data set is well below this limit and is, therefore, an indication of a connection between the NIR and 7 mm flare. Other cooling processes than adiabatic

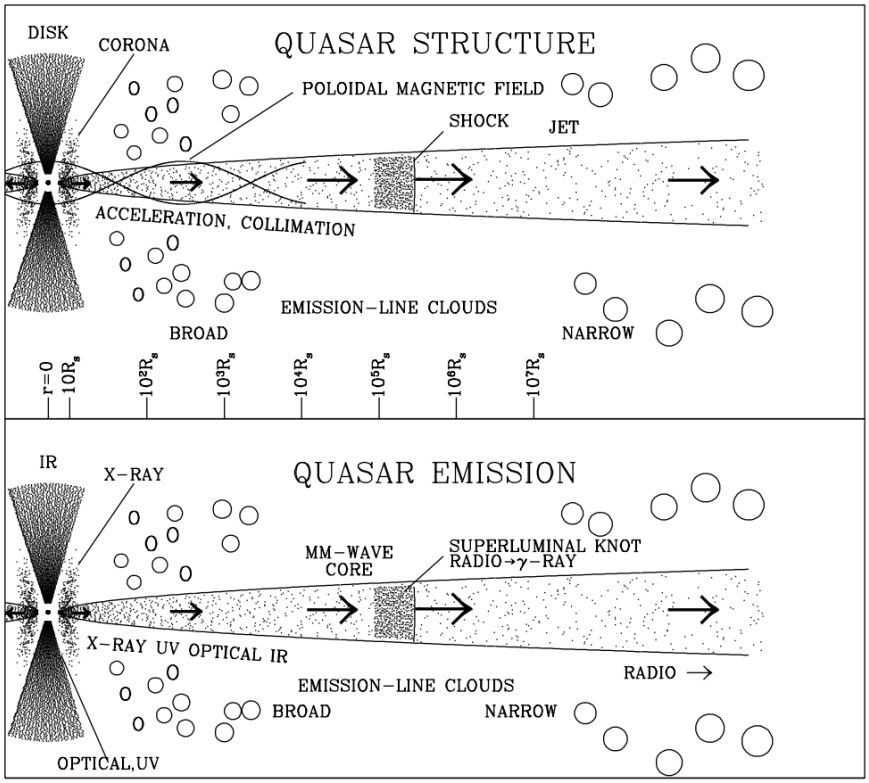

Figure 8.1: Illustration of a jet, showing the regions observable by different wavelengths. Even though this illustration shows a quasar, different frequencies will equally map different radial regions of the environment of Sgr A*. Source: (Marscher, 2005)

expansion of jets are possible, but the consistency of the reported time delay with the values provided by the literature are a strong indication of a connection between these events, which provides another hint towards a possibly present jet feature.

Simultaneous multi-frequency observations ranging from radio to X-rays are of most interest to gain a radial image of the environment of Sgr A*. After the first evidence of correlated multi-frequency flares has been detected by Zhao et al. (2004) and Eckart et al. (2004) at radio and NIR/X-ray wavelengths, follow up observations have been performed simultaneously at NIR/sub-mm/X-ray frequencies with the goal of investigating the underlying physical processes that lead to these flares. Eckart et al. (2004) report of a comparably weak X-ray flare which triggered the NIR observations. The authors detected a fading NIR flare which overlapped with the decreasing part of the X-ray flare. Furthermore, Eckart et al. (2006b) report of a moderate X-ray flare that occurred simultaneously to five NIR flux excesses. The X-ray flare was well covered by a synchronous NIR event with an upper limit for the time lag of ≤ 10 minutes, caused mainly by the required bin width of the X-ray data. Cross-correlation of all flares in 2003 and 2004 at different wavelengths show a time lag smaller than 10 minutes and, therefore, these events are considered to be simultaneous. This short time lag points towards a synchronous evolution of the same population of electrons which supports their previous statement in Eckart et al. (2004). Observations have revealed that each X-ray flare is accompanied by a NIR flare with almost zero time lag, but not vice versa (Eckart et al., 2004, 2006b, 2008a; Bélanger et al., 2005; Hornstein et al., 2007). The short duration of these flares indicate, that the emission is very likely to originate from a compact source.

Follow-up observations reported on several related NIR and sub-mm flares (e.g., Eckart et al. (2008a,c); Yusef-Zadeh et al. (2009)). Eckart et al. (2008a,c) find a time lag of 1.5 ± 0.5 h between 345 GHz and NIR frequencies. A typical delay of $\sim$100 min for a NIR/X-ray flare to reach the sub-mm/mm (1.3 mm) area has also been found by several other authors (Meyer et al., 2008b; Marrone et al., 2008; Yusef-Zadeh et al., 2008). At radio to sub-mm wavelengths the variability of Sgr A* changes on timescales ranging from hours to years (Zhao et al., 2003; Herrnstein et al., 2004). This radio variation is considered to be caused partly by interstellar scintillation. The causal connection to X-ray frequencies is still subject to discussion while there are claims of the brightest observed X-ray flare being connected to flux density variations at mm- and cm-wavelengths (Zhao et al., 2004; Mauerhan et al., 2005).

A summary of the time delays found by (Eckart et al., 2006b; Marrone et al., 2008; Meyer et al., 2008b; Yusef-Zadeh et al., 2006b, 2008, 2009, 2012; Miyazaki et al., 2013; Brinkerink et al., 2015) and the reported delay of (4.5 ± 0.5) hrs of this thesis are shown in Tab. 8.1. We excluded the arguable derived time delay of 20 ± 5 min of Marrone et al. (2008) and use 140 min instead, as suggested by Brinkerink et al. (2015). Zhao et al. (2004) report a time delay between X-ray to 7 mm data on observations that started 13.5 hr after the X-ray event. Because of this huge separation of the observations it is possible that they might have missed a 7 mm flare, that is delayed with respect to the X-ray data by about 5 hrs, as suggested by Yusef-Zadeh et al. (2009) and the time delay reported in this thesis. Therefore, this measurement has been excluded from the

Band	Time Delay [min]								
Date:	2004 Jul 6-7	2005 Feb 10	2005 Apr 6	2005 Jul 30-31	2006 Feb 10	2006 Jul 16-17	2007 Apr 1-5	2008 Jun 2-3	2012 May 17
-ray (2-8keV) to NIR (1.7 μm, 2.2 μm, 3.8 μm)	$8.0^{+10.0}_{-10.1}$ $8.0^{+20.2}_{-17.9}$ ≤ 10		$30^{+7}_{-6.5}$				$0.5^{+7}_{-6.5}$		
X-ray (2-8keV) to 850 μm						110 ± 17 96 ± 14			
NIR (1.7 μm, 2.2 μm, 3.8 μm) to 850μm	100							90 ± 30	
X-ray (2-8keV) to 1.3 mm				97 ± 17					
NIR (1.7 μm, 2.2 μm, 3.8 μm) to 1.3 mm				140			$158.4^{+30}_{-40.2}$		
450 μm to 1.3 mm (230 GHz)							$14.4^{+67.2}_{-17.4}$ $79.2^{+19.8}_{-40.2}$		
850 μm to 1.3 mm						2 ± 12			
2.2 mm (134 GHz) to 2.05 mm (146 GHz)							$3^{+3.4}_{-8}$		
2.95 mm (102 GHz) to 3.33 mm (90 GHz)		3	1.7 ± 0.6						
850 μm to 7 mm						>75			
3 mm to 7 mm							$61.2^{9.6}_{18.6}$		
850 μm to 13 mm						65^{+10}_{-23} 45 ± 30			
7 mm to 13 mm		30 ± 12 28 ± 9		30 ± 10	20 ± 6	20.4 ± 6.8			
X-ray (2-8keV) to 7 mm							$319.6^{+9.4}_{-7.6}$		
NIR (1.7 μm, 2.2 μm, 3.8 μm) to 7 mm									270 ± 30

Table 8.1: Summary of time delays at different frequencies for Sgr A*.

following discussion.

The data shows that shorter wavelengths always lead the longer ones. Together with the fact, that shorter wavelength measure smaller regions, which are closer to the core, the relation between flares implies, that these burst events propagate from smaller to larger radii. The apparent connection between all different radial sizes indicates, that all flares seem to be originating from a common event. Therefore, it is feasible to assume that the whole set of radiation from a single flare propagates the same medium and will be observable at different wavelengths with different time delays. If the intrinsic scales of these regions (ϕ_i) and the time delay (δt) are known, then, as described in Falcke et al. (2009), a velocity for the intrinsic radial patch can be determined by:

$$v = \frac{\phi_1 - \phi_2}{\delta t}. \tag{8.3}$$

Falcke et al. (2009) derived a wavelength dependent function for the intrinsic size of Sgr A* by subtracting the scattering law, given by

$$\phi_{\text{sca}} = (1.36 \pm 0.02)\,\text{mas} \times (\lambda/\text{cm})^2 \tag{8.4}$$

from the measured major axis sizes at radio wavelengths. The resulting intrinsic source size, considering error weights, was fitted by a power law function, which results in:

$$\phi_{\text{int}} = (0.52 \pm 0.03)\,\text{mas} \times (\lambda/\text{cm})^{1.3\pm0.1}. \tag{8.5}$$

While the velocity in equations 8.1 and 8.2 are derived from the observed apparent source size of the presented data set at 7 mm under the assumption of an expansion of 1.5 mas from the center, it is useful to analyze the intrinsic velocities that are corrected for interstellar scattering. The apparent observable source size is larger than the real

Band	Velocity [c]								
Date	2004 Jul 6-7	2005 Feb 10	2005 Apr 6	2005 Jul 30-31	2006 Feb 10	2006 Jul 16-17	2007 Apr 1-5	2008 Jun 2-3	2012 May 17
X-ray (2-8 keV) to NIR (1.7 μm, 2.2 μm, 3.8 μm)	$(7.6 \times 10^{-5}) \pm 0.00012$ $(7.6 \times 10^{-5})^{+0.0003}_{-0.0002}$ $\geq 6.08 \times 10^{-5}$						$0.0012^{+0.018}_{-0.015}$		
X-ray (2-8 keV) to 850 μm						0.022 ± 0.010 0.015 ± 0.005			
NIR (1.7 μm, 2.2 μm, 3.8 μm) to 850 μm	0.014							0.016 ± 0.007	
X-ray (2-8 keV) to 1.3 mm				0.025 ± 0.007					
NIR (1.7 μm, 2.2 μm, 3.8 μm) to 1.3 mm				0.017 ± 0.007			$0.015^{+0.005}_{-0.006}$		
450 μm to 1.3 mm (230 GHz)							$0.13^{+0.6}_{-0.2}$ $0.023^{+0.010}_{-0.014}$		
850 μm to 1.3 mm						0.5 ± 3.2			
2.2 mm (134 GHz) to 2.05 mm (146 GHz)							$0.14^{+0.4}_{-0.6}$		
2.95 mm (102 GHz) to 3.33 mm (90 GHz)		0.4	0.7 ± 0.9						
850 μm to 7 mm						< 0.3			
3 mm to 7 mm							$0.24^{+0.05}_{-0.08}$		
850 μm to 13 mm						$0.73^{+0.13}_{-0.3}$ 1.0 ± 0.8			
7 mm to 13 mm		0.9 ± 0.4 1.0 ± 0.4		0.9 ± 0.4	1.3 ± 0.5	1.3 ± 0.5			
X-ray (2-8 keV) to 7 mm							$0.068^{+0.006}_{-0.005}$		
NIR (1.7 μm, 2.2 μm, 3.8 μm) to 7 mm									0.08 ± 0.01

Table 8.2: Summary of velocities at different frequencies for Sgr A*.

intrinsic size and, thus, this enlarged emission region leads to higher velocities than they intrinsically occur. Using these equations, it is possible to determine the velocities for the time delays shown in Tab. 8.1. The resulting values are summarized in Tab. 8.2.

The corresponding angular major axis sizes of the shells related to the individual wavelengths as well as the corresponding radial shell sizes covered by each set of multi-wavelength observations are summarized in Tab. 8.3 and Tab. 8.4. A scaled overview of these shells is presented in Fig. 8.2, which shows the radial shell sizes corresponding to the available observing frequencies. The sizes of the innermost shells corresponding to X-ray and NIR wavelengths are smaller than the Schwarzschild radius of Sgr A* ($R_s \approx 0.009$ mas for a mass of $3.6 \times 10^6\, M_\odot$) and are, therefore, considered as the core for this illustration and further analysis. This circumstance arises from the assumed intrinsic size power law in Falcke et al. (2009) which was derived at longer wavelengths. The shells of these frequencies are in nature well above the Schwarzschild radius, but this deviation from their true radial dimension will have little impact on the results. The NIR and X-ray core are the center of this velocity model of the black hole's environment. Because of their small scale the NIR/X-ray shells are assumed to be equal for the following analysis.

In parallel to Falcke et al. (2009), it is useful to assume that the flares observed in the same wavebands encounter equal time delays and can be averaged. Flares on different dates can have different speeds due to their changing flaring properties, as their intensity and accretion flow might have changed. But the fact that the detected time delays of the same region observed on several dates are equal within the given error limits justifies this approach. As a result the expansion speeds also stay within a common range. If such a common velocity is assumed, it is reasonable to derive a mean velocity for each shell covered by the observations listed in Tab. 8.1. The resulting mean values are summarized in Tab. 8.4.

The resulting mean values show subluminal velocities, except for the outermost measurements at 13 mm. Interestingly, values exceeding 0.7 c are only found on the

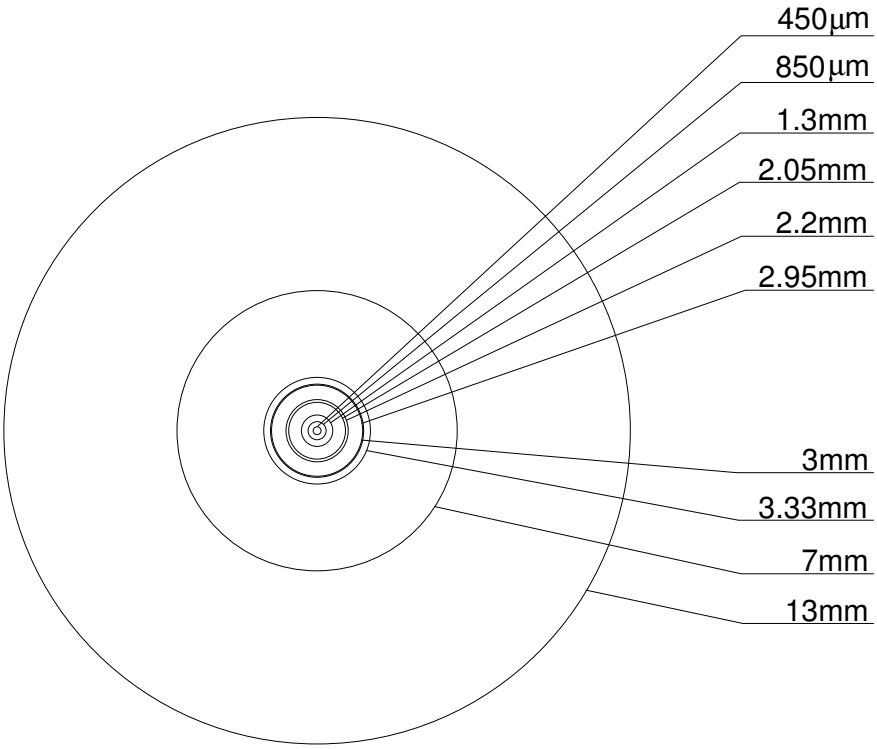

Figure 8.2: Scaled map of the shells spanned by the observations listed in Tab. 8.1.

outer shells defined by the 13 mm intrinsic size. Observations covering the midst areas offer velocities above 0.2 c (850 μm to 1.3 mm, 2.95 mm to 3.33 mm, 850 μm to 7 mm, 3 mm to 7 mm), this indicates that there is an innermost area of very low velocity, which causes the observations covering the whole range of 0 to 0.33 mas (NIR/X-ray to 7 mm) to offer very low velocities. While velocities of the innermost regions are well below 0.1 c, this indicates that the particles of a possibly expanding feature are accelerating at this scales. The time delays reported by Yusef-Zadeh et al. (2009) and this thesis, are also lower than 0.1 c. Since they span over the largest radius around Sgr A* ranging from the apparently low velocity core to the outer higher velocity regime it will offer lower velocities than the speeds of a shell covering only the outermost region, if this acceleration is real. In summary, the data suggests a small low velocity ($\leq$ 0.1 c) core up to 0.021 mas, followed by a medium velocity (0.5 c) shell ranging up to 0.125 mas and an outer high velocity (1 c) area. This indicates that the particles of a possibly expanding feature accelerate towards the outer regions, as it is suggested by jet models.

If we further assume that all flares encounter the same environment, as it has been done by Falcke et al. (2009) for the flares on Feb 10 2005, Feb 10 2006 and July 17 2006, it is possible to relate individual time delays to each other. It has to be kept in mind, that the variety of flaring intensities and durations might offer different properties, like higher accretion rates, which can alter the density of the propagation medium and might lead to different traveling speeds for different flares. In order to derive a radial velocity plot, we have related all measured observations of Tab. 8.1 to the NIR/X-

Band	intrinsic angular size [mas]
X-ray (2-8 keV)	$(7 \pm 12) \times 10^{-11}$
NIR (2.2 μm)	$(9 \pm 8) \times 10^{-6}$
450 μm	0.009 ± 0.003
850 μm	0.021 ± 0.006
1.3 mm	0.37 ± 0.008
2.05 mm	0.066 ± 0.012
2.2 mm	0.073 ± 0.012
2.95 mm	0.106 ± 0.012
3 mm	0.109 ± 0.015
3.33 mm	0.125 ± 0.016
7 mm	0.33 ± 0.03
13 mm	0.73 ± 0.05

Table 8.3: Intrinsic angular size of Sgr A* as a function of the wavelength. Derived according to Falcke et al. (2009).

ray core and interpolated additional time delays by relating their time delays to other measurements. The complete list of the data points acquired in this way is shown in Tab. 8.5. The data at 2.05 mm, 2.2 mm, 2.95 mm and 3.33 mm are excluded due to the lack of time delays relating these regions to the NIR/X-ray core. All NIR observations have been averaged to a common wavelength of 2.2 μm, which is reasonable, since the intrinsic size differences and time delay between these wavelengths are assumed to be small and will not change the result. The plotted time delays as well as velocities as a function of their intrinsic source sizes are shown in figures 8.3 and 8.5. To analyze the crowded wavelength shells below 0.1 mas, the time delay and velocity dependency on the intrinsic size has been plotted on a logarithmic scale as well in figures 8.4 and 8.6. Red points resemble direct measurements, while the single blue point is the time delay reported by this thesis (Rauch et al., 2016) and green points correspond to points of interpolated time delays.

The shown time delay significantly increases over a small radial area up to 0.05 mas and then stays almost constant over the remaining 0.7 mas covered by the data up to 13 mm. This results in velocities that seem to be following a linear or exponential behavior, which is hard to distinguish due to the large range of values at 13 mm. This might arise from the fact that they have been generated from relative measurements to other time lags, which results in high errors and value ranges. Excluding these widely spread 13 mm data and fitting a linear regression function to the data up to 7 mm results in:

$$v(\phi_{\text{int}}) = (0.20 \pm 0.03)\,\text{c} \times (\phi_{\text{int}}/\text{mas}) + (0.01 \pm 0.01)\,\text{c}. \tag{8.6}$$

With Eq. 8.5, this yields:

$$v(\lambda) = (0.10 \pm 0.02)\,\text{c} \times (\lambda/\text{cm})^{1.3\pm0.1} + (0.01 \pm 0.01)\,\text{c}. \tag{8.7}$$

The velocities resemble an acceleration towards the outer shells, as it has been suggested by the unrelated time delays and velocities of Tab. 8.4. As previously stated, it is unclear whether the detected flares and delays encounter the same accretion rates

Bands	relative intrinsic angular shell size [mas]	mean velocity [c]
X-ray (2-8 keV) to NIR (1.7 μm, 2.2 μm, 3.8 μm)	$(9 \pm 8) \times 10^{-6}$	$(5 \pm 5) \times 10^{-4}$
X-ray (2-8 keV) to 850 μm	0.021 ± 0.006	0.019 ± 0.004
NIR (1.7 μm, 2.2 μm, 3.8 μm) to 850μm	0.021 ± 0.006	0.014
X-ray (2-8 keV) to 1.3 mm	0.037 ± 0.006	0.025 ± 0.007
NIR (1.7 μm, 2.2 μm, 3.8 μm) to 1.3 mm	0.036 ± 0.008	0.016 ± 0.001
450 μm to 1.3 mm (230 GHz)	0.027 ± 0.009	0.08 ± 0.06
850 μm to 1.3 mm	0.016 ± 0.010	0.5 ± 4
2.2 mm (134 GHz) to 2.05 mm (146 GHz)	0.006 ± 0.017	$0.14^{+0.4}_{-0.08}$
2.95 mm (102 GHz) to 3.33 mm (90 GHz)	0.02 ± 0.03	0.6 ± 0.2
850 μm to 7 mm	0.31 ± 0.03	≤ 0.3
3 mm to 7 mm	0.22 ± 0.03	$0.24^{+0.05}_{-0.08}$
850 μm to 13 mm	0.71 ± 0.05	0.87 ± 0.14
7 mm to 13 mm	0.40 ± 0.06	1.08 ± 0.13
X-ray (2-8 keV) to 7 mm	0.33 ± 0.03	$0.068^{+0.006}_{-0.005}$
NIR (1.7 μm, 2.2 μm, 3.8 μm) to 7 mm	0.33 ± 0.03	0.08 ± 0.01

Table 8.4: Relative intrinsic angular shell size and mean velocity values for the areas mapped by different wavelengths of the observations summarized in Tab. 8.1 Sgr A*. Sizes and velocities have been derived according to Falcke et al. (2009).

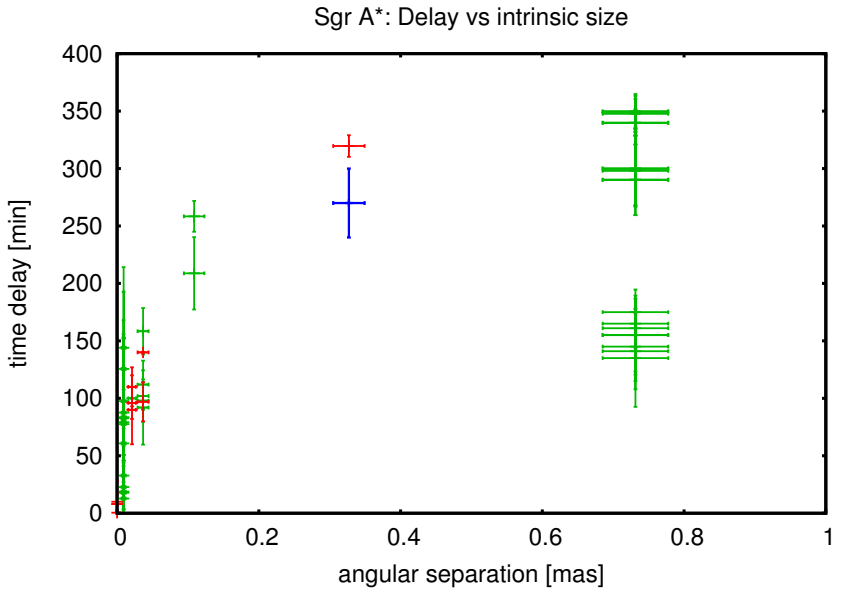

Figure 8.3: Time delay vs intrinsic size of the data in Tab. 8.5 plotted with a linear scale. The time delay of this thesis and Rauch et al. (2016) is plotted in blue, while red points are measurements directly linked to the X-ray/NIR core and green points represent interpolated data points.

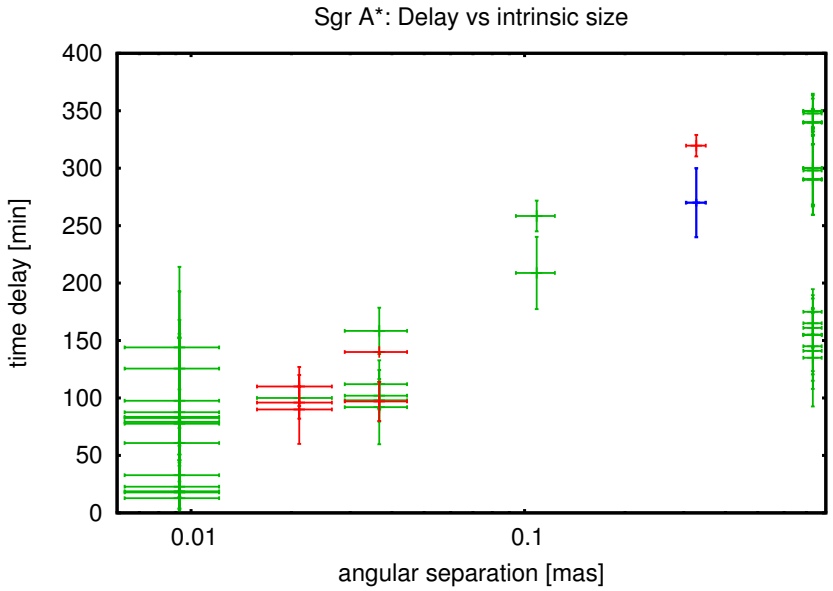

Figure 8.4: Time delay vs intrinsic size of the data in Tab. 8.5 plotted with a logarithmic scale. The time delay of this thesis and Rauch et al. (2016) is plotted in blue while red points are measurements directly linked to the X-ray/NIR core and green points represent interpolated data points.

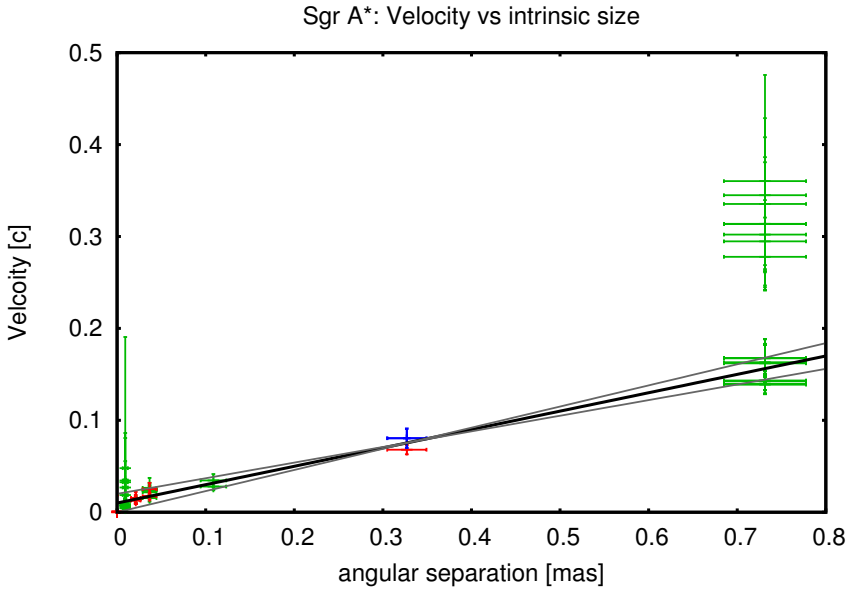

Figure 8.5: Velocity vs intrinsic size of the data in Tab. 8.5. The velocity derived from the time delay of this thesis and Rauch et al. (2016) is plotted in blue while red points are measurements directly linked to the X-ray/NIR core and green points represent interpolated data points.

Band	Intrinsic angular size [mas]	time delay [min]	Velocity [c]	Source
5kev	$(7 \pm 12) \times 10^{-11}$	0	0	
2.2 μm	$(9 \pm 8) 10^{-6}$	$8^{+10}_{-10.1}$	$(8 \pm 12) \times 10^{-5}$	Yusef-Zadeh et al. (2012)
2.2 μm	$(9 \pm 8) \times 10^{-6}$	$8^{+20.2}_{-17.9}$	$(8^{+21}_{-19}) \times 10^{-5}$	Yusef-Zadeh et al. (2012)
2.2 μm	$(9 \pm 8) \times 10^{-6}$	0.5^{+7}_{-6}	$(1^{+18}_{-15}) \times 10^{-3}$	Yusef-Zadeh et al. (2009)
2.2 μm	$(9 \pm 8) \times 10^{-6}$	10	6×10^{-5}	Eckart et al. (2006b)
450 μm	$(9 \pm 8) \times 10^{-6}$	126^{+68}_{-18}	$0.005^{+0.004}_{-0.002}$	Interpolation of 450 μm delay (Yusef-Zadeh et al., 2009) from 1.3 mm delay (Brinkerink et al., 2015)
450 μm	$(9 \pm 3) \times 10^{-3}$	83^{+70}_{-28}	$0.007^{+0.007}_{-0.004}$	Interpolation of 450 μm delay (Yusef-Zadeh et al., 2009) from 1.3 mm delay (Marrone et al., 2008)
450 μm	$(9 \pm 3) \times 10^{-3}$	98^{+71}_{-25}	0.006 ± 0.005	Interpolation of 450 μm delay (Yusef-Zadeh et al., 2009) from interpolated 1.3 mm delay (Marrone et al., 2008; Yusef-Zadeh et al., 2008)
450 μm	$(9 \pm 3) \times 10^{-3}$	84^{+70}_{-26}	$0.007^{+0.005}_{-0.004}$	Interpolation of 450 μm delay (Yusef-Zadeh et al., 2009) from interpolated 1.3 mm delay (Marrone et al., 2008)
450 μm	$(9 \pm 3) \times 10^{-3}$	78^{+75}_{-37}	$0.008^{+0.008}_{-0.005}$	Interpolation of 450 μm delay (Yusef-Zadeh et al., 2009) from interpolated 1.3 mm delay (Marrone et al., 2008; Eckart et al., 2008c)
450 μm	$(9 \pm 3) \times 10^{-3}$	88^{+69}_{-22}	$0.007^{+0.006}_{-0.003}$	Interpolation of 450 μm delay (Yusef-Zadeh et al., 2009) from interpolated 1.3 mm delay (Marrone et al., 2008; Yusef-Zadeh et al., 2012)
450 μm	$(9 \pm 3) \times 10^{-3}$	144^{+71}_{-44}	$0.004^{+0.003}_{-0.002}$	Interpolation of 450 μm delay (Yusef-Zadeh et al., 2009) from 1.3 mm delay (Yusef-Zadeh et al., 2009)
450 μm	$(9 \pm 3) \times 10^{-3}$	61^{+20}_{-41}	$0.010^{+0.005}_{-0.008}$	Interpolation of 450 μm delay (Yusef-Zadeh et al., 2009) from 1.3 mm delay (Brinkerink et al., 2015)
450 μm	$(9 \pm 3) \times 10^{-3}$	18^{+27}_{-44}	$0.04^{+0.06}_{-0.09}$	Interpolation of 450 μm delay (Yusef-Zadeh et al., 2009) from 1.3 mm delay (Marrone et al., 2008)
450 μm	$(9 \pm 3) \times 10^{-3}$	33^{+29}_{-46}	$0.02^{+0.02}_{-0.03}$	Interpolation of 450 μm delay (Yusef-Zadeh et al., 2009) from interpolated 1.3 mm delay (Marrone et al., 2008; Yusef-Zadeh et al., 2008)
450 μm	$(9 \pm 3) \times 10^{-3}$	19^{+28}_{-45}	$0.03^{+0.05}_{-0.08}$	Interpolation of 450 μm delay (Yusef-Zadeh et al., 2009) from interpolated 1.3 mm delay (Marrone et al., 2008)
450 μm	$(9 \pm 3) \times 10^{-3}$	13^{+38}_{-52}	$0.05^{+0.15}_{-0.20}$	Interpolation of 450 μm delay (Yusef-Zadeh et al., 2009) from interpolated 1.3 mm delay (Marrone et al., 2008; Eckart et al., 2008c)
450 μm	$(9 \pm 3) \times 10^{-3}$	23^{+24}_{-42}	$0.03^{+0.03}_{-0.06}$	Interpolation of 450 μm delay (Yusef-Zadeh et al., 2009) from interpolated 1.3 mm delay (Marrone et al., 2008; Yusef-Zadeh et al., 2012)
450 μm	$(9 \pm 3) \times 10^{-3}$	80^{+29}_{-57}	$0.008^{+0.004}_{-0.007}$	Interpolation of 450 μm delay (Yusef-Zadeh et al., 2009) from 1.3 mm delay (Yusef-Zadeh et al., 2009)
850 μm (353GHz)	$(2.1 \pm 0.6) \times 10^{-2}$	110 ± 17	0.013 ± 0.004	Yusef-Zadeh et al. (2008)
850 μm (353GHz)	$(2.1 \pm 0.6) \times 10^{-2}$	96 ± 14	0.015 ± 0.005	Marrone et al. (2008)
850 μm (353GHz)	$(2.1 \pm 0.6) \times 10^{-2}$	90 ± 30	0.016 ± 0.007	Eckart et al. (2008c)
850 μm (353GHz)	$(2.1 \pm 0.6) \times 10^{-2}$	100	0.015 ± 0.004	NIR to 850 μm delay (Yusef-Zadeh et al., 2012)
1.3mm (230GHz)	$(3.7 \pm 0.6) \times 10^{-2}$	140	0.018 ± 0.004	Brinkerink et al. (2015)
1.3mm (230GHz)	$(3.7 \pm 0.6) \times 10^{-2}$	97 ± 17	0.025 ± 0.007	Marrone et al. (2008)
1.3mm (230GHz)	$(3.7 \pm 0.6) \times 10^{-2}$	112 ± 21	0.022 ± 0.007	Interpolation of 1.3 mm delay (Marrone et al., 2008) from 850 μm delay (Yusef-Zadeh et al., 2008)
1.3mm (230GHz)	$(3.7 \pm 0.6) \times 10^{-2}$	98 ± 19	0.025 ± 0.008	Interpolation of 1.3 mm delay (Marrone et al., 2008) from 850 μm delay (Marrone et al., 2008)
1.3mm (230GHz)	$(3.7 \pm 0.6) \times 10^{-2}$	92 ± 33	0.026 ± 0.011	Interpolation of 1.3 mm delay (Marrone et al., 2008) from 850 μm delay (Eckart et al., 2008c)
1.3mm (230GHz)	$(3.7 \pm 0.6) \times 10^{-2}$	102 ± 12	0.022 ± 0.006	Interpolation of 1.3 mm delay (Marrone et al., 2008) from 850 μm delay (Yusef-Zadeh et al., 2012)
1.3mm (230GHz)	$(3.7 \pm 0.6) \times 10^{-2}$	158^{+21}_{-41}	$0.015^{+0.004}_{-0.006}$	(Yusef-Zadeh et al., 2009)
3mm (86GHz)	(0.109 ± 0.015)	258^{+14}_{-21}	0.028 ± 0.005	Interpolation of 3 mm delay (Yusef-Zadeh et al., 2009) from 7 mm delay (Yusef-Zadeh et al., 2009)
3mm (86GHz)	(0.109 ± 0.015)	209^{+32}_{-36}	$0.035^{+0.007}_{-0.008}$	Interpolation of 3 mm delay (Yusef-Zadeh et al., 2009) from 7 mm delay (Rauch et al., 2016)
7mm (43GHz)	(0.33 ± 0.03)	$319.6^{+9.4}_{-7.6}$	$0.068^{+0.006}_{-0.005}$	Yusef-Zadeh et al. (2009)
7mm (43GHz)	(0.33 ± 0.03)	270 ± 30	0.081 ± 0.011	Rauch et al. (2016)
13mm (22GHz)	(0.73 ± 0.05)	350^{+14}_{-13}	0.139 ± 0.011	Interpolation of 13 mm delay (Marrone et al., 2008) from 7 mm delay (Yusef-Zadeh et al., 2009)
13mm (22GHz)	(0.73 ± 0.05)	300 ± 32	0.16 ± 0.02	Interpolation of 13 mm delay (Marrone et al., 2008) from 7 mm delay (Rauch et al., 2016)
13mm (22GHz)	(0.73 ± 0.05)	340^{+12}_{-11}	0.14 ± 0.01	Interpolation of 13 mm delay (Yusef-Zadeh et al., 2008) from 7 mm delay (Yusef-Zadeh et al., 2009)
13mm (22GHz)	(0.73 ± 0.05)	290 ± 31	0.17 ± 0.03	Interpolation of 13 mm delay (Yusef-Zadeh et al., 2008) from 7 mm delay (Rauch et al., 2016)
13mm (22GHz)	(0.73 ± 0.05)	350^{+15}_{-15}	0.139 ± 0.011	Interpolation of 13 mm delay (Yusef-Zadeh et al., 2008) from 7 mm delay (Yusef-Zadeh et al., 2009)
13mm (22GHz)	(0.73 ± 0.05)	300^{+33}_{-33}	0.16 ± 0.03	Interpolation of 13 mm delay (Yusef-Zadeh et al., 2008) from 7 mm delay (Rauch et al., 2016)
13mm (22GHz)	(0.73 ± 0.05)	340^{+12}_{-10}	0.14 ± 0.01	Interpolation of 13 mm delay (Yusef-Zadeh et al., 2008) from 7 mm delay (Yusef-Zadeh et al., 2009)
13mm (22GHz)	(0.73 ± 0.05)	290 ± 31	0.17 ± 0.03	Interpolation of 13 mm delay (Yusef-Zadeh et al., 2008) from 7 mm delay (Rauch et al., 2016)
13mm (22GHz)	(0.73 ± 0.05)	348^{+14}_{-12}	0.140 ± 0.011	Interpolation of 13 mm delay (Yusef-Zadeh et al., 2008) from 7 mm delay (Yusef-Zadeh et al., 2009)
13mm (22GHz)	(0.73 ± 0.05)	298 ± 32	0.16 ± 0.03	Interpolation of 13 mm delay (Yusef-Zadeh et al., 2008) from 7 mm delay (Rauch et al., 2016)
13mm (22GHz)	(0.73 ± 0.05)	175^{+20}_{-29}	$0.28^{+0.04}_{-0.05}$	Interpolation of 13 mm delay (Yusef-Zadeh et al., 2008) from 850 μm delay (Yusef-Zadeh et al., 2008)
13mm (22GHz)	(0.73 ± 0.05)	161^{+18}_{-27}	$0.30^{+0.04}_{-0.06}$	Interpolation of 13 mm delay (Yusef-Zadeh et al., 2008) from 850 μm delay (Marrone et al., 2008)
13mm (22GHz)	(0.73 ± 0.05)	155^{+32}_{-38}	$0.31^{+0.07}_{-0.08}$	Interpolation of 13 mm delay (Yusef-Zadeh et al., 2008) from 850 μm delay (Eckart et al., 2008c)
13mm (22GHz)	(0.73 ± 0.05)	176^{+10}_{-23}	$0.28^{+0.03}_{-0.05}$	Interpolation of 13 mm delay (Yusef-Zadeh et al., 2008) from 850 μm delay (Yusef-Zadeh et al., 2012)
13mm (22GHz)	(0.73 ± 0.05)	155 ± 35	0.31 ± 0.08	Interpolation of 13 mm delay (Yusef-Zadeh et al., 2008) from 850 μm delay (Yusef-Zadeh et al., 2008)
13mm (22GHz)	(0.73 ± 0.05)	141 ± 34	0.34 ± 0.09	Interpolation of 13 mm delay (Yusef-Zadeh et al., 2008) from 850 μm delay (Marrone et al., 2008)
13mm (22GHz)	(0.73 ± 0.05)	135 ± 43	0.36 ± 0.12	Interpolation of 13 mm delay (Yusef-Zadeh et al., 2008) from 850 μm delay (Eckart et al., 2008c)
13mm (22GHz)	(0.73 ± 0.05)	156 ± 30	0.31 ± 0.07	Interpolation of 13 mm delay (Yusef-Zadeh et al., 2008) from 850 μm delay (Yusef-Zadeh et al., 2012)

Table 8.5: Data points interpolated from Tab. 8.1 Sizes and velocities have been derived according to Falcke et al. (2009).

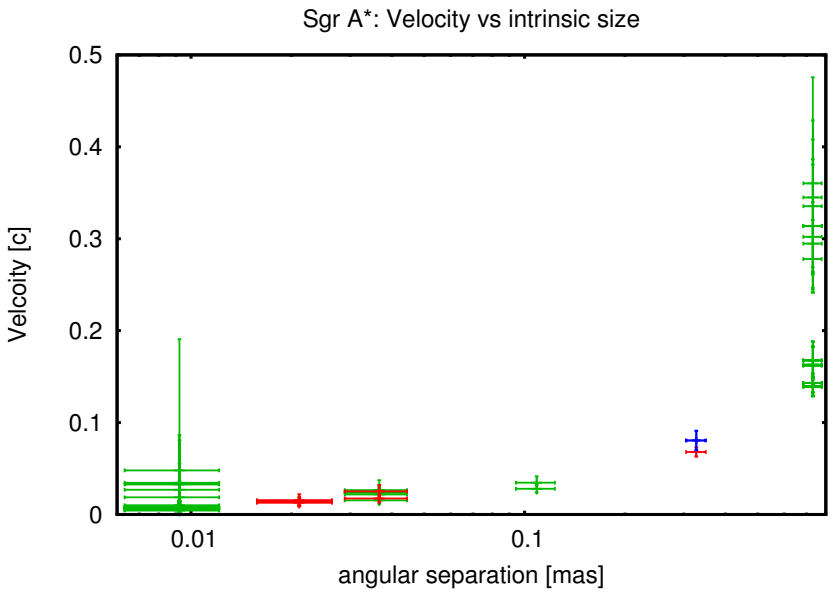

Figure 8.6: Velocity vs intrinsic size of the data in Tab. 8.5 plotted with a logarithmic scale. The velocity derived from the time delay of this thesis and Rauch et al. (2016) is plotted in blue while red points are measurements directly linked to the X-ray/NIR core and green points represent interpolated data points.

and properties of the propagation medium, but the smooth trend of the interpolated data points without any large outliers, indicates a common mechanism as their origin.

The expansion seems still to be accelerating at the larges shown intrinsic size of 0.73 mas (13 mm). The velocities corresponding to wavelengths $\leq$ 7 mm are within their error limits equal to the expansion speeds of $v_{\mathrm{exp}} = 0.003 - 0.1\,\mathrm{c}$ reported by Eckart et al. (2008c) and Yusef-Zadeh et al. (2008). These presented expansion speeds have been derived from fitting light curve parameters at a single wavelength, while the presented velocity measurements of this thesis use the size-frequency power law of Falcke et al. (2009). Consistent velocities between these two unrelated methods are an indication for both approaches to accurately measure the velocities. The fact that 13 mm velocities are above these limits might come from the uncertainties of their derivation and/or from the normalization of the scattering law Falcke et al. (2009) used to derive the intrinsic size power law. While this normalization only has minor effects at wavelengths $\leq$7 mm, it significantly affects the intrinsic sizes at longer wavelengths. Especially the calculated time delays of 13 mm with respect to 850 μm appear to be too low, which results in higher expansion speeds. Therefore, these points have to be taken carefully into account. The fact that the presented time delay of this thesis relates to all observed values and velocities with respect to a common NIR/X-ray core is a strong indication for the correctness of this measurement. This is also an evidence for adiabatic expansion being the cooling mechanism of flares.

8.2 Model distinction

This section aims at discriminating between the models of Sgr A* based on the derived parameters of chapter 7. In this context, a hot spot model, as proposed by Yuan et al. (2009), would cause a change of the closure phases of Sgr A* depending on all properties affecting its symmetry and periodicity such as the hot spots orbital size, its inclination and the flux ratio between disc and hot spot. A temporary jet, anchored at Sgr A*, which can be produced by higher accretion rates during quiescent states or might be formed as a cause of instabilities in the accretion flow (e.g. Markoff et al. (2007)), would also be detected by non-zero closure phase values. Since the expected orbital period of a hot spot is much larger, than the observing time of the presented data set, the effect of these two models can only be distinguished by the scale on which they appear. According to Reid et al. (2008), hot spots, contributing more than 30% of the total 7 mm flux, can be ruled out to orbit at radii above $\sim$80 μas. Adiabatically expanding off-center components are also limited by this boundary condition. Fainter hot spots at bigger radii are still possible, but a secondary component of 0.02 Jy at 1.5 mas (circular model fit) or (1.8 ± 0.4) mas, (delta component fit) as described by this data set, is much higher than this limit and can not be caused by a hot spot. A jet feature on the other hand is not excluded by this and is, therefore, the best possible origin of this structure.

The described source morphology and time delay between NIR to 7 mm observations points towards a possible adiabatically expanding jet feature to be present during the flaring states of Sgr A*, which leads to a deviation from its point like source structure at detectable scales. Since the hypothesis of a jet present at AGN, has already been reported for other source, like the second closest nucleus of M 81, it is reasonable to assume that such a feature is also present in Sgr A*. This source is four orders of magnitude more luminous than Sgr A* and represents a link between high luminosity AGN and Sgr A* (Ros & Pérez-Torres, 2012). Even though, different flaring mechanisms are possible for more luminous galactic centers, their common evolution suggests a comparable mechanism to be present in all AGN. Phase referencing observations of M 81 also revealed a core shift, and a changing jet orientation provides evidence of a possible precession of its jet (Alberdi et a., 2013).

The observational properties of the data presented in this work do not allow to put hard constraints on such a mechanism in Sgr A*, but shows its possible existence in a comparable environment. The indications of a secondary component during the flaring phases of Sgr A* are at about one to two sigma, but the complete set of hints, that consistently point towards its existence, raises interest in future observations to validate the reported results. Even though, we can not exclude that the described effects are caused by random weather effects or residual observational uncertainties, the best possible model that explains all described peculiarities is a short time jet to be present during the flaring phases of Sgr A*.

Chapter 9

Future outlook

The Galactic Center source Sgr A* is subject to many observational obstacles, such as strong extinction and scattering effects. The current uncertainties in determining its mass and distance amount to $< 10\%$ in mass and $< 5\%$ in distance. With the ongoing evolution of observational techniques and new telescopes, these error limits will approach a few percent in the next decade and will make it possible to use the Galactic Center as a well known calibrator for extragalactic distance measurements.

With the imminent commissioning of next generation of telescopes, like the Event Horizon Telescope, the improved resolution of these telescopes approaches the predicted scales of the event horizon. Therefore, we are at the dawn of an age, where it will be possible to actually observe the event horizon of Sgr A*, which will most likely provide observational proof of the existence of a Galactic Center black hole or will raise the need of other theories which can explain the observed compact object of very high mass in the centers of our and other galaxies. This improved resolution will also make it possible to exclude some of the described alternative models in chapter 2.2.

The presented multi wavelength observation at NIR and 7 mm has shown the success and capability of such observations to provide reliable results. In this context future campaigns are necessary to increase the crucial knowledge of the scattering law, which is required to be known accurately to measure intrinsic Galactic Center source sizes. Further observations are also needed to close the gaps in the radial view of Sgr A* presented in section 8.1. These observations are able to provide sizes as well as time delays between flares and will encourage scientists to put further constraints on the underlying mechanism of the flaring behavior of Sgr A*. While it is still unclear which of the described models can adequately explain the properties of observations during its flaring state, the subject offers a lot of possible topics that can be addressed.

The method of observing Sgr A* at multiple frequencies, ranging from NIR/X-ray to radio bands, will definitely provide additional data which are capable of putting harder constraints on the current theories about the origin of flares in the Galactic Center. For this reason we are looking forward to the results of an observing campaign held in Oct 2014 (BR201), which has been performed using the same observational parameters as the described data set BE061 of this thesis. A huge difference has been made by including geodetic blocks, in order to be able to generate an improved model and thus, improving the phase referencing capabilities of these observations. This will make it possible to gain further evidence about a possible positional shift of Sgr A* during flares.

While the passage of the DSO/G2 object in 2014 showed, in contrary to the expectations, no increase of the accretion or flaring rate of Sgr A*, its next passage in

2018 offers another possibility to observe potential effects on the Galactic Center black hole. The need of more observations seems evident and will hopefully lead to more multi-wavelength campaigns for the current and next generation of telescopes.

Bibliography

Abramowicz, M. G.,Kluźniak, & Lasota, J.-P. 2002, A&A 396, L31-L34 (Cited on page 20.)

Akiyama, K., Takahashi, R., Honma, M., Oyama, T., & Kobayashi, H. 2013, PASJ, 65, 91 (Cited on page 71.)

Alberdi, A., Martí-Vidal, I., Marcaide, J. M. et al. 2013, EPJ Web of Conferences, 61, 08002 (Cited on page 100.)

Alexander, T. 1999, ApJ, 527, 835 (Cited on page 17.)

Alexander, T. 2005, Phys. Rep., 419, 65 (Cited on page 17.)

Alexander, T., & Hopman, C. 2009, ApJ, 697, 1861 (Cited on page 17.)

Amaro-Seoane, P., & Chen, X. 2014, ApJ, 781, L18 (Cited on page 17.)

Aschenbach, B., Grosso, N., Porquet, D., & Predehl, P. 2004, A&A, 417, 71 (Cited on page 24.)

Backer, D. C., Zensus, J. A., Kellerman, K. I., et al. 1993, Science, 262, 1414 (Cited on page 42.)

Baganoff, F. K., Bautz, M. W., Brandt, W. N., et al. 2001, Nature, Vol. 413, 45-48 (Cited on pages 23 and 24.)

Baganoff, F. K., Bautz, M. W:, Morris, M., et al. 2003, ApJ, 591, 891 (Cited on pages vii, 14 and 21.)

Balick, B., Brown, R. L. 1974, ApJ, 194, 265 (Cited on page 13.)

Ball, G. H., Narayan, R., & Quataert, E. 2001, ApJ, 552, 221 (Cited on page 24.)

Bartko, H., Martins, F., Trippe, S., et al. 2010, ApJ, 708, 834 (Cited on page 17.)

Bélanger, G., Goldwurm, A., Melia, F., et al. 2005, ApJ, 635, 1095 (Cited on page 91.)

Bertram, T. 2007, Cophasing LINC-NIRVANA and Molecular gas in low-luminosity QSO host and cluster galaxies, Inaugural-Dissertation, Cologne 2007 (Cited on page 48.)

Binney, J. & Tremaine, S. 1987, Galactic Dynamics, PUP (Cited on page 17.)

Blandford, R. D. & Begelman, M. C. 1999, MNRAS, 303, L1 (Cited on page 24.)

Bolton, C. T. 1972, Nature Physical Science, 240, 124-127 (Cited on page 16.)

Bombaci, I. 1996, A&A, 305, 871 (Cited on page 7.)

Bovy, J., Hogg, D. W., & Rix, H.-W. 2009, ApJ, 704, 1704 (Cited on page 9.)

Bower, G. C., Falcke, H., Herrnstein, R. M., et al. 2004, Science, 304, 704 (Cited on page 43.)

Bower, G. C., Goss, W. M., Falcke, H., Backer, D. C., & Lithwick, Y. 2006, ApJ, 648, L127 (Cited on pages 42 and 43.)

Bower, G. C., Markoff, S., Brunthaler, A., et al. 2014, ApJ, 790, Issue 1, article id. 1, 10pp (Cited on page 71.)

Bowyer, S., Byram, E. T., Chubb, T. A., Friedman, H. 1965, Science 147, 3656, 394-398 (Cited on page 16.)

Brinkerink, C. D., Falcke, H., Law, C. J., et al. 2015, A&A, 576, A41 (Cited on pages 91 and 98.)

Broderick, A. E., & Loeb, A. 2006, MNRAS, 367, 905 (Cited on pages 26 and 27.)

Broderick, A. E., & Narayan, R., 2006, "On the nature of the compact dark mass at the galactic center", ApJ Letter, 638, L21 (Cited on pages 20 and 27.)

Broderick, A. E., Fish, V. L., Doeleman, S. S., & Loeb, A. 2011, ApJ, 738, 38 (Cited on page 74.)

Buchholz, R. M., Schödel, R., & Eckart, A. 2009, A&A, 499, 483 (Cited on page 17.)

Chan, C.-K., Liu, S., Fryer, C. L., et al. 2009, ApJ, 701, 521 (Cited on page 27.)

Chapline, G. 2005, "Dark energy stars", Proc. of 22nd Texas Symp. on Relativistic Astrophysics at Stanford, edited by: Chen, P., Bloom, E., Madejski, G., & Patrosian, V., 101 (Cited on page 20.)

Chatzopoulos, S., Fritz, T. K., Gerhard, O., et al. 2015, MNRAS, 447, 948 (Cited on page 17.)

Christopher, M. H., Scoville, N. Z., Stolovy, S. R., & Yun, M. S 2005, ApJ, 622, 346 (Cited on page 12.)

Clark, B. G. 1999, ASP Conf. Series, 180, p. 1. (Cited on page 31.)

Cotton, W. D., 1995, "Fringe-Fitting" in Very Long Baseline Interferometry and the VLBA, ASP conf. series, Vol. 82, p. 189, Zensus, J. A., Diamond, P. J., & Napier, P. J. eds. (Cited on page 57.)

Dale, J. E., Davies, M. B., Church, R. P., & Freitag, M. 2009, MNRAS, 393, 1016 (Cited on page 17.)

Do, T., Ghez, A. M., Morris, M. R., et al. 2009, ApJ, 703, 1323 (Cited on page 17.)

Dodds-Eden, K., Porquet, D., Trap, G., Quataert, E., Haubois, X. et al. 2009, ApJ, 698, 676 (Cited on page 26.)

Doeleman, S. S., Shen, Z.-Q., Rogers, A. E. E. et al. 2001, AJ, 121, 2610 (Cited on page 42.)

Donea, A. C., Falcke, H., & Biermann, P. L. 1999, ASP Conf. Ser. Vol. 186, Falcke, H., Cotera, A., Duschl, W. J., Melia, F., Rieke, M. J., eds. (Cited on page 24.)

Eckart, A., & Genzel, R. 1996, Nature, 383, 415 (Cited on pages 18 and 20.)

Eckart, A., & Genzel, R. 1997, MNRAS 284, 576 (Cited on page 18.)

Eckart, A., Genzel, R. Ott, T., & Schödel, R. 2002, MNRAS 331, 917 (Cited on page 18.)

Eckart, A., Baganoff, F. K., Morris, M., Bautz, M. W., Brandt, W. N., et al. 2004, A&A, 427, 1 (Cited on pages 23, 26 and 91.)

Eckart, A., Schödel, R., Meyer, L. et al. 2006, The Messenger, Vol. 125, page 2 (Cited on page 24.)

Eckart, A., Baganoff, F. K., Schödel, R. et al. 2006, A&A, 450, 535 (Cited on pages 23, 24, 26, 91 and 98.)

Eckart, A., Schödel, R., Meyer, L. et al. 2006, A&A, 455, 1 (Cited on pages 24 and 26.)

Eckart, A., Baganoff, F. K., Zamaninasab, M. R. et al. 2008, A&A, 479, 625 (Cited on pages 23, 26 and 91.)

Eckart, A., Baganoff, F. K., Morris, M. R. et al. 2008, JPhCS, 131, 012006 (Cited on page 23.)

Eckart, A., Schödel, R., García-Marín, M., et al. 2008, A&A, 492, 337 (Cited on pages 23, 91, 98 and 99.)

Eckart, A., Baganoff, F. K., Morris, M. R. et al. 2009, A&A, 500, 935 (Cited on page 23.)

Eckart, A., García-Marín, M., Vogel, S. N., et al. 2012, A&A, 537, A52 (Cited on page 24.)

Einstein, A. 1916, Annalen der Physik 49, 769 (Cited on page 15.)

Eisenhauer, F., Genzel, R., Alexander, T., et al. 2005, ApJ, 628, 246 (Cited on pages 17 and 18.)

Falcke, H. & Markoff, S. 2000, A&A, 362, 113 (Cited on page 25.)

Falcke, H., Markoff, S., & Bower, G. C. 2009. A&A, 496, 77 (Cited on pages xi, 43, 92, 93, 94, 95, 96, 98 and 99.)

Feldmeier, A., Neumayer, N., Seth, A., et al. 2014, A&A, 570, A2 (Cited on page 17.)

Ferrarese, L. & Merritt, D. 2000, ApJ, 539, L9 (Cited on pages 7, 16 and 18.)

Fish, V. L., Doeleman, S. S., Beaudoin, C., et al. 2011, ApJ, 727, L36 (Cited on page 74.)

Fizeau, H. 1868, Prize Bordin, Report on the Contest of the year 1867, Chiefs: Duhamel, Pouillet, Regnault, Bertrand, Edmond Becquerel (Cited on page 31.)

Fried, D. L. 1982, J. Opt. Soc. Am., 72, 52 (Cited on page 48.)

Fritz, T. K., Gillessen, S., Dodds-Eden, K., et al. 2011, ApJ, 737, 73 (Cited on page 21.)

Fritz, T. K., Chatzopoulos, S., Gerhard, O., et al. 2014, arXiv:1406.7568 (Cited on page 18.)

Gebhardt, K., Bender, R., Bower, G., et al. 2000, ApJ, 539, L13 (Cited on pages 7 and 18.)

Genzel, R., Schödel, R., Ott, T., et al. 2003a, ApJ, 594, 812 (Cited on page 17.)

Genzel, R., Schödel, R., Ott, T., et al. 2003b, Nature, Vol. 425, 934 (Cited on pages 23, 24 and 27.)

Genzel, R., Eisenhauer, F., & Gillessen, S. 2010, Rev. Mod. Phys, 82, 3121 (Cited on pages 17 and 18.)

Ghez, A. M., Morris, M., Becklin, E. E., Tanner, A., Kremenek, T. 2000, Nature, 407, 349 (Cited on page 18.)

Ghez, A. M., Duchêne, G., Matthews, K., et al. 2003a, ApJ 586, L127 (Cited on page 17.)

Ghez, A. M., Becklin, E., Duchêne, G., et al. 2003b, ANS, 324, 527 (Cited on page 18.)

Ghez, A. M., Becklin, E., Duchene, G., et al. 2003c, AN, Supplementary Issue 1, Proceedings of the Galactic Center Workshop 2002, 527-533 (Cited on page 18.)

Ghez, A. M., Wright, S. A., Matthews, K., et al. 2004, ApJ, 601, L159 (Cited on page 24.)

Ghez, A. M., Salim, S., Hornstein, S. D., et al. 2005, ApJ, 620, 744 (Cited on page 18.)

Giacconi, R., Gursky, H., Paolini, F. R., & Rossi, B. B. 1962, Phys. Rev. Lett. 9, 439 (Cited on page 16.)

Gillessen, S., Eisenhauer, F., Quataert, e:, et al. 2006, ApJ, 640, L163 (Cited on pages 22 and 26.)

Gillessen, S., Eisenhauer, F., Trippe, S., et al. 2009, ApJ 692, 1075 (Cited on pages vii, 9, 18 and 19.)

Giroletti, M., Massaro, E., Tosti, G. et al. 2010, "Revealing the jets of the faintest BL Lacs", Fermi meets Jansky–AGN in Radio and Gamma-Rays, T. Savolainen et al. (eds), Bonn: MPIfR, p. 189 (Cited on page 36.)

Goto, M., Indriolo, N., Geballe, T. R. & Usuda, T. 2013, The Journal of Physics and Chemistry A, 117, 9919 (Cited on pages vii and 13.)

Gültekin, K., Gebhardt, K., Lauer, K., et al. 2009, ApJ, 698, 198 (Cited on pages 7 and 18.)

Guesten, R., Genzel, R., Wright, M. C. H., et al. 1987, ApJ, 456, 194 (Cited on page 12.)

Gwinn, C. R., Kovalev, Y. Y., Johnson, M. D., & Soglasnov V. A. 2014, ApJ 749, L14 (Cited on pages 58 and 71.)

Hamaus, N., Paumard, T., Müller, T., et al. (2009), ApJ, 692, 902 (Cited on page 27.)

Hemboldt, J.F., Taylor, G. B., Tremblay, S. et al. 2007, "The VLBA Imaging and Polarimetry Survey at 5 GHz", ApJ, 658, 203 (Cited on page 36.)

Herrnstein, R. M., Zhao, J.-H., Bower, G. C. & Goss, W. M. 2004, AJ, 127, 3399 (Cited on page 91.)

Högbom, J. A., Astron. Astrophys. Suppl. 15, 417-426 (Cited on page 38.)

Hornstein, S. D., Matthews, K., Ghez, A. M., et al. 2006, JPhCS, 54, 399 (Cited on page 22.)

Hornstein, S. D., Matthews, K., Ghez, A. M., et al. 2007, ApJ, 667, 900 (Cited on page 91.)

Igumenshchev, I. V. 2002, ApJ, 577, 31 (Cited on page 24.)

Jackson, J. M., Geis, N., Genzel, R., et al. 1993, Apj, 402, 173 (Cited on page 12.)

Jansky, K. G. 1933, Proc. IRE 21: 1387-98 (Cited on page 29.)

Jennison, R. C. 1958, MNRAS, 118, 276 (Cited on pages 68 and 72.)

Johnson, M. D. & Gwinn, C. R. 2015, ApJ 805, 180 (Cited on pages 58 and 71.)

Kellermann, K. I. & Moran, J. M. 2001, ARA&A, 39, 457 (Cited on page 29.)

Kerr, R. P. 1963, PRL 11, 237-238 (Cited on page 15.)

Klein, U. 2006, "Radio Astronomy - tools, application and impacts", Argelander-Institut für Astronomie - Bonn, printed lecture notes Rev. Sep 2011 (Cited on page 29.)

Klöckner, H.-R. 2014, "Principles of Interferometry", IMPRS Black Board Lectures 2014 (Cited on page 29.)

Kogan, L. 1995, Effect of Digitizers Errors on the Cross and Auto Correlation Response of an FX Correlator, VLBA Scientific Memo No. 9 (Cited on page 54.)

Kormendy, J., & Gebhardt, K. 2001, Relativistic Astrophysics: 20th Texas Symposium. AIP Conference Proceedings 586, 363-381 (Cited on page 16.)

Kovalev, Y.Y., Petrov, L., Fomalont, E. B., & Gordon, D. 2007, "The Fifth VLBA Calibrator Survey: VCS5", AJ, 133, 1236 (Cited on page 36.)

Krabbe, A., Genzel, R., Eckart, A., et al. 1995, ApJ, 447, L95 (Cited on page 17.)

Krichbaum, T. P., Graham, D. A., Witzel, A. et al. 1998, A&A, 335, L106 (Cited on page 42.)

Krichbaum, T. P., Graham, D. A., Bremer, M. et al. 2006, JPhCS, 54, 328 (Cited on pages 42 and 43.)

van Langevelde, H. J., Frail, D. A., Cordes, J. M., & Diamond, P. J. 1992, ApJ, 396, 686 (Cited on page 42.)

Laplace, P. S. 1796, Exposition du Systéme du Monde (Cited on page 15.)

Launhardt, R., Zylka, R., & Mezger, P. G. 2002, A&A, 384, 112 (Cited on page 12.)

Lee, S.-S., Lobanov, A. P., Krichbaum, T. P. et al. 2008, "A Global 86 GHZ VLBI Survey of Compact Radio Sources", AJ, 136, 159 (Cited on page 36.)

Leppänen, K. J. 1993, Opacity Correction for High Frequency VLBI Observations, VLBA Scientific Memo No. 1 (Cited on page 54.)

Lewis, E., "Fundamentals of Nuclear Reactor Physics, 1st Edition", Academic Press, Print ISBN: 9780123706317 (Cited on pages vii and 9.)

Lister, M.L., Aller, H. D., Aller, M. F. et al. 2009, "MOJAVE: Monitoring of Jets in Active Galactic Nuclei with VLBA Experiments. V. Multi-Epoch VLBA Images", AJ 137, 3718 (Cited on page 36.)

Liu, S., Melia, F., & Petrosian, V. 2006, ApJ, 611, L101 (Cited on page 26.)

Lo, K. Y., Shen, Z.-Q., Zhao, J.-H. & Ho, P. T. P. 1998, ApJ, 598, L61 (Cited on page 42.)

Loeb, A, & Waxman, E. 2007, JCAP, 3, 11 (Cited on page 25.)

Löckmann, U., Baumgardt, H., & Kroupa, P. 2010, MNRAS, 402, 519 (Cited on page 17.)

Lu, R. S., Ghez, A. M., Hornstein, S. D., et al. 2006, JPhCS, 54, 279 (Cited on page 17.)

Lu, R. 2010, High Frequency VLBI Studies of Sagittarius A* and NRAO 530, Inaugural-Dissertation, University of Cologne (Cited on pages 24, 25 and 26.)

Lu, R.-S., Krichbaum, T. P., Eckart, A., et al. 2011a, ASP Conf. ser., 439, 331 (Cited on pages 42 and 43.)

Lu, R. S., Krichbaum, T. P., Eckart, A., et al. 2011b, A&A, 525, A76 (Cited on pages 24 and 60.)

Lucy, L. B. 1974, AJ, 79, 745L (Cited on page 40.)

Luminet, J. P. 1979, A&A 75, 1-2, 228-235 (Cited on page 16.)

Lynden-Bell, D., & Sanitt, N. 1969, MNRAS 143, 167 (Cited on page 16.)

Maoz, E. 1998, "Dynamical constraints on alternatives to supermassive black holes in galactic nuclei", ApJ Letter, 494, L181 (Cited on page 20.)

Markoff, S., Falcke, H., Yuan, F., & Biermann, P. L. 2001, A&A, 379, L13 (Cited on pages 25 and 26.)

Markoff, S., Bower, G. C., & Faclke, H. 2006, MNRAS, 379, 1519 (Cited on pages 25, 27, 89 and 100.)

Marrone, D. P., Moran, J. M., Zhao, J.-H., & Rao, R. 2006, JPhCS, 54, 354 (Cited on page 23.)

Marrone, D. P., Baganoff, F. K., Morris, M. R., et al. 2008, ApJ, 682, 373 (Cited on pages 91 and 98.)

Marscher, A. P. 2005, Mem. S.A.It., 76, 168 (Cited on pages x and 90.)

Marscher, A., Jorstad, S. G., Larionov, V. M., Aller, M. F., & Lähteenmäki 2011, "Multi-Waveband Emission Maps of Blazars", J.Astrophys. Astr. 32, 233 (Cited on page 36.)

Mauerhan, J. C., Morris, M., Walter, F., & Baganoff, F. K. 2005, ApJ, 623, L25 (Cited on pages 23 and 91.)

Mazur, P. O., & Mottola, E. 2001, arXiv:gr-qc/0109035 (Cited on page 20.)

McMillan, P. J., & Binney, J. 2010, MNRAS, 402, 934 (Cited on page 9.)

Meila, F. 1994, ApJ, 426, 577 (Cited on page 24.)

Melia, F., & Falcke, H. 2001, ARA&A, 39, 309 (Cited on page 24.)

Merrit, D., & Szell, A. 2006, ApJ, 648, 890 (Cited on page 17.)

Merrit, D. 2010, ApJ, 718, 739 (Cited on page 17.)

Meyer, L., Eckart, A., Schödel, R., Duschl, W. J., Mužić, K., et al. 2006, A&A, 460, 15 (Cited on pages 21, 23 and 26.)

Meyer, L., 2008a, The near-infrared activity of Sagittarius A*, Inaugural-Dissertation, University of Cologne (Cited on pages 12, 17, 22, 24 and 26.)

Meyer, L., Do, T., Ghez, A., et al. 2008b, ApJ, 688, L17 (Cited on page 91.)

Michell, J. 1784, Phil. Trans. R. Soc. Lond. 74, 58 (Cited on page 15.)

Middelberg, E., & Bach, U. 2008, Reports on Progress in Physics, 71, 6 (Cited on pages vii, viii, 31, 33, 34, 35, 37, 38, 41, 56, 57 and 85.)

Mieske, S., Hilker, M., & Infante, L. (2005), A&A, 438, 103-119 (Cited on page 9.)

Miyazaki, A., Tsuboi, M., & Tsutsumi, T. 2012, IAU Symposium, No. 290, 1, Zhang, C. M., Belloni, T., Mendez, M., & Zhang, S. N. eds. (Cited on page 24.)

Miyazaki, A., Tsuboi, M., & Tsutsumi, T. 2013, PASJ, 65, L6 (Cited on page 91.)

Moellenbrock, G. 2002, Synthesis Summer School, talk on "Calibration and Editing" (Cited on pages 43, 44, 45, 46, 47 and 49.)

Moran, J. M., & Dhawan, V. 1995, ASP conf. ser., 82, 161 (Cited on page 54.)

Munyaneza, F., Tsiklauri, D., & Viollier, R. D. 1998, "Sagittarius A*: A supermassive black hole or a spatially extended object?", ApJ Letter, 509, L105 (Cited on page 20.)

Narayan, R., & Goodman, J. 1989, MNRAS, 238, 963 (Cited on page 42.)

Narayan, R. & Yi, I. 1994, ApJ, 428, 13 (Cited on page 24.)

Narayan, R., Yi, I., & Mahadevan, R. 1995, Nature, 374, 623 (Cited on page 24.)

Narayan, R., Mahadevan, R., Grindlay, J. E., Popham, R. G., & Gammie, C. 1998, ApJ, 492, 554 (Cited on pages 24 and 25.)

Narayan, R., Igumenshchev, I. V., & Abramowicz, M. A. 2000, ApJ, 539, 798 (Cited on page 24.)

Narayan, R., Quataert, E., Igumenshchev, I. V., & Abramowicz, M. A. 2002, ApJ, 577, 295 (Cited on page 24.)

Newman, E. T., Couch, E., Chinnapared, K., et al. 1965, J. Math. Phys. 6, 918 (Cited on page 15.)

Nishiyama, S., Nagata, T., Tamura, M., et al. 2008, ApJ, 680, 1174 (Cited on page 21.)

Nishiyama, S., Tamura, M., Hatano, H., Nagata, T., Kudo, T., et al. 2009, ApJ, 702, L56 (Cited on page 26.)

Nordström, G. 1916, Proc. Acad. Sci. Amsterdam 20, 1238 (Cited on page 15.)

Ojha, R., Fey, A. L., Johnston, K. J., et al. 2004, "VLBI Observations of Southern Hemisphere ICRF Sources. I.", AJ, 127, 3609 (Cited on page 36.)

Ojha, R., Kadler, M., Böck et al. 2010, "TANAMI: Tracking Active Galactic Nuclei with Austral Milliarcsecond Interferometry I. First-Epoch 8.4 GHz images", A&A 519, 45 (Cited on page 36.)

Özel, F., Psaltis, D., & Narayan, R. 2000, ApJ, 541, 234 (Cited on page 25.)

Paumard, T., Genzel, R., Martins, F., et al. 2006, ApJ, 643, 1011 (Cited on pages 17 and 27.)

Peebles, P. J. E. 1972, ApJ, 178, 371 (Cited on page 16.)

Piner, B.G., Pant, N., Edwards, P. G. 2010, "The Jets of TeV Blazars at Higher Resolution: 43 GHz and Polarimetric VLBA Observations from 2005 to 2009", ApJ, 723, 1150 (Cited on page 36.)

Planck Collaboration, 2015, arXiv:1502.01589, A&A submitted (Cited on page 7.)

Pollack, L.K., Taylor, G. B., & Zavala, R. T. 2003, "VLBI Polarimetry of 177 Sources from the Caltech-Jodrell Bank Flat-Spectrum Survey", ApJ 589, 733 (Cited on page 36.)

Preto, M., & Amaro-Seoane, P. 2010, ApJ, 708, L42 (Cited on page 17.)

Quataert, E., & Gruzinov, A. 2000, ApJ 539, 809 (Cited on page 24.)

Quataert, E. 2002, ApJ, 575, 855 (Cited on page 25.)

Quataert, E. 2003, AN, 324, 435 (Cited on page 24.)

Quinlan, G. D., Hernquist, L., & Sigurdsson, S. 1995, 440. 554 (Cited on page 17.)

Rauch, C., Ros, E., Krichbaum, T. P., et al. 2016, A&A, 587, A37 (Cited on pages viii, ix, x, xi, 39, 52, 54, 59, 60, 61, 63, 64, 66, 67, 70, 72, 73, 75, 80, 81, 83, 89, 95, 96, 97, 98 and 99.)

Reber, G. 1944, ApJ, 100, 279 (Cited on page 29.)

Reber, G. 1948, Proc. IRE, 36, 1215 (Cited on page 29.)

Reid, M. J., & Brunthaler, A. 2004, ApJ, 616, 872 (Cited on page 9.)

Reid, M. J., Broderick, A. E., Loeb, A., & Brunthaler, A. 2008, ApJ, 682, 1041 (Cited on pages 27 and 100.)

Reid, M. J., Menten, K. M., Zheng, X. W., et al. 2009, ApJ, 700, 137 (Cited on page 9.)

Reissner, H. 1916, Ann. Physik 50, 106 (Cited on page 15.)

Richardson, W. H. 1972, JOSA, 62, 55 (Cited on page 40.)

Richstone, D., Ajhar, E. A., Bender, R., et al. 1998, Nature, 395, A14 (Cited on pages 7 and 18.)

Rogers, A. E. E., Doeleman, S. S., Wright, M. C. H., et al. 1994, ApJ, 434, L59 (Cited on page 42.)

Rohlfs, K. 1986, Tools of radio astronomy, Springer-Verlag, 332 p. (Cited on page 30.)

Romani, R.W., Narayan, R., & Blandford, R. 1986, MNRAS, 220, 19 (Cited on page 42.)

Ros, E., & Kadler, M. 2009, VLBI Data Analysis - Calibration, Edition and Fringe Fitting, 1st school on Multi-wavelength Astronomy, 29 Jun – 10 Jul 2009, Paris, France (Cited on pages 46, 51 and 55.)

Ros. E. 2012, 2011 Fermi & Jansky: Our Evolving Understanding of AGN„ St Michaels, MD, Nov 10-12, arXiv:1205.1043 (Cited on pages xi, 36 and 37.)

Ros, E. & Pérez-Torres, M. Á 2012, A&A, 537, A93 (Cited on page 100.)

Schmidt, M. 1963, Nature 197, 1040 (Cited on page 16.)

Schödel, R., Ott, T., Genzel, R., et al. 2002, Nature 419, 694 (Cited on pages 18 and 20.)

Schödel, R., Ott, T., Genzel, R., et al. 2003, ApJ 596, 1015 (Cited on page 18.)

Schödel, R., Eckart, A., Alexander, T., et al. 2007, A&A, 469, 125 (Cited on pages 12 and 17.)

Schödel, R., Merritt, D., & Eckart, A. 2009, A&A, 502, 91 (Cited on page 16.)

Schödel, R., Najarro, F., Mužić, K., & Eckart, A. 2010, A&A, 511, id.A18 (Cited on page 21.)

Schödel, R., Feldmeier, A., Kunneriath, D., et al. 2014, A&A, 566, A47 (Cited on pages 12 and 18.)

Schödel, R. 2015, IAU Symposium, No. 312, Spurzem, R., Liu, F., Li, S., & Meiron, Y., eds. (Cited on pages 12, 18 and 21.)

Schwarzschild, k. 1916, Sitzungsber. Preuss. Akad. Wiss., Phys. Math. Kl. 189 (Cited on page 15.)

Seth, A. C., van den Bosch, R., Baumgardt, H., et al. 2014, Nature, 513, 298 (Cited on pages 7 and 18.)

Shakura, N. I. & Sunyaev, R. A. 1973, A&A 24, 337-355 (Cited on page 16.)

Shahzamanian, B., Eckart, A., Valencia-S., M., et al. 2015, A&A, 576, A20 (Cited on pages ix, 39, 40 and 64.)

Shepherd, M. C., Pearson, T. J., & Taylor, G. B. 1994, Bulletin of the Astronomical Society, Vol. 26, No. 2, p. 987 - 989 (Cited on pages 37, 56, 58 and 65.)

Singh, D. K., Singh, R. P., & Kamra, A. K. 2004, The electrical environment of the earth's atmosphere: a review, Space Science Reviews, vol. 113, 3-4, pp.375 (Cited on pages viii and 42.)

Taylor, G.B. 2010, "The Parsec-Scale Characteristics of Fermi Blazars and Radio Galaxies", AAS Meeting 215, 225.03, BAAS 42, p. 543 (Cited on page 36.)

Torres, D. F., Capozziello, S., & Lambiase, G. 2000, Phys. Rev. D62, 104012 (Cited on page 20.)

Trippe, S., Paumard, T., Ott, T., Gillessen, S., Eisenhauer, F. 2007, MNRAS, 375, 764 (Cited on page 26.)

Tully, R. B., Courtois, H., Hoffman, Y., & Pomaréde, D. 2014, Nature, 513, number 7516, p71 (Cited on pages vii and 10.)

Vachaspati, T., Stojkovic, D., & Krauss, L. M. 2007, Phys. Rev. D76, 024005 (Cited on page 20.)

Viollier, R. D., Trautmann, D. & Tupper, G. B. 1993, "Supermassive neutrino stars and galactic nuclei", Phys. Letter B 306, 79 (Cited on page 20.)

Walker, C. 2002, Socorro Summer School, talk on "VLBI", `http://www.aoc.nrao.edu/events/synthesis/2002/vlbi.html` (Cited on pages 35 and 57.)

Witzel, G., Eckart, A., Bremer, M., et al. 2012, ApJS, 203, 18 (Cited on pages vii, 23 and 40.)

Young, P. 1980, ApJ, 242, 1232 (Cited on page 17.)

Yuan, F., Markoff, S., & Falcke, H. 2002, A&A, 383, 854 (Cited on pages 24, 25 and 27.)

Yuan, F., Quataert, E., & Narayan, R. 2003, ApJ, 598, 301 (Cited on pages vii, 22, 24, 25 and 26.)

Yuan, F., Quataert, E., & Narayan, R. 2004, ApJ, 606, 894 (Cited on pages 24 and 26.)

Yuan, F., Lin, J., Wu, K., & Ho, L. C. 2009, MNRAS, 395, 2183 (Cited on pages vii, 27, 89 and 100.)

Yusef-Zadeh, F., Bushouse, H., Dowell, C. D., Wardle, M., Roberts, D., et al. 2006a, ApJ, 644, 198 (Cited on page 26.)

Yusef-Zadeh, F., Roberts, D., Wardle, M, Heinke, C. O., & Bower, G. C. 2006b, ApJ, 650, 189 (Cited on pages 26 and 91.)

Yusef-Zadeh, F., Wardle, M., Heinke, C., et al. 2008, ApJ, 682, 361 (Cited on pages 23, 91, 98 and 99.)

Yusef-Zadeh, F., Bushouse, H., Wardle, M., et al. 2009, ApJ, 706, 348 (Cited on pages 68, 89, 91, 94 and 98.)

Yusef-Zadeh, F., Wardle, M., Dods-Eden, K., et al. 2012, AJ, 144, 1 (Cited on pages 91 and 98.)

Zamaninasab, M., Eckart, A., Meyer, L., et al. 2008, Proc. of "The Universe Under the Microscope - Astrophysics at High Angular Resolution", Editors: Schödel, R., Eckart, A., Pfalzner, S., & Ros, E., JPhCS, 131a (Cited on page 27.)

Zamaninasab, M. 2010a, Inaugural-Dissertation, University of Cologne, Near Infrared Polarimetry A Tool for Testing Properties of Sagittarius A* (Cited on page 15.)

Zamaninasab, M., Eckart, A., Witzel, G., Dovciak, M., Karas, V., et al. 2010b, A&A, 510, A3 (Cited on page 26.)

Zhao, J.-H., Young, K. H., Herrnstein, R. M., et al. 2003, ApJL, 586, 29 (Cited on page 91.)

Zhao, J.-H., Bower, G. C., Goss, C., & Liu, S. M. 2004, ApJ, 603, L85 (Cited on page 91.)

Erklärung

An Eides statt versichere ich, dass die vorgelegte Arbeit - abgesehen von den ausdrücklich bezeichneten Hilfsmitteln - persönlich, selbständig und ohne Benutzung anderer als der angegebenen Hilfsmittel angefertigt wurde, die aus anderen Quellen direkt oder indirekt übernommenen Daten und Konzepte unter Angabe der Quelle kenntlich gemacht sind, die vorgelegte Arbeit oder ähnliche Arbeiten nicht bereits anderweitig als Dissertation eingereicht worden ist bzw. sind, sowie eine Erklärung über frühere Promotionsversuche und deren Resultate, für die inhaltlich-materielle Erstellung der vorgelegten Arbeit keine fremde Hilfe, insbesondere keine entgeltliche Hilfe von Vermittlungs- bzw. Beratungsdiensten (Promotionsberater oder andere Personen) in Anspruch genommen wurde sowie keinerlei Dritte vom Doktoranden unmittelbar oder mittelbar geldwerte Leistungen für Tätigkeiten erhalten haben, die im Zusammenhang mit dem Inhalt der vorgelegten Arbeit stehen.

Teilpublikationen

Rauch, C.; Ros, E.; Krichbaum, T. P.; Eckart, A.; Zensus, J. A.; Shahzamanian, B.; Mužić, K.: "Wisps in the Galactic center: Near-infrared triggered observations of the radio source Sgr A* at 43 GHz", 2016, Astronomy and Astrophysics, Volume 587, A37

Unterschift:

———————————————————————

Datum:

———————————————————————